UNIVERSIDADE FEDERAL DE MINAS GERAIS
Instituto de Ciências Exatas
Programa de Pós-graduação em Física

Rafael Battistella Nadas

TIP-ENHANCED RAMAN SPECTROSCOPY AND PHOTOLUMINESCENCE IN TWO-DIMENSIONAL SYSTEMS

Belo Horizonte

2024

Rafael Battistella Nadas

TIP-ENHANCED RAMAN SPECTROSCOPY AND PHOTOLUMINESCENCE IN TWO-DIMENSIONAL SYSTEMS

Doctoral thesis presented to the Graduate Program in Physics at the Federal University of Minas Gerais as a partial requirement for the degree of Doctor in Physics.

Supervisor: Prof. Dr. Ado Jório de Vasconcelos
Co-supervisor: Prof. Dr. Luiz Gustavo de Oliveira Lopes Cançado

Belo Horizonte

2024

Dados Internacionais de Catalogação na Publicação (CIP)

N129t Nadas, Rafael Battistella.
Tip-enhanced Raman spectroscopy and photoluminescence in two-dimensional systems / Rafael Battistella Nadas. – 2024.
90 f. : il.

Orientador: Ado Jorio de Vasconcelos.
Coorientador: Luiz Gustavo de Oliveira Lopes Cançado.
Tese (doutorado) – Universidade Federal de Minas Gerais, Departamento de Física.
Bibliografia: f. 73 -87.

1. Espectroscopia de Raman. 2. Fotoluminescência. 3. Grafeno. I. Título. II. Vasconcelos, Ado Jorio de. III. Cançado, Luiz Gustavo de Oliveira Lopes. IV. Universidade Federal de Minas Gerais, Departamento de Física.

CDU – 543.424 (043)

Ficha catalográfica elaborada por Romário Martins Ribeiro – CRB6 3595
Biblioteca Professor Manoel Lopes de Siqueira – Departamento de Física - UFMG

UNIVERSIDADE FEDERAL DE MINAS GERAIS
INSTITUTO DE CIÊNCIAS EXATAS
PROGRAMA DE PÓS-GRADUAÇÃO EM FÍSICA

FOLHA DE APROVAÇÃO

A presente tese, intitulada **"Tip-enhanced Raman spectroscopy and photoluminescence in two-dimensional systems"** de autoria de **RAFAEL BATTISTELLA NADAS** submetida à Comissão Examinadora, abaixo-assinada, foi aprovada para obtenção do grau de **DOUTOR EM CIÊNCIAS**, em dezoito de abril de 2024.

Belo Horizonte, 18 de abril de 2024.

Prof. Ado Jorio de Vasconcelos
Orientador do estudante
Departamento de Física/UFMG

Prof. Luiz Gustavo de Oliveira Lopes Cançado
Coorientador do estudante
Departamento de Física/UFMG

Prof. Wagner Nunes Rodrigues
Departamento de Física/UFMG

Prof. Lukas Novotny
Instituto Federal de Tecnologia de Zurique/Suiça

Prof. Sebastian Daniel Heeg
Universidade Humboldt de Berlim

Prof. Mauricio Terrones Maldonado
Universidade Estadual da Pensilvânia/EUA

Prof. Vincent Meunier
Universidade Estadual da Pensilvânia/EUA

Documento assinado eletronicamente por **Ado Jorio de Vasconcelos**, **Professor do Magistério Superior**, em 18/04/2024, às 16:07, conforme horário oficial de Brasília, com fundamento no art. 5º do Decreto nº 10.543, de 13 de novembro de 2020.

Documento assinado eletronicamente por **Vincent Meunier**, **Usuário Externo**, em 18/04/2024, às 16:30, conforme horário oficial de Brasília, com fundamento no art. 5º do Decreto nº 10.543, de 13 de novembro de 2020.

Documento assinado eletronicamente por **Sebastian Daniel Heeg**, **Usuário Externo**, em 18/04/2024, às 16:52, conforme horário oficial de Brasília, com fundamento no art. 5º do Decreto nº 10.543, de 13 de novembro de 2020.

Documento assinado eletronicamente por **Wagner Nunes Rodrigues**, **Professor do Magistério Superior**, em 19/04/2024, às 10:53, conforme horário oficial de Brasília, com fundamento no art. 5º do Decreto nº 10.543, de 13 de novembro de 2020.

Documento assinado eletronicamente por **Mauricio Terrones**, **Usuário Externo**, em 19/04/2024, às 19:00, conforme horário oficial de Brasília, com fundamento no art. 5º do Decreto nº 10.543, de 13 de novembro de 2020.

Documento assinado eletronicamente por **Lukas Novotny**, **Usuário Externo**, em 24/04/2024, às 16:14, conforme horário oficial de Brasília, com fundamento no art. 5º do Decreto nº 10.543, de 13 de novembro de 2020.

Documento assinado eletronicamente por **Luiz Gustavo de Oliveira Lopes Cancado**, **Professor do Magistério Superior**, em 29/04/2024, às 14:17, conforme horário oficial de Brasília, com fundamento no art. 5º do Decreto nº 10.543, de 13 de novembro de 2020.

A autenticidade deste documento pode ser conferida no site https://sei.ufmg.br/sei/controlador_externo.php?acao=documento_conferir&id_orgao_acesso_externo=0, informando o código verificador **3190449** e o código CRC **094A5DAA**.

Referência: Processo nº 23072.222494/2024-19 SEI nº 3190449

Agradecimentos

Agradeço ao meu orientador, Professor Ado Jorio, e ao meu co-orientador, Professor Luiz Gustavo Cançado, pela dedicação e orientação ao longo deste percurso acadêmico. Suas orientações foram fundamentais para o desenvolvimento desta tese.

Expresso minha gratidão aos membros da banca, Prof. Sebastian Heeg, Prof. Vincent Meunier, Prof. Lukas Novotny, Prof. Mauricio Terrones e Prof. Wagner Nunes pela disposição em participar da avaliação deste trabalho.

À minha mãe Beatriz, meu pai Christian, meu irmão João Pedro, minha tia Dóris e minha prima Gabriella dedico minha mais profunda gratidão por todo o amor, incentivo e apoio ao longo de toda a minha vida e especialmente durante esta jornada acadêmica.

Agradeço de todo coração à minha amada namorada, Manuelle, pelo amor, compreensão e apoio incondicional durante este processo. Sua presença foi meu porto seguro nos momentos mais difíceis.

Não posso deixar de agradecer ao Professor Emilson, da UTFPR, por sua orientação e apoio no processo de ingresso no doutorado, que foi fundamental para o meu desenvolvimento acadêmico.

Agradeço ao meu amigo Lucão por sua amizade sincera e apoio desde o início do doutorado, sendo um grande amigo que me acolheu quando estive longe de casa, principalmente no momento em que tive um sério problema de saúde.

Agradeço também ao Andreij, cuja ajuda, sugestões e amizades foram fundamentais para o desenvolvimento desse doutorado.

Expresso minha gratidão ao Vitor, Cassiano e Hudson por sua presença e suporte em me ensinar do zero um sistema tão complexo.

Agradeço imensamente às pessoas que me ajudaram na preparação de amostras, Campolina, Gabriel, Gustavo, Ive, Lucas, Miyata-sensei e Rafael Martins, pela colaboração essencial para o sucesso deste trabalho.

A todos os meus colegas de laboratório e da FabNS, Andre, Augusto, Bianca, Bruno, Catarina, Danilo, Deybson, Diego, Douglas, Emerson, Fabiano, Filó, Fred, Gabriella, Jane, João, Joás Liliane, Luquinhas, Maíra, Matheus, Marcia, Maria, Mario, Menescal, Monken, Paniago, Paula, Plancácio, Rafael Rojas, Renan, Taiguara, Tiagão, Will e Xubaca, expresso minha sincera gratidão pela troca de conhecimento e interações no laboratório que deixaram o doutorado mais leve.

Agradeço também aos colegas de outros laboratórios e instituições com quem tive contato mais próximo, Ary, Eliel, Fábio, Jhonattan, Leo Campos, Maria Clara, Moalisson, Raphaela

e Saito-sensei, pela colaboração e amizade.

Por fim, expresso minha gratidão à CAPES, ao CNPq, ao SibratecNANO e à Fapemig pelo financiamento generoso e fundamental para a realização desta pesquisa. Seu apoio foi essencial para o desenvolvimento deste trabalho e para o avanço da ciência no país.

Acknowledgements

I would like to thank my advisor, Professor Ado Jorio, and my co-advisor, Professor Luiz Gustavo Cançado, for their dedication and guidance throughout this academic journey. Their guidance was crucial for the development of this thesis.

I express my gratitude to the committee members, Prof. Sebastian Heeg, Prof. Vincent Meunier, Prof. Lukas Novotny, Prof. Mauricio Terrones and Prof. Wagner Nunes for their willingness to participate in the evaluation of this work.

To my mother, Beatriz, my father, Christian, my brother, João Pedro, my aunt, Dóris, and my cousing, Gabriella I dedicate my deepest gratitude for all the love, encouragement, and support throughout my life and especially during this academic journey.

I thank my beloved girlfriend, Manuelle, for her love, understanding, and unwavering support during this process. Her presence was my safe haven in the most difficult moments.

I cannot fail to thank Professor Emilson from UTFPR for his guidance and support in the process of entering the doctoral program, which was fundamental to my academic development.

I thank my friend Lucão for his sincere friendship and support since the beginning of the doctoral program, being a great friend who welcomed me when I was far from home, especially when I had a serious health problem.

I also thank Andreij, whose help, suggestions, and friendship were fundamental to the development of this doctoral program.

I express my gratitude to Vitor, Cassiano, and Hudson for their presence and support in teaching me from scratch such a complex system.

I am immensely grateful to the people who helped me in the preparation of samples, Campolina, Gabriel, Gustavo, Ive, Lucas, Miyata-sensei and Rafael Martins, for their essential collaboration for the success of this work.

To all my laboratory colleagues and those from FabNS, Andre, Augusto, Bianca, Bruno, Catarina, Danilo, Deybson, Diego, Douglas, Emerson, Fabiano, Filó, Fred, Gabriella, Jane, João, Joás, Liliane, Luquinhas, Maíra, Matheus, Marcia, Maria, Mario, Menescal, Monken, Paniago, Paula, Plancácio, Rafael Rojas, Renan, Taiguara, Tiagão, Will, and Xubaca, I express my sincere gratitude for the exchange of knowledge and interactions in the laboratory that made the doctoral program lighter.

I also thank colleagues from other laboratories and institutions with whom I had closer contact, Ary, Eliel, Fábio, Jhonattan, Leo Campos, Maria Clara, Moalisson, Raphaela, and Saito-sensei, for their collaboration and friendship.

Finally, I express my gratitude to CAPES, CNPq, SibratecNANO, and Fapemig for the generous and fundamental funding for the realization of this research. Their support was essential for the development of this work and for the advancement of science in the country.

Resumo

Materiais bidimensionais (2D), caracterizados por propriedades emergentes de sua espessura em escala atômica, estrutura cristalina e propriedades de superfície, têm atraído considerável atenção na comunidade científica devido à ampla gama de aplicações em diversos campos, incluindo eletrônica, optoeletrônica, catálise e armazenamento de energia. Para explorar plenamente o potencial desses materiais, é importante estudá-los, e a espectroscopia Raman e a fotoluminescência têm sido amplamente utilizadas para investigá-los. No entanto, essas técnicas possuem um limite fundamental de resolução espacial, segundo o qual, a menor distância que se pode distinguir entre dois emissores de luz, é ditada pelo comprimento de onda da luz usada para iluminar. Mais especificamente, se a luz visível for usada, não é possível investigar características nanométricas desses materiais por meio dessas técnicas. A espectroscopia Raman amplificada por ponta (TERS) e a fotoluminescência amplificada por ponta (TEPL) ajudam a superar esse limite fundamental ao aproximar uma antena opticamente ativa da amostra, acessando o sinal não propagante proveniente da amostra (campo próximo). Neste caso, o limite de resolução não é mais limitado pela luz usada, mas pelo raio da ponta, permitindo o estudo de características nanométricas com luz visível. Uma dessas características são os fenômenos de coerência no sinal TERS do grafeno, assim como para os dicalcogenetos de metais de transição (TMDs). Nesta tese, é utilizado TERS coerente para medir o comprimento de coerência (L_c) do processo de espalhamento Raman no grafeno como função da energia de Fermi. L_c diminui quando a energia de Fermi é movida para o ponto de neutralidade, consistente com o conceito de anomalia de Kohn. Uma vez que o processo Raman envolve elétrons e fonons, os resultados observados podem ser entendidos como devido a uma variação grande da velocidade de grupo dos fônons ópticos, v_g, atingindo valores excepcionalmente altos para estes, ou devido a mudanças na incerteza da energia do elétron, ambas as propriedades sendo importantes para fenômenos ópticos e de transporte que podem não ser observáveis por qualquer outra técnica. Essa coerência de campo próximo também é investigada para os TMDs MoS_2, WS_2, $MoSe_2$ e WSe_2, mostrando que diferentes TMDs apresentam diferentes valores de comprimento de coerência Raman. Além disso, a resolução espacial alcançada com as pontas opticamente ativas permitiu a investigação de efeitos específicos dentro dos TMDs, como a investigação de fronteiras de grãos em MoS_2 crescidos por CVD, variações no TERS dentro de rugas de WS_2 e $MoSe_2$, do impacto do substrato nos espectros de TERS e TEPL de $MoSe_2$ e identificação de defeitos localizados em WSe_2. Finalmente, é feita uma tentativa de medir padrões de moiré em TMDs de bicamadas rodadas, mas bolhas nanométricas são emissores intensos, obscurecendo quaisquer características de

moiré nas medições.

Palavras-chave: Espectroscopia Raman melhorada por ponta; Fotoluminescência melhorada por ponta; Grafeno; Dicalcogenetos de metais de transição; Anomalia de Kohn; Comprimento de coerência Raman.

Abstract

Two-dimensional (2D) materials, characterized by their properties emerging from their atomic-scale thickness, crystal structure, and surface properties, have raised significant attention in the scientific community due to their diverse range of applications across numerous fields, including electronics, optoelectronics, catalysis, and energy storage. In order to fully explore their potentials, it is important to study such materials and Raman spectroscopy and photoluminescence have been widely used to investigate them. However, these techniques have a fundamental spatial resolution limit, since the minimum distance that one can distinguish two emitters of light is dictated by the wavelength of the light used to illuminate. Therefore, if one uses visible light, it is not possible to probe nanometric features of such materials through these techniques. Tip-enhanced Raman spectroscopy (TERS) and tip-enhanced photoluminescence (TEPL) overcome this fundamental limit by approximating an optical antenna to the sample, accessing the non-propagating (near field) signal coming from a sample. Now, the resolution limit is not constrained by the light used, but by the tip's radius, enabling the study of nanometric features with visible light, including related coherence phenomena in the TERS signal of graphene, as well as for transition metal dichalcogenides (TMDs). In this thesis, coherent TERS is used to measure the coherence length (L_c) of the Raman scattering process in graphene as a function of Fermi energy. L_c decreases when the Fermi energy is moved into the neutrality point, consistent with the concept of the Kohn anomaly. Once the Raman process involves both electrons and phonons, the observed results can be understood either as due to an unusually large variation of the longitudinal optical phonon group velocity v_g, reaching unprecedented high values for optical phonons, or due to changes in the electron energy uncertainty, both properties being important for optical and transport phenomena that might not be observable by any other technique. This near field coherence is also probed for the transition metal dichalcogenides (TMDs) MoS_2, WS_2, $MoSe_2$ and WSe_2, showing that different TMDs present different values of Raman coherence length. Furthermore, the spatial resolution achieved with optically active tips enabled the examination of specific effects within TMDs, such as grain boundaries in CVD-grown MoS_2, wrinkles in WS_2 and $MoSe_2$, and the substrate's impact on TERS and TEPL spectra of $MoSe_2$, and identifying localized defects in WSe_2. Finally, an attempt to measure moiré features in twisted bilayer TMDs is done, but nanometric size bubbles are brighter emitters, shadowing any moiré feature on the measurements.

Keywords: Tip-enhanced Raman spectroscopy; Tip-enhanced photoluminescence; Graphene; Transition metal dichalcogenides; Kohn anomaly; Raman coherence length.

List of abbreviations and acronyms

AFM Atomic force microscopy

EF Enhancement factor

FF Far field

FWHM Full width at half maximum

hBN Hexagonal Boron Nitride

MoS_2 Molybdenum disulfide

$MoSe_2$ Molybdenum diselenide

NF Near field

PTTP Plasmon tunable tip pyramids

SNOM Scanning near-field optical microscopy

TBG Twisted bilayer graphene

TEPL Tip-enhanced photoluminescence

TERS Tip-enhanced Raman spectroscopy

TMDs Transition metal dichalcogenides

WS_2 Tungsten disulfide

WSe_2 Tungsten diselenide

WTe_2 Tungsten ditelluride

Contents

Chapter 1

Introduction

Two-dimensional (2D) materials have been of great interest in the scientific community due to their unique electronic, mechanical, and optical properties, which differ significantly from the bulk form [1]. Among these materials, graphene and transition metal dichalcogenides (TMDs) stand out as prominent representatives, exhibiting remarkable characteristics that make them promising candidates for various applications ranging from electronics to optoelectronics and beyond [2, 3]. Understanding their optical, electronic and vibrational properties is crucial for using their full potential in practical applications.

In order to study these 2D materials properties, spectroscopic techniques have played an important role, enabling researchers to probe their electronic and vibrational properties [3–5]. One of such technique is Raman spectroscopy, named after Dr. Chandrasekhara Venkata Raman that in 1928 first probed the inelastic scattering of light [6]. Raman spectroscopy is a very useful technique to study materials science and it has provided valuable insights into the vibrational modes and structural characteristics of graphene and TMDs [7, 8]. Similarly, photoluminescence (PL) spectroscopy has emerged as a powerful tool for investigating the optical properties of two-dimensional TMDs [9]. The ability to probe the emission spectra of these materials provides valuable information about their electronic band structure and excitonic properties.

Even though Raman and PL spectroscopy are both very useful techniques to study materials properties, they are limited by the diffraction limit of light. In 1873, Ernst Abbe showed that the minimum distance Δx that one can clearly distinguish two emitters of light is about half of the wavelength (λ) of the incoming light [10]. This is called Abbe diffraction limit and, in 1879, Baron Rayleigh provided the equation for the so-called Rayleigh critereon, which imposes the theoretical diffraction limit [11]

$$\Delta x = 0.61 \frac{\lambda}{n \sin(\theta)} \tag{1.1}$$

where n is the medium refractive index and θ is the half-angle of the focal cone of light and they are usually combined in the so-called numerical aperture NA = $n\sin(\theta)$. For a high NA objective lens of 1.51, and using visible light at 400 nm, the minimum value for Δx=172 nm. Therefore, in order to study phenomena that happen in distances smaller than 172 nm, these

optical spectroscopies are not applicable.

The diffraction limit imposed by conventional optical microscopy poses a significant challenge when probing the nanoscale features of 2D materials. Overcoming this limitation has been a goal in the field of microscopy, driving researchers to explore innovative approaches to achieve higher spatial resolution. In 1928, Edward H. Synge proposed a method for extending microscopic resolution further, starting a pursuit for higher resolution limits [12]. His visionary ideas paved the way for the development of techniques capable of surpassing the diffraction limit, including tip-enhanced Raman spectroscopy (TERS) and photoluminescence TEPL [13–15].

TERS and TEPL represents a groundbreaking advancement in the field of spectroscopy, offering greater spatial resolution by combining the sensitivity of Raman or PL spectroscopy with the nanometer-scale resolution of scanning probe microscopy (SPM). The principle of TERS and TEPL involves localizing the excitation laser to a sharp metallic tip, thereby enhancing the Raman or PL signal from molecules or materials located in close proximity to the tip apex. This localized enhancement enables researchers to achieve spatial resolutions beyond the diffraction limit imposed by equation 1.1, opening new avenues for studying nanoscale phenomena in 2D materials. The limit now is in the order of the radius of the tip, which is in the order of tens of nanometers.

One important aspect of 2D materials is the study regarding defects [16, 17], which holds significant importance due to its direct implications on material properties and device performance. Defects such as vacancies, grain boundaries, edges, and dopants can significantly alter the electronic, optical, and mechanical properties of 2D materials. Understanding the formation, distribution, and impact of defects is crucial for tailoring the properties of 2D materials for specific applications. For instance, defects in graphene have been shown to affect its electronic transport properties, with vacancies acting as scattering centers for charge carriers [2,18]. Additionally, defects play a crucial role in the catalytic activity of 2D materials, with edge sites serving as active sites for various chemical reactions [19]. Characterizing defects in 2D materials requires advanced analytical techniques. Among them, TERS and TEPL can provide valuable information due to the gain in spatial resolution without loss of chemical information.

TERS can be also used to study the Raman coherence length (L_c) of graphene [20–23] and TMDs, which comes from the interference of Raman scattered photons. Typically, L_c is considerably smaller than the resolution limit imposed by equation 1.1 for conventional Raman measurements. TERS overcomes the resolution limit and the Raman scattered photons can interfere, translating into different enhancement factors for the Raman bands.

In this thesis, we explore the potential of TERS and TEPL as complementary techniques for studying the structural and optical properties of graphene and TMDs with spatial resolution in the order of tens of nanometers. The aim here is to utilize the distinct capabilities of these advanced spectroscopic methods to further explore 2D materials and potentially contribute to future technological advancements. The coherence length variation due to doping in graphene and TMDs, as well as nanoscale defects, edges, grain boundaries, wrinkles in TMDs are the

object of study.

1.1 Structure and organization

The thesis is organized in the following way:

In chapter 2, a definition of the materials that will be studied in the following chapters is done, i.e. graphene and transition metal dichalcogenides MoS_2, WS_2, $MoSe_2$ and WSe_2. It will also be presented the coherence in near field theory that will be used in the results chapters. Furthermore, a review in the literature on the papers that present TERS and TEPL of TMDs is done to pave the way for the advances done in the present thesis.

In chapter 3, the methodology used in the experiments is presented, that is, the sample preparation process that has to be specially tailored for TERS and TEPL. The experimental setup used in the TERS and TEPL measurements is also presented in this chapter.

In chapter 4, the first results achieved by this thesis are presented. A graphene device was patterned with a careful choice for the gate metal, which enables the detection of the Kohn anomaly in the graphene's G band at room temperature. Moreover, it is studied the influence of the electric field on graphene's TERS spectra. Finally, it is established the Raman coherence length dependence on doping and its origin (either phononic or electronic) is discussed.

In chapter 5, TERS spectra of the TMDs MoS_2, WS_2, $MoSe_2$ and WSe_2 are presented, and the theory for coherence is applied for the study of TMDs. Moreover, a series of localized emissions on the TMDs are presented, studying grain boundaries, wrinkles, substrate dependence, bubbles and localized defects in monolayers and twisted bilayers TMDs.

Finally, chapter 6 presents the conclusion and future perspectives that TERS and TEPL can further open in the study of materials science.

Chapter 2

Literature Review

In this chapter it will be discussed the novel results on TERS and TEPL of two dimensional materials, the theory used to understand and explain the results obtained in chapters 4 and 5, as well as some other aspects that were developed in this thesis.

2.1 Two-Dimensional Materials

Two-dimensional materials, a class of substances confined to a few layers of atoms, have emerged as an interesting field of study in materials science. These materials exhibit unique properties attributed to their reduced dimensionality, including remarkable electronic, optical, and mechanical characteristics [24,25]. For instance, graphene, which consists of a single layer of carbon atoms arranged in a hexagonal lattice, presenting exceptional electrical conductivity, thermal conductivity, and mechanical strength [2,26,27].

A broader category of two-dimensional materials is known as TMDs, such as MoS_2, WS_2, $MoSe_2$, and WSe_2. They consist of a transition metal layer sandwiched between two chalcogen layers, forming a hexagonal lattice structure and, when in monolayer form, they present unique electronic properties as 2D semiconductors [28].

2.1.1 Graphene

Graphene's hexagonal lattice is shown in Figure 2.1 (a). This material can exhibit a Raman response various ways, such as the stretching motion of the bonds between carbon atoms has energy corresponding to the G band (E_{2g}, $\approx 1585\,cm^{-1}$) and the breathing motion of the hexagon of carbon atoms corresponds to the so-called 2D band (A_{1g}, a second order feature at $\approx 2650\,cm^{-1}$ for the HeNe laser) [7] as shown in Figure 2.1 (b).

One important part, specially for the interpretation of the results in chapter 4, is the symmetry of the G and 2D phonon. Figure 2.1 (c) and (d) display a zoomed version of part (a), in which it displays the vibration correspondent to the G and 2D band, respectively. Since the G band corresponds to the C-C stretching [Figure 2.1 (c)], not all the symmetries are conserved. On the other hand, the 2D band is the breathing mode of the carbon atoms, preserving all the symmetries, hence it is a totally symmetric mode [29].

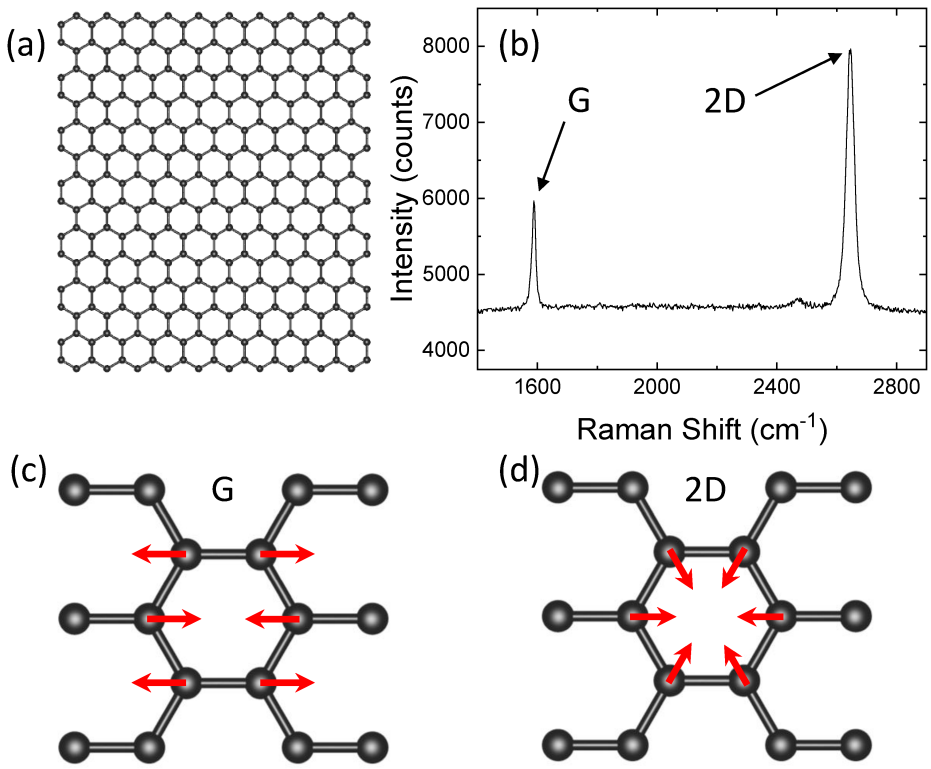

Figure 2.1: (a) Hexagonal lattice of graphene. Each sphere corresponds to a carbon atom. (b) Conventional Raman spectra of a graphene, taken using the HeNe laser, 5 accumulations of 5 s each, with 750 μW laser power. (c) and (d), zoomed version of panel (a), displaying as red arrows the vibration modes G and 2D, respectively.

There are other Raman peaks that are not going to be discussed here, but among them, one is important to highlight, the D band ($\approx 1330\,\mathrm{cm}^{-1}$). The D band will be discussed here because it is defect related and one focus of this work is the spatial resolution in TERS and TEPL. Since the border is a defect in the graphene lattice, the D band appears in it, being a good way to determine the spatial resolution in a TERS measurement [30]. Furthermore, small defects that are not visible in conventional Raman spectroscopy, when doing TERS, the D band attests their existence.

2.1.1.1 Electric field influence in graphene's Raman spectra

In order to understand the electric field influence in graphene's Raman spectra, first it is important to understand the electron-phonon interaction, how it is usually treated and how it is different for graphene [7]. Normally, vibrations in materials are explained using the so-called Born-Oppenheimer (adiabatic) approximation, that is, when electrons are moving fast enough so that they can follow the movement of the nuclei in the vibration. However, if the nuclei motion is faster than the time needed for electronic relaxation, the adiabatic approximation is not valid anymore.

The time for electronic relaxation in graphene is in the order of hundreds of femtoseconds [31, 32], while the time for the atomic movement in the G band vibration is $\approx$22 fs [33].

Therefore, the electrons do not have time to relax, breaking the adiabatic approximation, resulting in a strong electron-phonon coupling and a G-band dependence on electronic doping and temperature.

First, let's discuss the temperature effect on phonons. The G phonon frequency (ω_G) dependence with temperature is given by:

$$\omega_G = \omega_G^0 + \chi T, \tag{2.1}$$

in which $\chi = -0.0162\,\mathrm{cm}^{-1}/\mathrm{K}$ [34] is the first order coefficient for the temperature dependent correction to ω_G and $\omega_G^0 = 1584\,\mathrm{cm}^{-1}$ [34] is the G phonon frequency when $T \to 0$ in graphene. In reference [34] the authors identify this shift in frequency varying temperature due to thermal expansion of the lattice and to the so-called self energy shift due to anharmonic coupling of the phonon modes,

$$\omega_G - \omega_G^0 = (\chi_T + \chi_V)\Delta T, \tag{2.2}$$

where χ_T and χ_V corresponds to the self-energy and thermal expansion contributions, respectively.

It is clear in equation 2.2 that the phonon frequency depends linearly with the temperature variation and the change is very small (ΔT=100K varies ω_g by $1.6\mathrm{cm}^{-1}$) [34]. Nevertheless, the temperature dependence is also important when considering the electron-phonon coupling and the electronic population varying in a crystalline structure. The Fermi-Dirac distribution gives the probability that an orbital with energy E is occupied in an ideal electron gas in thermal equilibrium

$$f(E) = \frac{1}{e^{(E-\mu)/k_BT} + 1}, \tag{2.3}$$

where k_B is the Boltzman constant and μ is the chemical potential. This changes in number of occupants will directly affect the G phonon frequency shift as it will be discussed further.

Once we have established the temperature dependence, let's consider the phonon frequency renormalization within the context of the perturbation theory. Here, the electron-phonon interaction is considered a perturbation where the phonon can excite an electron-hole pair, renormalizing the phonon energy depending on the Fermi level, electronic structure and temperature [35–37]. After that, the phonons renomarlize the electron energies and vice-versa [see Figure 2.2 (a)]. Thus, one can control this energy (frequency) shift with a gate voltage (see chapter 4).

From the second order perturbation theory one can calculate the phonon energy shift for the G band due to the electron-phonon interaction

$$\hbar\omega_\lambda = \hbar\omega_\lambda^{(0)} + \hbar\omega_\lambda^{(2)}, \tag{2.4}$$

where λ corresponds to the optical branch in the phonon dispersion (LO or iTO), $\hbar\omega_\lambda^{(0)}$ is the phonon energy without the electron-phonon interaction and $\hbar\omega_\lambda^{(2)}$ is the electron-phonon

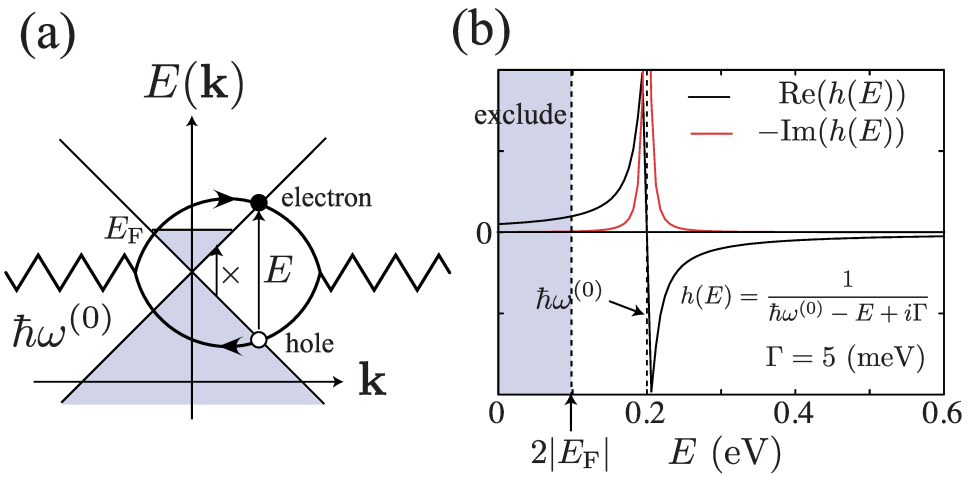

Figure 2.2: (a) An intermediate state involving an electron–hole pair that contributes to the shift in energy of the optical phonon modes. A zigzag line represents a phonon mode, while a loop signifies an electron–hole pair. The Pauli principle prohibits the existence of a low-energy electron–hole pair with $0 \leq E \leq 2E_F$ at zero temperature. (b) The real and imaginary components of the energy-dependent correction, denoted by h(E), to the phonon energy due to the intermediate electron–hole pair state. Notably, the sign of the correction depends on the energy of the intermediate state as determined by equation 2.6. Figure taken from [38].

perturbation given by the second order perturbation theory:

$$\hbar\omega_\lambda^{(2)} = 2\sum_k \frac{|<\mathrm{eh}(\mathbf{k})|\mathcal{H}_{int}|\omega_\lambda>|^2}{\hbar\omega_\lambda^{(0)} - (E_\mathrm{e}(\mathbf{k}) - E_\mathrm{h}(\mathbf{k})) + i\Gamma_\lambda} \times [f(E_\mathrm{h}(\mathbf{k}) - E_\mathrm{F}) - f(E_\mathrm{e}(\mathbf{k}) - E_\mathrm{F})], \quad (2.5)$$

where the factor 2 in front is due to spin degeneracy, $<\mathrm{eh}(\mathbf{k})|\mathcal{H}_{int}|\omega_\lambda>$ is the matrix element for the creation of an electron-hole pair at the momentum $\mathbf{k}$ by the electron-phonon interaction with $q = 0$ phonon, E_e and E_h are, respectively, the electron and hole energies and Γ_λ is the decay width.

As $<\mathrm{eh}(\mathbf{k})|\mathcal{H}_{int}|\omega_\lambda>$ is a smooth function of $E = E_\mathrm{e}(\mathbf{k}) - E_\mathrm{h}(\mathbf{k})$, the impact of an electron–hole pair on $\hbar\omega_\lambda^{(2)}$ is significantly influenced by its energy. In Figure 2.2 (b), it is graphically represented both the real and imaginary components of the denominator of equation 2.5, denoted as

$$h(E) = \frac{1}{(\hbar\omega_\lambda^{(0)} + E + i\Gamma_\lambda)}. \quad (2.6)$$

This analysis is conducted for the scenario where $\hbar\omega_\lambda^{(0)}$ equals 0.2 eV and Γ is set to 5 meV. In the case where E is less than $\hbar\omega_\lambda^{(0)}$ (greater than $\hbar\omega_\lambda^{(0)}$), Re[h(E)] exhibits a positive (negative) value, and the electron–hole pair with lower (higher) energy positively (negatively) influences $\hbar\omega_\lambda^{(2)}$. Additionally, an electron–hole pair with $E < 2|E_F|$ cannot contribute to the energy shift due to the presence of the Fermi distribution function $f(E)$ in equation 2.5. Consequently, the quantum correction to the phonon energy by an intermediate electron–hole pair can be manipulated by adjusting the Fermi energy. For instance, when $|E_F| = \hbar\omega_\lambda^{(0)}/2$, $\hbar\omega_\lambda^{(2)}$

reaches a minimum value at zero temperature since all positive contributions are suppressed in equation 2.5. This phenomenon is displayed in the calculation of the frequency shift in Figure 2.3 (b).

The non-zero presence of $\mathrm{Im}(h(E))$ shown in Figure 2.2 (b) occurs only in close proximity to $E = \hbar\omega^{(0)}$, indicating that the phonon can undergo resonant decay into an electron-hole pair possessing the same energy as the phonon. It is worth mentioning that when $|E_F| > \hbar\omega^{(0)}/2$, the width of the resonance window is narrow, leading to $\Gamma_\lambda \approx 0$ at zero temperature. However, at a finite temperature, Γ_λ may assume a non-zero value. Figure 2.3 (a) is obtained through the self-consistent calculation of $\Gamma_\lambda = -\mathrm{Im}(\hbar\omega_\lambda^{(2)})$ in equation 2.5. Additionally, Figure 2.3 (a) demonstrates the expected behavior of the G-band FWHM as the electron concentration (Fermi level) varies.

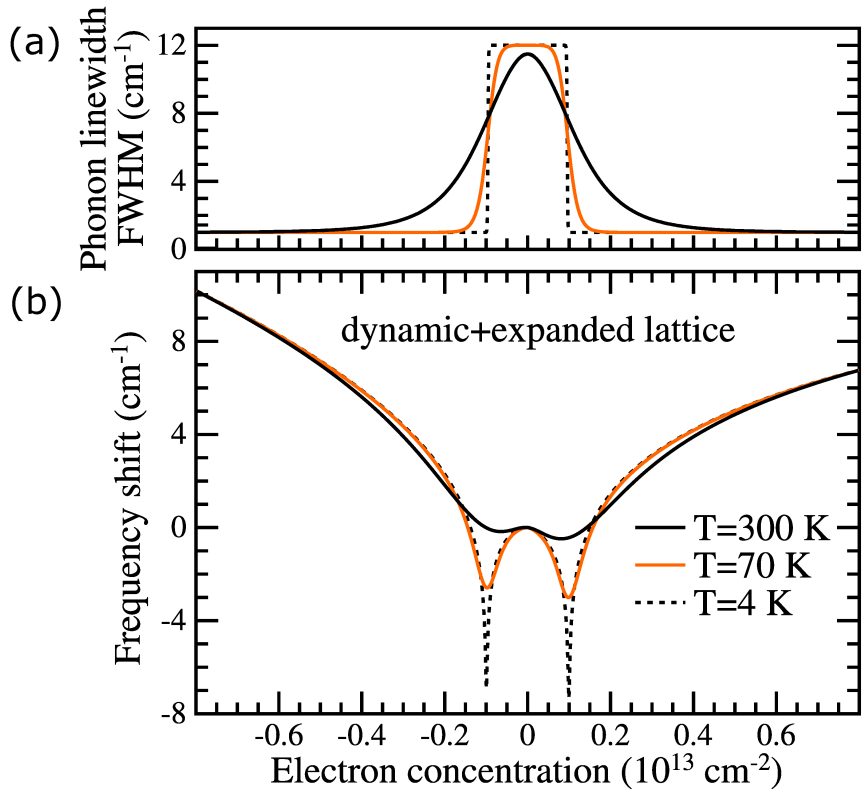

Figure 2.3: (a) Imaginary and (b) real part of equation 2.5. It displays the calculation of the (a) FWHM and (b) frequency shift of the G-band in graphene as a function of the number of charge carriers for T = 300 K, 70 K, and 4 K. Figure from [37].

In Figure 2.3 it is illustrated the impact of temperature variation on phonon renormalization, as indicated by distinct line styles, given by the Fermi distribution-related term in 2.5. At $T = 0$, $f(E) = 1$ up to the Fermi level, beyond which $f(E) = 0$. This results in a singular dependence for phonon renormalization and linewidth variation at $E_F = \pm\hbar\omega_G/2$, as shown in Figures 2.3 (a) and (b). As the temperature rises, the occupancy probability exhibits a broader distribution around E_F, effectively smoothing out the singularities at $E_F = \pm\hbar\omega_G/2$.

This phenomenon is a direct consequence of the Kohn anomaly [39] and it has already been observed in the literature [36, 40]. The w-shape near the neutrality between $E_F = \pm\hbar\omega_G/2$ is

reported in the literature for low temperatures for the ω_g dependence on doping [41]. However, it is difficult to observe this phenomenon at room temperature due to the Fermi distribution effect at 300 K. For more on that topic, see chapter 4.

2.1.2 Transition Metal Dichalcogenides

Transition metal dichalcogenides (TMDs) are a class of two-dimensional materials that have been widely studied in recent years due to their remarkable electronic and optical properties [3–5]. TMDs consist of a transition metal atom in between two layers of chalcogen atoms, forming a hexagonal lattice [9] [Figure 2.4 (a)]. This structure gives rise to interesting properties, among them the existance of a sizable bandgap [42] and the potential for strong excitonic effects [43]. As a result, TMDs have emerged as promising materials for a wide range of applications, from next-generation electronic and optoelectronic devices to catalysis and sensing [3, 44, 45]. Understanding the vibrational and electronic properties of TMDs is fundamental for exploiting their potential in various applications.

Unlike graphene, the A and E symmetry phonons are both active first order Raman modes very close to the Γ point. Furthermore, while graphene has only in-plane modes, TMDs present off-plane modes [46]. This can be seen in Figure 2.4 (b), in which it is shown a side view of the TMDs crystal structure. While the E_{2g} mode is in-plane, the A_{1g} mode is off-plane.

Materials belonging to different point group symmetries will have different nomenclatures for the totally symmetric mode (always coming with an A) and non-symmetric modes. In the Schoenfles notation in group theory [29], the letter A means that the mode is not degenerate and it is symmetric with respect to the rotation of the principal axis. The letter E means that the mode is double degenerate. The subscript 1 means it is symmetric with respect to the C_n principle axis, while the subscript 2 means it is anti-symmetric with respect to the C_n principle axis. Subscript g (for gerade) means that the mode is symmetric with respect to the inverse, and the superscript prime (') means it is symmetric with respect to the reflection in the horizontal plane.

In the bulk form, TMDs belong to the D_{6h} point group, but when in monolayer (and few-layers), due to lack of translational symmetry in the z-axis, the symmetry is reduced to the D_{3h} point group (for odd number of layers. For even number it is reduced to the D_{3d} point group). Therefore, when in bulk all TMDs present A_{1g} and E_{2g} Raman peaks, but when in monolayer, these peaks become A_1' and E' symmetry modes [150]. In this work, we will use different assignments for these peaks (A_{1g}, E_{2g}, A', E', A, E) to match the references used for the assignments, but the symmetries explained in this paragraph are valid for all TMDs.

Figure 2.4 (c) displays the Raman spectra of the TMDs MoS_2, WS_2, $MoSe_2$ and WSe_2 monolayers. The first order peaks A and E are highlighted. Again, unlike graphene, many other second order peaks appear in the spectra, making it harder to isolate and study them. In particular, besides the many other peaks in the spectrum, the A and E peaks are almost degenerate in WSe_2, which hinders the TERS analysis (see chapter 5).

Another important property of TMDs is that they are an indirect semi-conductor when in

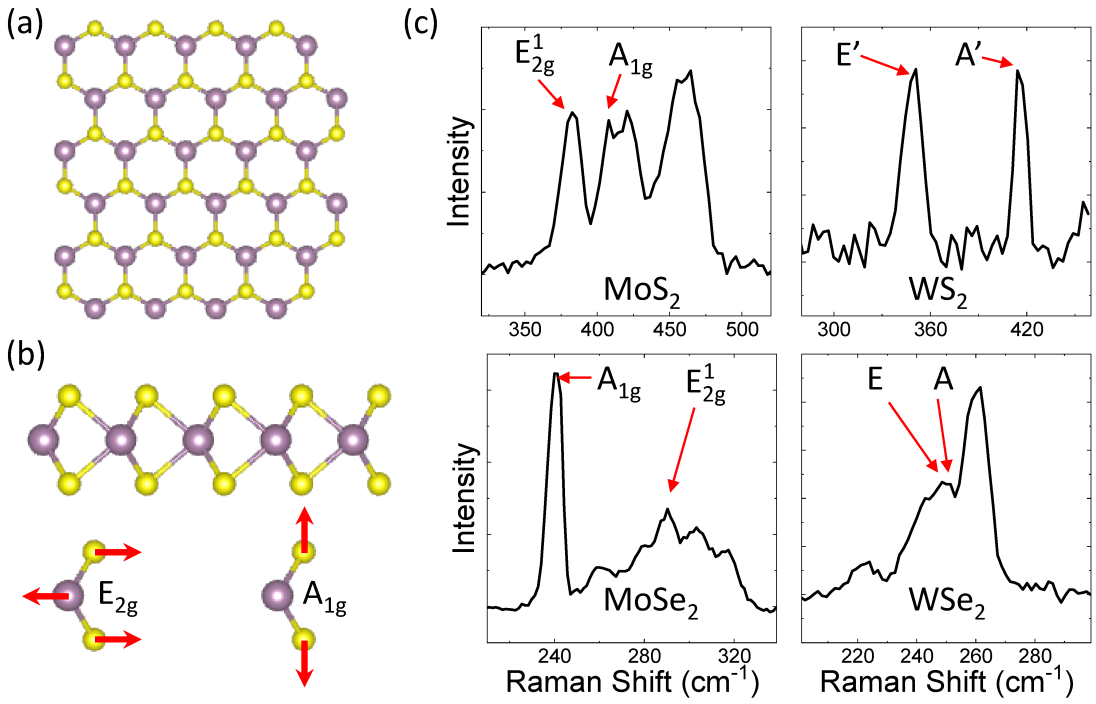

Figure 2.4: Top-view of TMDs crystal structure. The purple atoms are the transition metal (Mo or W) and the yellow atoms are the chalcogens (S or Se). (b) Side view of the TMDs crystal structure. At the bottom it is displayed the two first order Raman modes E_{2g} and A_{2g}. Here, unlike graphene, the A mode is off-plane while the E mode is in-plane. (c) Raman spectra of the TMDs MoS_2, WS_2, $MoSe_2$ and WSe_2 monolayers. Here, many other second order peaks appear due to the laser used (632.8 nm).

many layers form, but they become a direct bandgap when in monolayer form [9, 42]. Figure 2.5 displays the photoluminescence (PL) of (a) MoS_2, (c) $MoSe_2$ and (d) WSe_2. Here, the HeNe (632.8 nm) is used, being the reason for the WS_2 spectra (b) being cropped: while the other TMDs have emissions in the near infrared, WS_2 band gap is on top of the laser energy [47], being cropped by the long pass filter (see Figure 3.3). Thus, we only observe one side of the PL. Because of the laser used, the Raman spectra is also visible in the same frame as the PL, and it is marked as a red circle in Figure 2.5. Since every sample interacts differently with each laser, different experimental parameters were used to acquire the spectra, see details in Figure 2.5 caption.

In Figure 2.5 (a) and (b) one can use a higher spectral resolution spectrometer grating (600 and 1200 l/mm, respectively), resolving the Raman spectrum better (WS_2 has a very high PL intensity for low excitation power for the HeNe laser due to resonance phenomena [48]). For the others [Figure 2.5 (c) and (d)] one needs a lower spectral resolution spectrometer grating (300 l/mm). Particularly, in panel (d), WSe_2 PL spectrum is so intense that in order to see the Raman one has to multiply by 500 times.

Finally, another hot topic on TMDs is the effect of defects. TMDs samples grown to the large area required for industrial-scale applications commonly exhibit defects such as vacancies, strain fields, electrical and chemical doping, grain boundaries, and surface ad-

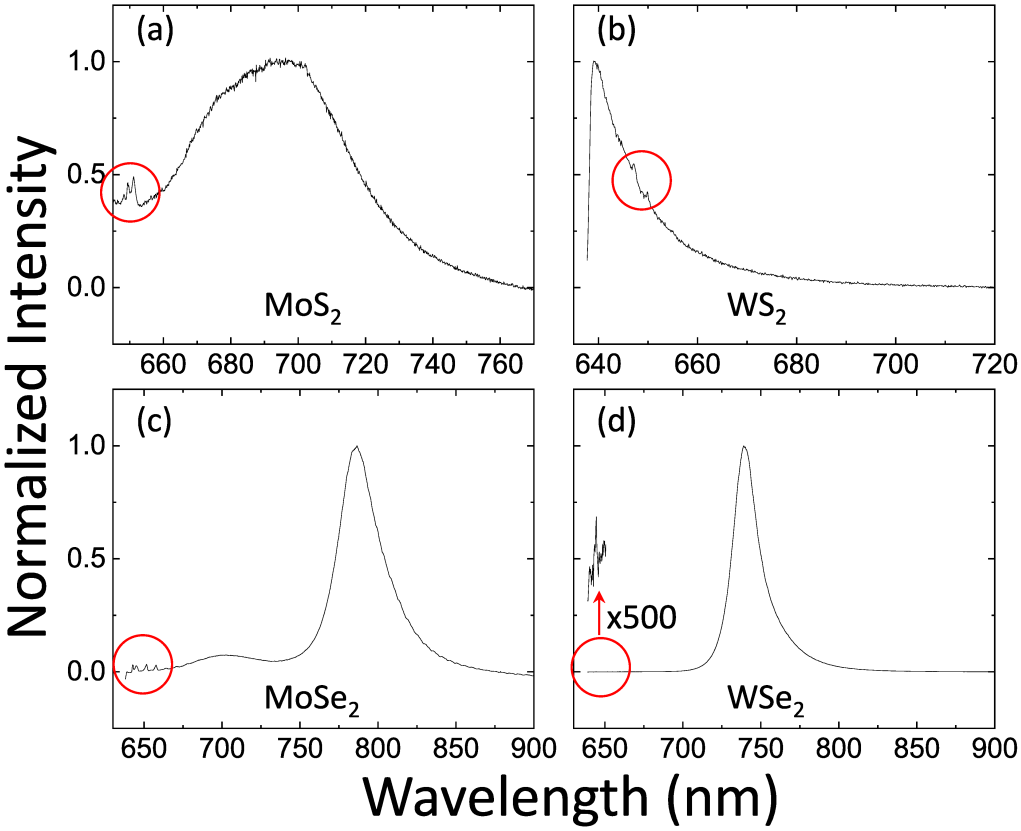

Figure 2.5: PL spectra of TMDs (a) MoS_2, (b) WS_2, (c) $MoSe_2$ and (d) WSe_2. The red circles highlights the Raman signal that is also visible in the PL spectra, even in (d) where in order to see it one had to multiply it by 500 times. The vertical line in panel (b) is due to the long pass filter in our experimental setup. Since every sample interacts differently with each laser, different experimental parameters were used to acquire the spectra; (a) 200 μW, (b) 1.92 μW and (c) 200 μW were done in 5 accumulations of 5 s each while (d) 20 μW was done in 30 accumulations of 0.5 s each.

sorbents [16]. These defects are associated with modifications in optical and electronic properties, significantly impacting the performance of TMDs in devices [49]. Conversely, there is a substantial effort focused on defect engineering in these 2D TMDs to achieve novel and desirable properties [16, 17]. Therefore, characterizing these defects is crucial, not only to aid in the development of their growth methods but also to study the intentional tuning of their properties. These phonomena can also be characterized using TERS and TEPL, and the first steps towards it are taken in this thesis.

2.2 Scanning near-field optical microscopy

The scanning near-field optical microscopy (SNOM) technique essentially involves the combination of an optical technique (i.e. Raman or PL spectroscopy) with a scanning probe coupled to it [50]. In this work, I will focus on a specific type of SNOM, which is composed of an inverted confocal optical microscope with an atomic force microscopy (AFM) scanhead coupled to it, allowing for the scanning of a probe over a sample to study the near-field char-

acteristics when bringing a tip very close to the sample. The tips (or nano antennas [51, 52]) are metallic, leading to a plasmonic resonance at the tip apex [53]. Typically, these tips are made using silicon AFM tips coated with gold or silver, or cantilevers with a metal nanowire at the tip [54]. They can also be produced through the corrosion of metal wires [55] or by evaporating metals onto corroded silicon templates [56].

2.2.1 Coherence in two-dimensional systems

In this section it will be shown the effects of coherence in the Raman scattered photons during a TERS measurement. Raman scattering in crystals is conventionally discussed in the literature as a spatial incoherent phenomenon [57, 58]. This implies that the scattered field originating from different points within the sample is considered to be spatially uncorrelated. This understanding aligns with early coherence theories, which propose that the field emitted by an incoherent source at a specific wavelength λ lacks spatial correlation on scales larger than $\lambda/2$ (measured from the scatterer's surface) [59]. As a result, standard light scattering methods typically cannot access correlations on scales smaller than $\lambda/2$, resulting in an incoherent signal detected in the far field.

However, with the emergence of near-field optics and advancements in nanoscience, investigations into thermal emitters have revealed correlation lengths significantly shorter than λ [60–64]. In this context, we demonstrate that similar principles govern near-field Raman scattering, indicating that correlation lengths much smaller than $\lambda/2$ can be discerned from experimental data. Consequently, the analysis of near-field Raman scattering needs consideration of subwavelength correlations and the associated interference phenomena.

Here, the tip will be considered a dipole that approaches very close to the sample (≈ 5 nm) and that it acts as an antenna to transform the evanescent into propagating field.

First, the Raman polarizability is given by

$$\overleftrightarrow{\alpha}^{\gamma}_{ij}(r;\omega_s,\omega) = \sum_{k=x,y,z} \frac{\partial \alpha_{ij}(\mathbf{r},\omega)}{\partial q_k} q_k \tag{2.7}$$

where γ labels the Raman mode responsible for the virtual mode $\mathbf{q}$ of the crystal lattice, with frequency $|\omega - \omega_s|$. Now, the intensity measured in the detector at the position $\mathbf{r}_0$ can be calculated as the ensemble average of the scattered signal in the form of

$$S(\mathbf{r}_0;\omega_s) = \langle E^{s*}(\mathbf{r}_0;\omega_s) E(\mathbf{r})_0;\omega_s)\rangle \tag{2.8}$$

$$\begin{aligned} S(\mathbf{r}_0;\omega_s) = \frac{\omega_s^4}{\varepsilon_0^2 c^4} \sum_{l,m,n} \sum_{i,j} \int_{\mathbb{D}} d^3\mathbf{r}_2 \int_{\mathbb{D}} d^3\mathbf{r}_1 \langle \overleftrightarrow{\alpha}^{\gamma*}_{mi}(\mathbf{r}_1;\omega_s) \overleftrightarrow{\alpha}^{\gamma*}_{nj}(\mathbf{r}_2;\omega_s)\rangle \\ \times G^*_{lm}(\mathbf{r}_0,\mathbf{r}_1;\omega_s) G^*_{ln}(\mathbf{r}_0,\mathbf{r}_2;\omega_s) E^*_i(\mathbf{r}_1,\omega) E^*_j(\mathbf{r}_2,\omega). \end{aligned} \tag{2.9}$$

Here, the term $\langle \overleftrightarrow{\alpha}^{\gamma*}_{mi}(\mathbf{r}_1;\omega_s) \overleftrightarrow{\alpha}^{\gamma*}_{nj}(\mathbf{r}_2;\omega_s)\rangle$ is responsible for the correlation between the scattered fields. In conventional Raman spectroscopy, it is considered that the fields do not

interfere, replacing this term for a Dirac delta, and equation 2.9 can be solved to:

$$S(r_0;\omega_s) = V_{\mathbb{D}}\Omega\frac{\omega_s^4}{\varepsilon_0^2 c^4}\left|\hat{\varepsilon}_s.\overleftrightarrow{\alpha}^{\gamma}(\omega_s,\omega)\mathbf{E}(\omega)\right|^2, \tag{2.10}$$

in which Ω is the experimental solid angle, $V_{\mathbb{D}}$ is the scattering volume and $\hat{\varepsilon}_s$ is a unit vector that defines the polarization of the scattered field.

However, if the fields do interfere, i.e., the experiment takes place inside the Raman coherence length, in reference [20] the authors argument that the correlation term can be replaced by a Gaussian function with the form

$$\overleftrightarrow{\alpha}^{\gamma*}_{mi}(\mathbf{r}_1;\omega_s)\overleftrightarrow{\alpha}^{\gamma*}_{nj}(\mathbf{r}_2;\omega_s)\rangle = \tilde{\alpha}^{\gamma*}_{mi}(\mathbf{r}_1;\omega_s)\tilde{\alpha}^{\gamma*}_{nj}(\mathbf{r}_1;\omega_s)\frac{e^{-(|\mathbf{r}_1-\mathbf{r}_2|/L_c^2)}}{\pi L_c^2}. \tag{2.11}$$

Note the L_c appears defining the width of the Gaussian term. We can now insert equation 2.11 into equation 2.9 for a two-dimensional system where the scattering modes occur on the plane of the sample (such as graphene)

$$\begin{aligned} S(\mathbf{r}_0;\omega_s) = {} & \frac{\omega_s^4}{\varepsilon_0^2 c^4}\sum_{l,m,n}\sum_{i,j}\iint_{-\infty}^{+\infty} dx_2 dy_2 G_{ln}(\mathbf{r}_0,x_2,y_2;\omega_s)\tilde{\alpha}^{\gamma*}_{nj}E_j(x_2,y_2,\omega) \\ & \times\iint_{-\infty}^{+\infty} dx_1 dy_1 \frac{e^{-[(x_1-x_2)^2+(y_1-y_2)^2/L_c^2]}}{\pi L_c^2} G^*_{lm}(\mathbf{r}_0,x_1,y_1;\omega_s)\tilde{\alpha}^{\gamma*}_{mi}E^*_i(x_1,y_1,\omega), \end{aligned} \tag{2.12}$$

with $l \in \{x,y,z\}$ and $m,n;i,j \in \{x,y\}$.

Defining the tip's polarizability as

$$\overleftrightarrow{\alpha}_{tip}(\mathbf{r}') = \begin{pmatrix} \alpha_\perp & 0 & 0 \\ 0 & \alpha_\perp & 0 \\ 0 & 0 & \alpha_{||} \end{pmatrix}, \tag{2.13}$$

where $\alpha_\perp$ and $\alpha_{||}$ corresponds to the transverse and longitudinal polarizabilities [65]

$$\alpha_\perp(\omega) = 4\pi\varepsilon_0 r_{tip}^3\frac{\varepsilon(\omega)-1}{\varepsilon(\omega)+2}, \tag{2.14}$$

$$\alpha_{||}(\omega) = 2\pi\varepsilon_0 r_{tip}^3 f_e(\omega), \tag{2.15}$$

where r_{tip} is the tip's radius, ε is the tip's dielectric constant and f_e is the tip's enhancement factor.

The electric field when interacting with the tip generates a dipole

$$\mathbf{p} = \overleftrightarrow{\alpha}_{tip}\mathbf{E}, \tag{2.16}$$

thus

$$\overleftrightarrow{G}(\mathbf{r}_0,\mathbf{r};\omega_s) = \overleftrightarrow{G}^{0}(\mathbf{r}_0,\mathbf{r};\omega_s) + \frac{\omega_s^2}{\varepsilon_0 c^2}\overleftrightarrow{G}^{0}(\mathbf{r}_0,\mathbf{r};\omega_s)\overleftrightarrow{\alpha}_{tip}(\mathbf{r'};\omega_s)\overleftrightarrow{G}^{0}(\mathbf{r'},\mathbf{r};\omega_s), \tag{2.17}$$

$$\mathbf{E}(\mathbf{r},\omega) = \mathbf{E}_0(\mathbf{r},\omega) + \frac{\omega_s^2}{\varepsilon_0 c^2}\overleftrightarrow{G}^{0}(\mathbf{r},\mathbf{r'};\omega)\overleftrightarrow{\alpha}_{tip}(\omega)\mathbf{E}_0(\mathbf{r'},\omega). \tag{2.18}$$

where $\mathbf{r'} = (0,0,z)$ and $\mathbf{r} = (x,y,0)$ are the positions of the tip and the sample, respectively. Combining equations 2.17 and 2.18, and assuming that $|\alpha_{||}| \gg |\alpha_{\perp}|$,

$$\begin{aligned} G_{ln}(\mathbf{r}_0,x,y;\omega_s)\alpha^{\gamma}_{nj}(x,y,\omega)E_j(x,y,\omega) &= G^0_{ln}(\mathbf{r}_0,x,y;\omega_s)\alpha^{\gamma}_{nj}E_{0j}(x,y,\omega) \\ &+\frac{\omega_s^2}{\varepsilon_0 c^2}G^0_{lz}(\mathbf{r}_0,z';\omega_s)\alpha_{||}(\omega_s)G^0_{zn}(z',x,y;\omega_s)\alpha^{\gamma}_{nj}(x,y,\omega)E_{0j}(x,y,\omega) \\ &+\frac{\omega^2}{\varepsilon_0 c^2}G^0_{ln}(\mathbf{r}_0,x,y,\omega_s)\alpha^{\gamma}_{nj}(x,y,\omega)G^0_{jz}(x,y,z';\omega)\alpha_{||}(\omega)E_{0z}(z',\omega) \\ +\frac{\omega^2\omega_s^2}{\varepsilon_0^2 c^4}G^0_{lz}(\mathbf{r}_0,z';\omega_s)\alpha_{||}(\omega_s)G^0_{zn}(z',x,y;\omega_s)\alpha^{\gamma}_{nj}(x,y,\omega)G_{jz}(x,y,z';\omega)\alpha_{||}(\omega)E_{0z}(z',\omega). \end{aligned} \tag{2.19}$$

One can identify the electric field E_{em} as the sum of the scattering modes

$$E_{em} = E_S + E_T + E_{ST} + E_{TS} + E_{STS} + E_{TST} + ..., \tag{2.20}$$

where E_S and E_T are the electric fields scattered, respectively, by the sample (S) and by the tip (T). The subsequent terms correspond to interactions that, in the case of E_{ST}, for example, interact with the tip and then with the sample, and higher-order terms follow the same logic.

Thus, equation 2.19 represents the scattering modes presented in equation 2.20, being the first term S, followed by the TS, ST and TST modes, respectively. In reference [20] the authors assumed that the TS term is small in comparison to the ST term. Thus, they only considered the TST and ST terms in the calculation. However, in reference [22] the authors included the TS term, as we did here.

Following the calculations in reference [22], one can compactly calculate the intensity of a Raman mode to be

$$I^{\mathrm{TERS}}_{\gamma}(z) = C_{\gamma}\{f_e^4 r_{\mathrm{tip}}^{12} g^{\mathrm{TST}}_{\gamma}(L_{\mathrm{c}},z) + f_e^2 r_{\mathrm{tip}}^{6}[g^{\mathrm{ST}}_{\gamma}(L_{\mathrm{c}},z) + g^{\mathrm{TS}}_{\gamma}(L_{\mathrm{c}},z)]\}, \tag{2.21}$$

where $I^{\mathrm{TERS}}_{\gamma}$ denotes the TERS intensity of graphene as a function of tip-sample distance (z) for the phonon mode γ = G or 2D. C_{γ} is the Raman cross section, f_{e} the tip enhancement factor and r_{tip} the tip radius. Note that L_{c} is a parameter for $g^{\mathrm{TST}}_{\gamma}$ and $g^{\mathrm{ST,TS}}_{\gamma}$, corresponding to the tip-sample-tip (TST) and tip-sample, sample-tip (ST, TS) scattering functions, calculated using Green's function formalism, as defined in Ref. [22].

Using graphene as an example, Figure 2.6 (a) and (b) (from reference [22]) displays the influence of the TS (red), ST (black) and TST (blue) modes in the graphene Raman A_{1g} and

E_{2g} modes. Here, it is important to highlight that the ST scattering mode dominates the E_{2g} mode due to destructive near field interference happening on the other modes (see chapter 4 for further discussion on this).

One way to test the theory, is by doing the approach curve experiment (refer to section 4.3 to see the full explanation on how this experiment is done). Here, seven of such experiments were performed with the same tip, in the same position in graphene. The data were acquired and we can plot the quantity $(I^{TERS}_{A_1}/I^{FF}_{A_1})/(I^{TERS}_{E_{2g}}/I^{FF}_{E_{2g}})$ and fit using equation 2.21 to acquire L_c. With a statistical analysis, one can find $r_{tip} = (31 \pm 6)$ nm, $f_e = 4.5 \pm 0.8$ and $L_c = (26 \pm 4)$ nm, which are all reasonable values and with good experimental uncertainties, validating the experiment for determining L_c.

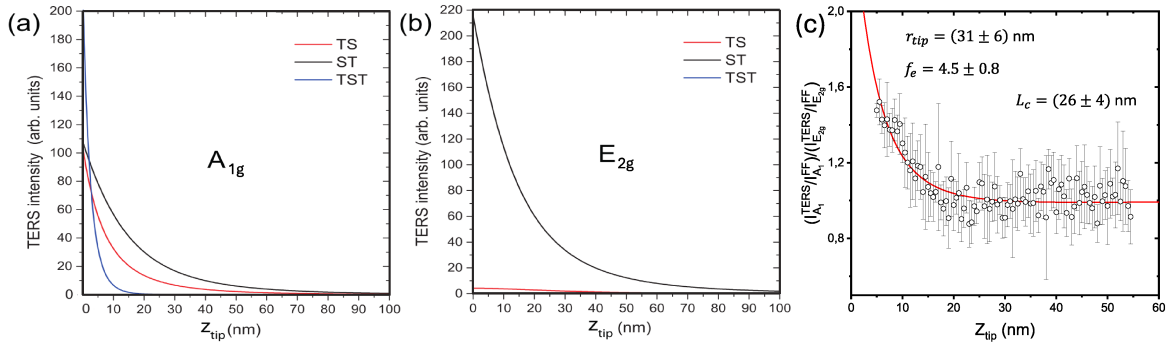

Figure 2.6: TS (red), ST (black) and TST (blue) influence in the (a) A_{1g} and (b) E_{2g} modes. The influence of the ST mode is much more evident in the E_{2g} case due to destructive interference happening at the TST and ST processes. (c) Experimental measurement of seven approach curve experiments, performed with the same tip in the same location of a graphene sample. Values for r_{tip}, f_e and L_c are displayed. Parts (a) and (b) were taken from reference [22].

2.2.2 TERS and TEPL in two-dimensional materials

In this subsection it will be presented the state of the art of works investigating the materials presented in section 2.1.

Initially, regarding carbon-based materials, one-dimensional (1D) carbon nanotubes were investigated in TERS [66–70], primarily because of their pronounced resonant Raman characteristics linked to their one-dimensional structure. More recently, TERS has also been employed to study a single carbyne chain confined inside a double-walled carbon nanotube [71]. Subsequently, two-dimensional (2D) graphene emerged as a key player in the advancement of both the principles and applications of TERS, that will be further studied.

Figure 2.7 (a) shows one of the highest enhancements in a 2D graphene flake ever recorded. The 2D band presented an spectral enhancement of $\approx$ 100 times with the aid of the plasmon tunable tip pyramid (PTTP - refer to section 3.2 for details). Note that, in this spectrum, the defect related D band appears when the tip is engaged, but it is absent without the tip, even when multiplying the far-field spectra by 500 times [inset of Figure 2.7 (a)]. This is due to a defect island invisible with micro-Raman that shines in the presence of the tip. Figure 2.7 (b)

and (d) displays the D band region intensity map inside a 100 x 100 nm region with (b) and without (d) the tip. Here, it is noticeable that the defect is in the order of ≈30 nm [Figure 2.7 (c)], which is indeed only visible in nano-Raman. Figure 2.7 (e) displays the spectra of the three different points (P1 - green, P2 - magenta and P3 - red) in panel (b), displaying the highly intense D band in P2, no D band and P1 and a dimer intense D band in P3, showing that in the region there are more than one defect island. Figure 2.7 (f) displays the AFM measurement of (b), where no significant topography features matching with the optical images are observed.

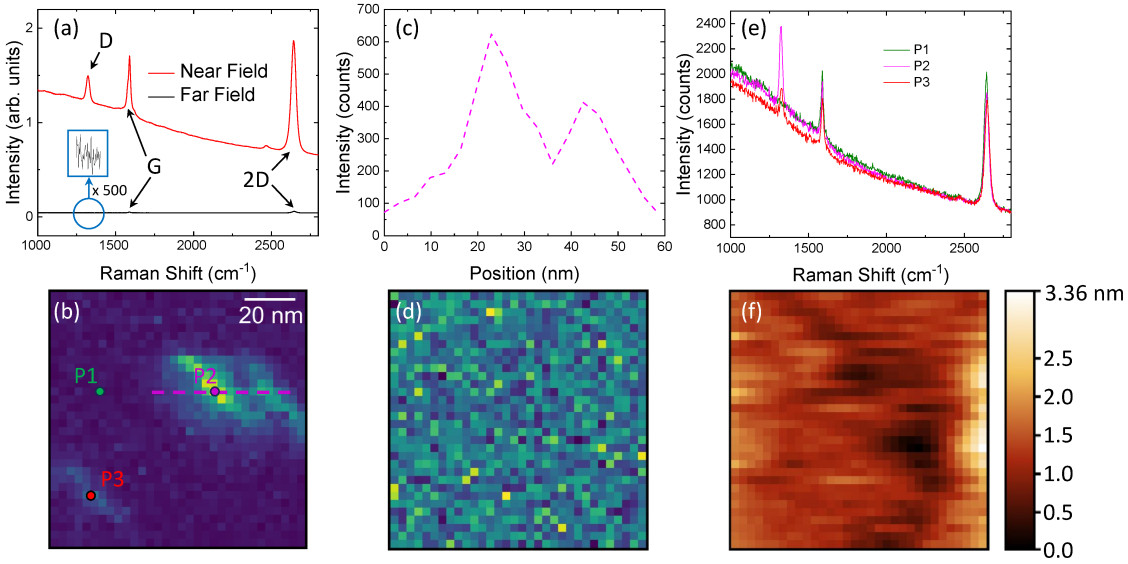

Figure 2.7: TERS measurements of a graphene sheet. (a) Near field (red) and far field (black) measurements. The spectral enhancement is in the order of ≈100 times with both spectra taken with 5 accumulations of 5 s each with 200 μW laser power. It is noticeable that the D band only appears in the near field spectrum, even when we multiply the far field data by a factor of 500 (inset). (b) Near field map of a 100x100 nm area of the D band region intensity. Map performed with 32 points per line/column, 0.5 s per pixel, 200 μW laser power. (c) A line profile of the D band in the magenta colored line in panel (b), showing that the defect is in the order of ≈30 nm. (d) Far field map of the same region as (b) performed with the same parameters, showing that the D band feature only appears with the presence of the tip. (e) spectra from points P1 (green), P2 (magenta) and P3 (red) that are displayed in panel (b). It is clear that in point P1, no D band is observed, whereas in P2 and P3, the D band shines. Note that P3 is less intense than P1, making it a region with fewer defects. (f) AFM of the same region, with no clear feature that resembles the morphology of the defect, indicating that there might be a vacancy defect island.

TERS has also been employed to detect local strain and doping in graphene devices with in-plane homojunctions, constructed as van der Waals heterostructures, where the graphene is partially supported by talc and partially by SiO_2 [72]. The spatial resolution of TERS makes the visualization of the charge depletion region at the interface between distinct substrates possible. Moreover, local strain and doping may arise from the presence of particles in the substrate [73] or from non-uniform deposition when producing twisted bilayer graphene [74]. Such non-uniformity is detectable only through nano-Raman, as it is averaged out in conventional micro-Raman analysis [74].

After graphene, the TMD MoS_2 is the most studied 2D material using TERS and TEPL [75–83]. The first report of tip-enhanced measurements in MoS_2 shows a nanoscale mapping of excitons and trions by combining TERS and TEPL, with a spatial resolution of less than 20 nm [76]. The authors also investigated doping by using Ag and Au coated tips and found that the type of doping depends on the work function of the metal, n-doping for Ag and p-doping for Au. Thus, using an Ag coated tip, it was possible to create a TEPL mapping of the A^0 exciton and for the A^- and B^- trions in a single layer MoS_2. Following this work, other authors contributed to the development of the field. For instance, a giant gap-mode TERS was performed in MoS_2 with the aid of a nanocluster array on the substrate [78]. As shown in Figure 2.8 (a), a 10^8 enhancement was observed for the A_{1g} peak. Notice the A_{1g} enhanced much more than the E_{2g}, consistent with the near-field coherence effect discussed for graphene [20, 22, 23, 84]. This large enhancement is credited to the presence of nanodisks of gold on the substrate [displayed on the right side of Figure 2.8 (a)], creating the gap-mode regime that provides high enhancement on the edges of the disks. The authors also observed a plasmonic hot electron doping of the monolayer MoS_2 due to the presence of the tip and the nanodisks on the substrate, which caused a transient structural phase transition from 2H to 1T [85].

TERS has also been used to study highly localized strain in MoS_2/Au heterostructures induced during the formation of such heterostructure, in which the maximum shift reported for the E_{2g} mode was (4.2± 0.8) cm^{-1}, corresponding to 1.4% biaxial strain [77]. TERS have been used to study nanoscale defects and wrinkles on MoS_2 with a spatial resolution of $\sim$ 18 nm, identifying localized inhomogeneities [80] and probing edge-related properties in few-layers MoS_2 [82].

More recently, the local doping variations in the depletion region in in-plane homojunctions in MoS_2 devices have been imaged using tip-enhanced photoluminescence (TEPL) [72]. In TEPL, the local luminescence is measured rather than the phonon scattering, and Gadelha *et al.* used the spatial oscillation of the exciton and trion frequencies to image doping variations with nanometer resolution.

Other 2D materials have also been investigate by TERS, such as the transition metal monochalcogenide (TMM) gallium sulfide (GaS) [86], which is interesting for having two different Raman active A_{1g} modes. The authors reported that the phonon coherence length (L_c) for a five-layers GaS is different for the A^1_{1g} phonon (L_c ~64nm) and for the A^2_{1g} phonon (L_c ~47nm). The L_c were determined through the approach curve experiment, which consists of moving the tip out from the sample at fixed steps and recording the Raman spectrum at each point, as displayed on Figure 2.8 (b) for the A^1_{1g} peak. In order to do so, a curve must be fit to the experiment data that has as one of its parameters L_c, similarly to what was done in graphene [84] and to what will be done in chapters 4 and 5. As L_c becomes larger, so does the TERS enhancement for the totally symmetric A mode. Additionally, they showed that L_c decreases as the number of layers decreases, suggesting that scattering with the surface of the substrate has a major role on the phonon decay process.

Back to TMDs, in monolayer $MoSe_2$, TERS and TEPL have been also studied in references

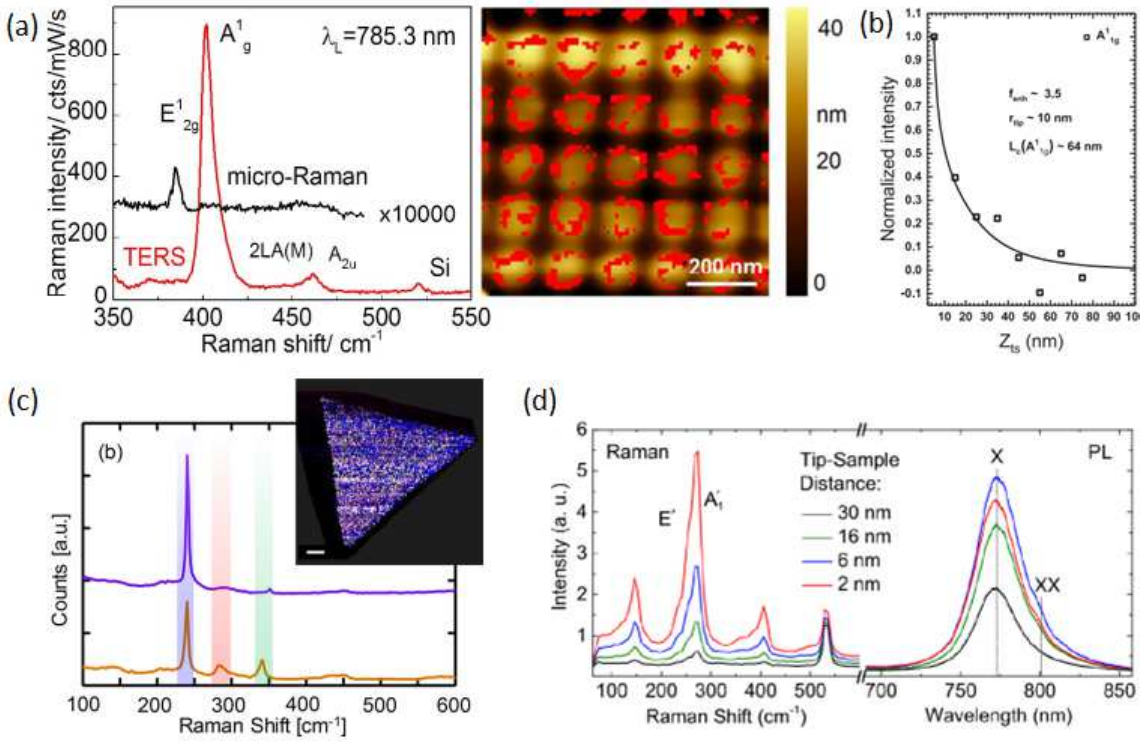

Figure 2.8: Review of TERS and TEPL in different TMDs. (a) Giant gap-plasmon TERS on TMD MoS_2 spectrum (left) on top of a substrate with gold nanodisks (right). The strong signals are recorded at the edges of the nanodisks [78]. (b) Tip-approach measurement that implies the spatial phonon length of TMM GaS [86]. (c) Comparison of non-resonant (top) and resonant (bottom) TERS of TMD $MoSe_2$ and TERS image of the flake [87]. (d) TERS and TEPL spectra of TMD WSe_2 as a function of the tip-sample distance [88]. Reproduced from references [78, 86–88].

[87, 89]. For instance, it has also been used to reveal nanoscale heterogeneities, by combining TERS and TEPL with different scanning probe microscopy techniques [87]. Figure 2.8 (c) shows a non-resonant and a resonant TERS spectra (top and bottom of Figure 2.8 (c), respectively). On the former, only one dominant peak at around 240cm^{-1} (blue) is clearly distinguished, while on the latter there are other Raman peaks at 287cm^{-1} (red) and 340cm^{-1} (green). When comparing these measurements with α-MoO_3 TERS, it was possible to infer that these differences from non-resonant and resonant TERS spectra were due to the inclusion of MoO_3 in the $MoSe_2$ matrix.

In WSe_2, the following references bring studies with TERS and TEPL [88, 90–93]. For example, TERS and TEPL nanospectroscopy and nanoimaging were combined, as shown in Figure 2.8(d). Figure 2.8(d) shows the Raman and PL spectra acquired at different tip-sample distances, showing the E_{2g} (E′) and A_{1g} (A'_{1g}), respectively, at around 273cm^{-1} and the first (150cm^{-1}) and third (405cm^{-1}) order LA phonons [88]. The authors also suggest that the shoulder in the TEPL spectra may be coming from the rise of trion or biexciton emissions. These features allowed the study of monolayer WSe_2 grown by physical vapor deposition of associated nanoscale heterogeneities in the form of edges, grain boundaries and nucleation sites, extracting information about correlations of the photoluminescence spectral intensity,

shifts with crystal edges and exciton diffusion length. The data suggests approximately 25 nm exciton diffusion length, inferred due to the spatial scale of the photoluminescence quenching, and around 30 to 80 nm wide region of optical heterogeneity at the edges. Still on WSe_2, it was also reported that other metals, beside Au and Ag, can be used to prepare a substrate for gap-mode TERS [90], showing similar results for the TERS measurement for WSe_2 on Au and Cr substrates, implying that these results can be extended to other metals.

Finally, in WS_2, TERS and TEPL were also used to study materials properties and defects [94–97]. For instance, in reference [96] the authors performed an ultrastable TERS measurement that lasted 6 hours in total, making it possible to analyze larger flake areas, analyzing defects in micrometer-sized flakes. This experiment overcomes one of the biggest problems in TERS measurements: stability. They achieved that by developing a feedback system that compensate the regular thermal and ambient condition drifts in the system. Furthermore, in reference [95] the authors performed TERS probing defects in monolayer WS_2. They show that the sulfur vacancies produce not only a red shift in the A_{1g} mode, but it also red-shifts the defect related bands. Their advance pave the way to analyze the quality of WS_2 monolayer for applications in optoelectronic devices.

One more scenario that has been growing in interest are the so-called 2D materials heterostructures [5, 98]. They could either be vertical, in which one material is placed on top of the other, or lateral, in which the materials are placed side by side. The interaction in the interface generates different phenomena that are not observed when the materials are isolated. Thus, constructing graphene or TMDs heterostructures is a hot topic for studying with TERS and TEPL. For instance, in reference [99] it was observed by the first time the so-called Morié patterns in a twisted bilayer graphene using an optical technique. It was showed that the different stacking regions (AB and BA, AA and the solitons) present different Raman (TERS) signal. In TMDs heterostructures, a few works are already reported in the literature regarding TERS and TEPL [92, 100–106]. For instance, in reference [101], the authors studied a WSe_2/WS_2 vertical heterostructure and they were able to directly track interlayer (de)coupling in a TMD bilayer. They were also able to study the decouple of the layers due to the absent of the low frequency interlayer phonon. Moreover, in reference [106] the authors probe the interface in a MoS_2-WS_2 lateral heterostructure, in which they suggest that a multi-disordered interface of lateral heterostructure is created by a continuous alloy of TMDs within tens of nanometers.

Chapter 3

Methodology

In this chapter it will be presented the methodologies used in the construction of this thesis, which consists of the details of the sample preparation (in particular, the device production) and the experimental setup for SNOM (TERS and TEPL).

3.1 Sample preparation and field-effect transistor

To perform TERS and TEPL measurements, since the sample has to be illuminated via transmission (see details in section 3.2), the substrate must be transparent. Additionally, as we use a short working distance objective, the cover slip should be thin in thickness (< 0.170 mm) and, being an oil objective, of a reasonable size ($\approx$ 1x1 cm^2 or larger) to prevent oil leakage onto the sample. Therefore, when preparing samples, these considerations should be taken into account.

Samples of two-dimensional materials prepared for direct TERS or TEPL measurements are obtained through standard mechanical exfoliation [107, 108], directly onto the cover slip that will be used for the measurement. However, in some cases, it is of interest to measure a specific flake or to assemble heterostructures, where materials of the same or different nature are stacked. There are various methods to construct these structures [109–112], but traditional transfer methods usually involve placing a layer of hBN on top of the sample. However, for our system, it is necessary for the tip to approach very close to the sample (approximately 5 nm distance), a thick layer of material in the order of tens of nanometers (as is typically the case with hBN flakes used for transfer) makes the experiment unfeasible. Therefore, our own tear-and-stack method had to be developed [74]. This method involves using a pyramidal-shaped Polydimethylsiloxane (PDMS) stamp covered with a layer of polycarbonate, thus creating a pick-up method by stacking a large number of two-dimensional materials in the desired order. Figure 3.1 summarizes the process for creating a TBG that can be extrapolated in order to build a graphene device [23] or to simply produce any sample of interest without a top hBN.

The development of this method produced two papers, both contributing extensively in the sample preparation process, displayed in references [74, 99].

Another crucial aspect of this work involves the preparation of field-effect transistors

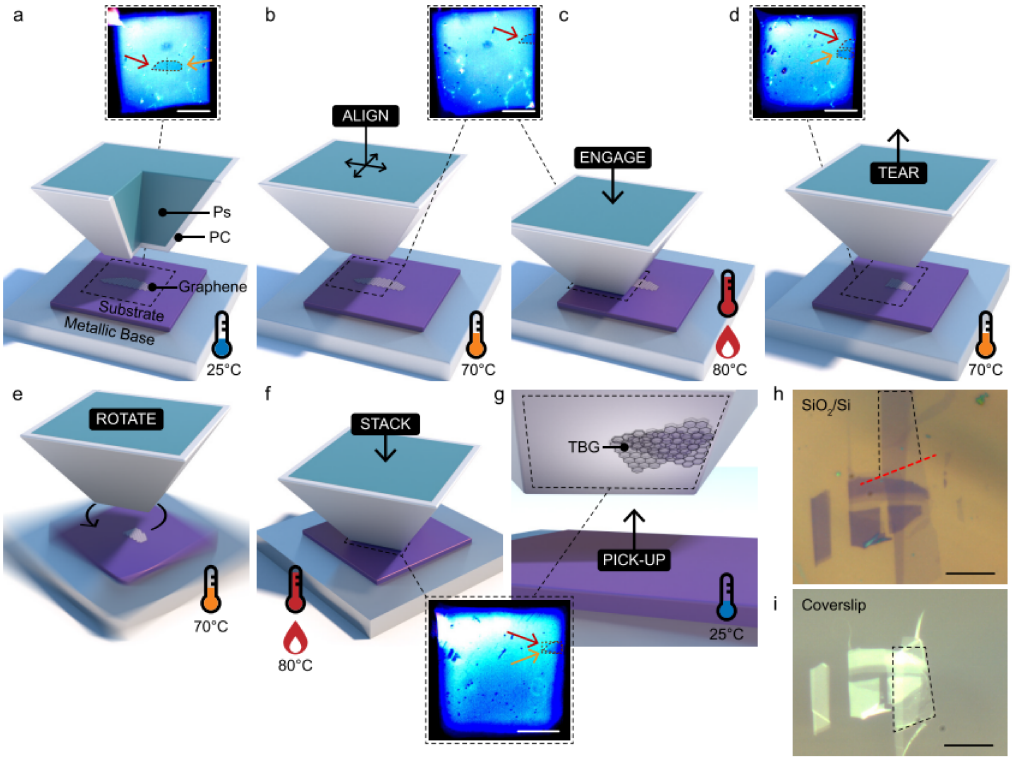

Figure 3.1: Tear and stack to build TBG using the pyramid stamp (PS). (a) Visualizing the graphene flake through the PS. (b) Beginning of the tear process. The PS is aligned over a region of a graphene sheet. (c) PS in contact with part of the graphene sheet while the temperature is raised. (d) PS cooled down and retracted from the graphene sheet, tearing and picking up the section of sheet previously in contact with the PS. (e) PS aligned over the remaining half of the graphene sheet, which is then rotated by the desired twist angle. (f) PS pressed in contact with the rotated section of the graphene sheet while the temperature is raised. (g) Sample cooled down, separating the PS from the sample. The TBG stays attached to the polycarbonate that covers the PS. The scale bar depicted in the optical pictures presented in panels a-g is 50 μm. (h) Optical micrograph of a graphene sample on a SiO_2/Si substrate before the tear and stack process. (i) Same transferred to a coverslip after a tear and stack procedure. The scale bar depicted in panels h and i is 10 μm. Figure taken from [74].

(device) to study the dependence of the Raman / TERS spectrum of graphene by varying the number of charge carriers in the material. The physical device is displayed in Figure 3.2 (a) and it is illustrated in Figure 3.2 (b). In the context of our present study, the material of interest is graphene, with graphite contacts, hBN as the insulator, and the material used for the gate is an object of study in section 4.1.

The graphene device was prepared by patterning the contacts with e-beam lithography on a glass coverslip (we adopt a thin 10 nm Al layer over the e-beam polymer to avoid charge accumulation), followed by a 1 nm/10 nm-thick Cr/Au film evaporation. After that, we used the developed tear and stack method in Figure 3.1 to stack [without the rotation part in Figure 3.1 (e)] the graphite-graphene-hBN heterostructure (where lateral graphite leads are used simply as Ohmic contacts), and then we deposit it on top of the pre-patterned coverslip. Again, the device is purposely not encapsulated so that the tip could interact with the graphene directly.

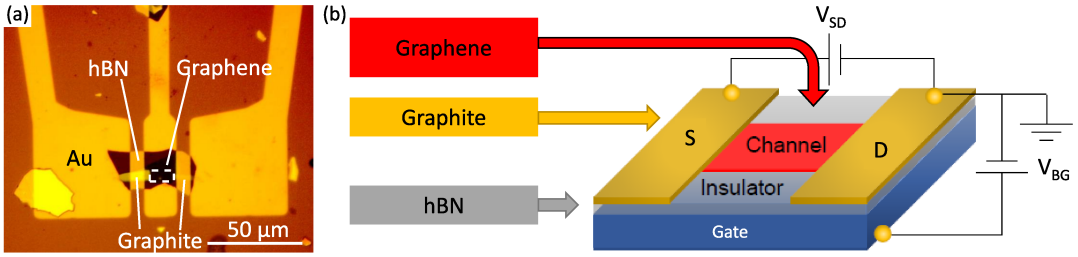

Figure 3.2: (a) Optical image of the real device built for this work and (b) illustration of the device, with our material used for the gate being a metallic material, graphite contacts, hBN as the insulator, and graphene as the channel material.

3.2 TERS and TEPL experimental setup

To perform the measurements, the system used in the laboratory employs a radially polarized beam, which enters the microscope by passing through a dichroic mirror. The laser beam interacts with the sample, and the back-scattered signal has two output channels: it either goes to an optical path ending in an Andor Shamrock SR-303i spectrometer or to a path with a photon counter (avalanche photodiode - APD) from Excelitas model SPCM-AQRH-14, as illustrated in Figure 3.3. The inverted microscope employs a 60x objective (NA 1.4) with oil immersion to focus the beam on the sample and the tip.

The measurement system can also be viewed as a combination of a confocal Raman microscope with a scanning head for AFM on top. The scanhead used in this work was assembled specifically for this project based on previous models [113–115]. It consists of two piezoelectric ceramics (one to control the movement along the z-axis and one to control the movement along the x-y axis) bonded together. These are glued to a Macor ceramic ring with EPO-TEK adhesive, which, in turn, is glued to a metal ring to integrate with the rest of the scanhead body, as shown in Figure 3.4 (a). At the other end of the tube, the first amplification stage is attached [Figure 3.4 (b)], where the tuning fork terminals are soldered to the tip. This assembly is then placed in the scanhead body [Figure 3.4 (c)], where there are two metal boxes on the sides: one is the circuit through which the signal passes for the z-piezo, and the other is only for wire passages to the second amplification stage to the breakout box, and to the controller of the RHK model R9. Details of the electronics can be found in references [113, 115].

The system's AFM operates in shear force (non-contact) mode with a resonance frequency shift at around 32 kHz. On one of the tines of this tuning fork, a Plasmon-Tunable Tip Pyramid (PTTP) [53, 56] is attached. The nano pyramid of this tip has a side legth (L) that is adjustable for achieving plasmonic resonance with the laser used, as shown in Figure 3.5 (a). The ideal L for the HeNe laser, which is used for the measurements, $\lambda = 632.8$ nm, is around 470 nm. Previously, the PTTP was first glued to a tungsten wire and then it was glued to the tuning fork [as displayed in Figure 3.5 (b)], whereas now the PTTPs are attached direclty to the tuning fork [Figure 3.5 (c)].

Before, the tuning fork was soldered direclty in the first amplification stage, causing it

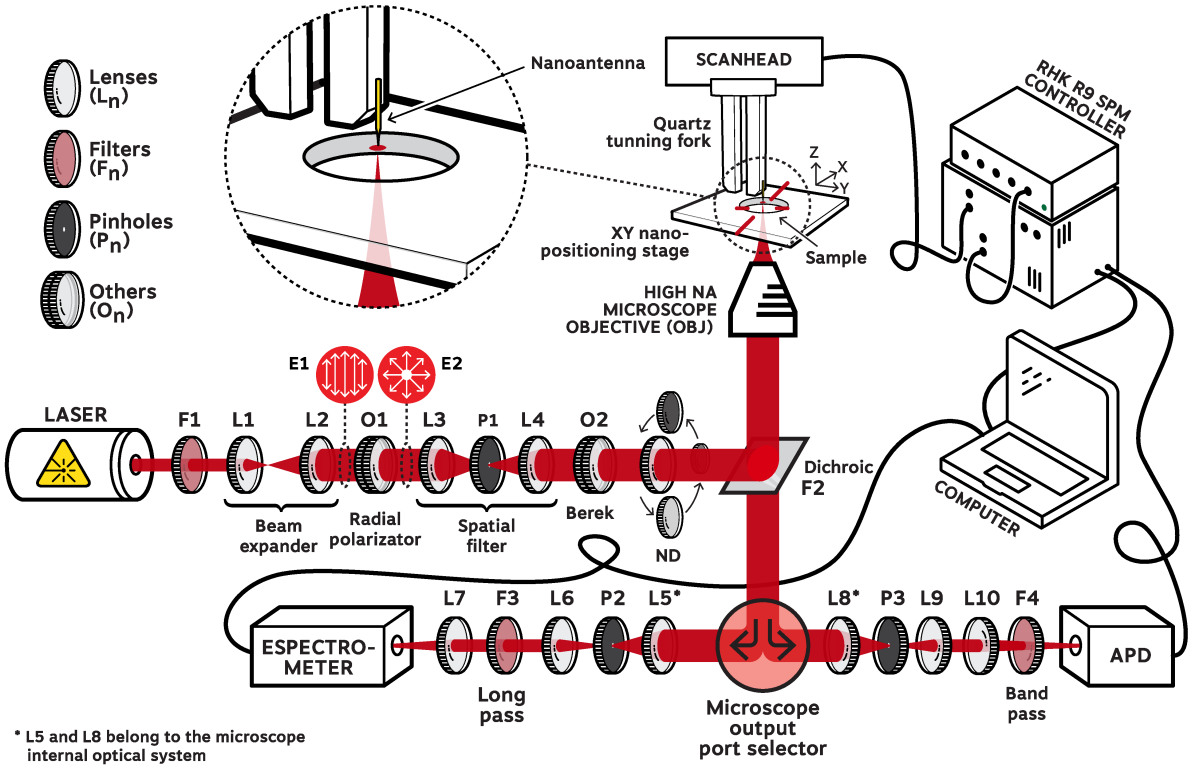

Figure 3.3: Experimental schematic of the TERS and TEPL system, taken from reference [113]. The laser beam enters the microscope passing through a dichroic mirror, interacts with the sample and the tip, and returns to one of the optical paths with either the spectrometer or the APD. The entire system is controlled by the RHK company's R9 software for the scanning microscopy part and by Andor SOLIS version 4.31.30023.0 software for the spectral part.

to overheat often, damaging the circuit (circuit exchanges were done usually after 4 to 5 tip exchanges) and hazarding the piezo. Moreover, also due to the heat applied in the soldering process, one had to wait for a few hours to start the experiment after the tip was positioned for the system to reach thermal equillibrium. Now, the soldering of the tuning fork is done in a tip-exchange mechanism [see Figure 3.5 (d)] that can be disconnected from the circuit. In this way, it was not needed to exchange a first amplification stage for more than two years over hundreds of measurements. Furthermore, since the tip's assembly is done prior to the experiment, one can perform dozens of experiments in one day (the tips are already at thermal equillibrium and ready to use).

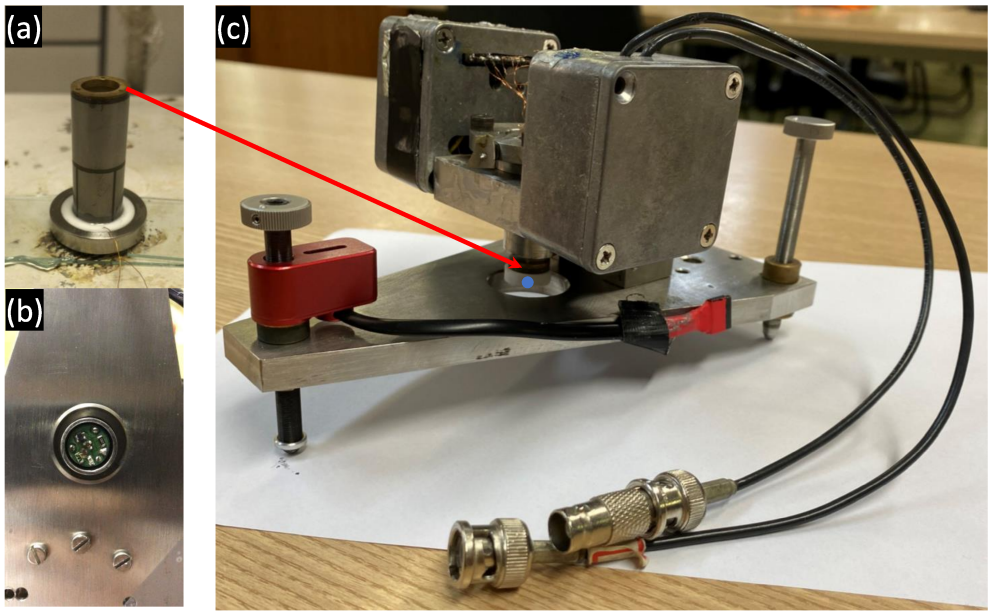

Figure 3.4: (a) Piezoelectric ceramics z and x-y. At the bottom, the piezoelectric ceramic is glued to a ring made of Macor ceramic, which itself is glued to a metal ring. (b) Bottom view of the already assembled scanhead, with the first amplification stage and the electronic components already soldered. (c) Completely assembled scanhead ready to use. The metal ring in part (a) is upside down at the edge of the red arrow. The blue dot is the tip-exchange socket that eases the tip exchange process [see Figure 3.5 (d)]. Circuit details can be found in [113–115]

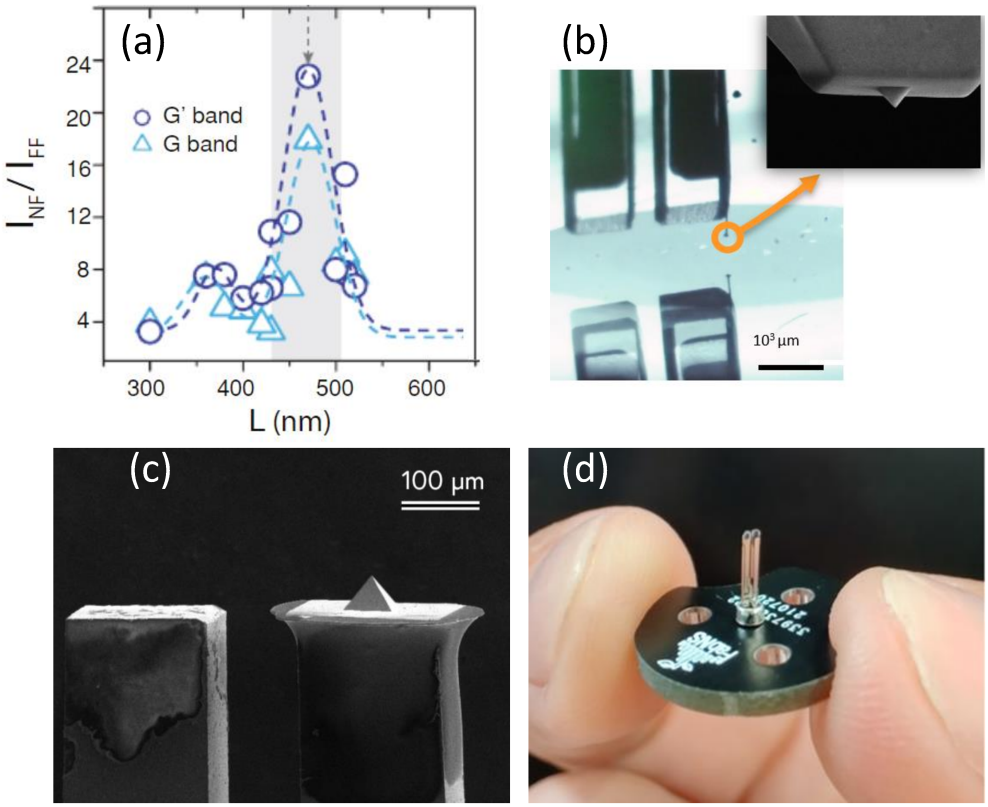

Figure 3.5: (a) Graph of the near-field (NF) to far-field (FF) Raman intensity ratio, I_{NF}/I_{FF}, as a function of the edge size L of the nano-pyramid, for a laser with a wavelength $\lambda = 632.8$ nm. The edge size L at which the tip plasmon resonates with the HeNe Laser wavelength is around $L = 470$ nm. (b) Optical image of the tuning fork with the PTTP at the tip attached by a Tungsten wire, and a scanning electron microscopy (SEM) image showing the nano-pyramid. (c) SEM image with lower magnification showing the way that the tips are currently being coupled to the tuning fork. (d) Tip-exchange mechanism to easily exchange tips from the scanhead. Panels (a) and (b) were adapted from [53] and panels (c) and (d) are taken from reference [116].

Chapter 4

Graphene Device

This chapter comprehends micro-Raman and TERS measurements of a graphene device, in which it is possible to vary the graphene's Fermi level and to record the Raman spectra with and without the tip. In the first part it will be discussed the gate metal choice, which is important due to the specificity of our experimental setup and due to graphene's photo-doping. Then, we carried out the Raman and TERS measurements for different values of electronic doping. Here, due to our careful choice of materials for the device, we were able to observe the Kohn anomaly effect at room temperature for the first time in graphene [117]. Finally, we performed the approach curve experiments for nearly neutral and doped graphene. The results show that the Raman coherence lenght depends on graphene's Fermi level. It will aslo be discussed the origin of this so-called Raman coherence length, whether it is preeminent from an electronic or phononic coherence length [23].

4.1 Gate metal choice

In our TERS and TEPL system, the illumination is done from below; therefore, the material used for the gate must be thin enough for the laser to reach the material with a reasonable power for the study. Additionally, the gate must not exhibit optical activity in the Raman bands region of the studied material, otherwise it could mask the signal of interest. Lastly, as the aim is to study the Raman properties of two-dimensional materials as a function of their doping, the material used for the gate must not induce extra variations in doping caused by the laser (photo-doping) [118].

Four materials were tested as the gate of a graphene device: WS_2, MoS_2, WTe_2 and Au, as shown in Figure 4.1. The first three were transferred onto the substrate as explained in section 3.1. As for gold, it was deposited via thermal evaporation, forming a thin layer of 10nm, allowing the passage of the laser with an approximately 50% intensity loss.

For all these materials, the first prerequisite is met: the laser can pass through the material and reach the graphene with a reasonable power. However, upon measuring the Raman spectrum, WS_2 [Figure 4.2 (a)] exhibits optical activity in the region of the graphene's G-band, making it an unsuitable candidate for the intended application. In Figures 4.2 (b), (c),

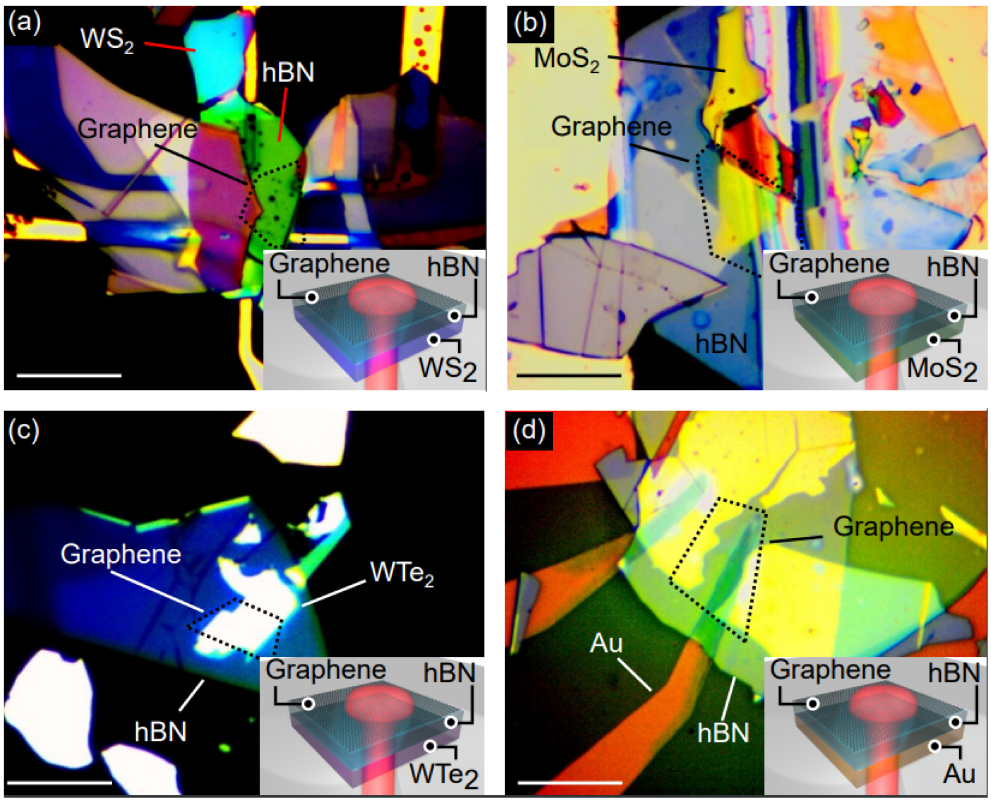

Figure 4.1: Samples of graphene on top of hBN and on top of the gate metal (a) WS_2, (b) MoS_2, (c) WTe_2 and (d) Au. In the insets there is a schematic of the side view of each case.

and (d), it is possible to observe that the G and 2D bands of graphene are clearly detected for MoS_2, WTe_2, and Au gates.

The final excluding condition for the use of materials as a gate is photo-doping. To prevent it, it is necessary for the energy of the laser (E_L) used to be lower than the work function of the metal (Φ_M) minus the electron affinity of the insulator (χ_{IN}) [118], that is:

$$E_L < \Phi_M - \chi_{\mathrm{IN}}. \tag{4.1}$$

The laser used for the measurements is a HeNe laser (632.8 nm, or $E_L = 1.96$ eV) and the insulator is hBN, $\chi_{IN} \approx 2.2$ eV [120]. Therefore, according to equation 4.1, the work function of the material used for the gate should be $\Phi_M > 4.16$ eV. For MoS_2, the work function is approximately 4.9 eV, and for WTe_2 it is approximately 4.10 eV [121]. As for gold, the work function is approximately 5.3 eV [122]. Thus, despite the G and 2D bands being clearly visible in Figure 4.2 c, since WTe_2 is at the limit imposed by Equation 4.1, it can be discarded as a material for the gate of the device. Both MoS_2 and gold meet the three necessary conditions; therefore, they are good candidates for use as the gate. In this study, the choice was made to work with gold instead of MoS_2 as the gate for two reasons: first, due to the relative intensity concerning the baseline; that is, the Raman peaks of interest, although visible, are more affected by the luminescence of MoS_2 compared to gold. Second, for practicality reasons, gold evaporation needs to be carried out for electric contacts in all devices regardless. Therefore, using MoS_2 would add an extra step in the preparation.

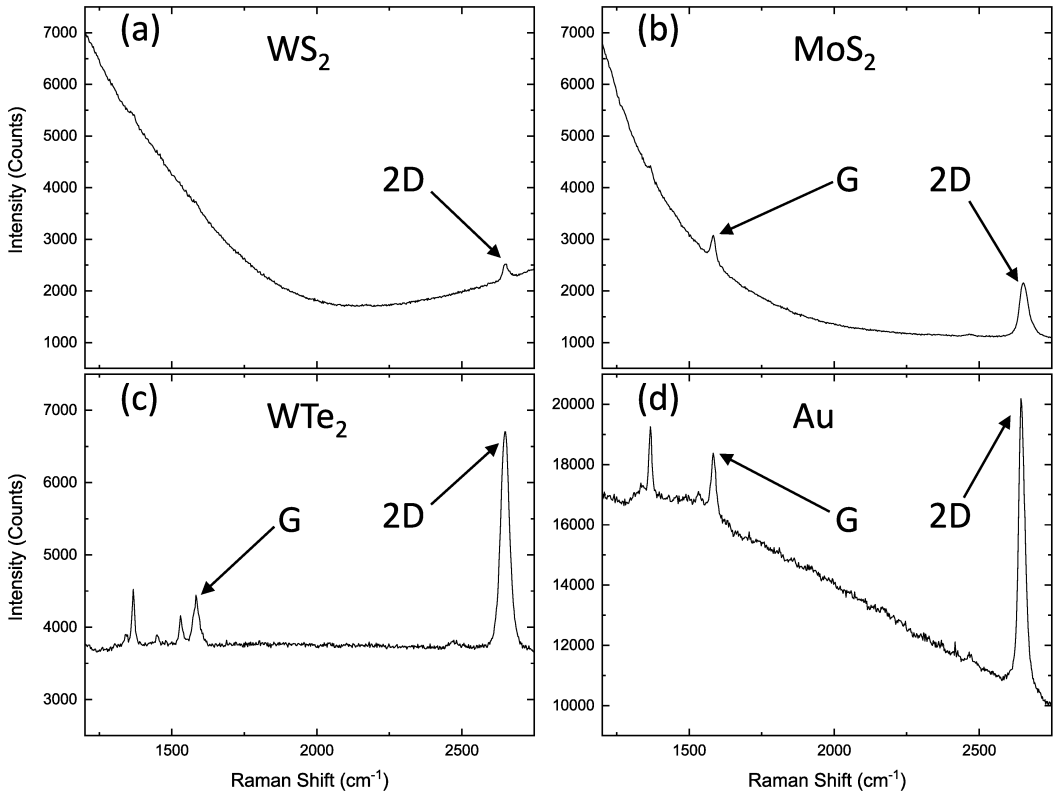

Figure 4.2: Raman spectra of graphene samples on top of hBN and (a) WS_2, (b) MoS_2, (c) WTe_2, and (d) Au. The spectra were measured using a HeNe laser (632.8 nm), 750 μW, with 3 acquisitions of 10 s each. The G and 2D bands of graphene are highlighted where they were observed. The other peaks are either from hBN ($\approx 1366\,\mathrm{cm}^{-1}$ [119]) or from contamination.

Finally, to confirm that the device with gold does not exhibit photo-doping, resistance measurements of the device were conducted as a function of gate voltage, as shown in Figure 4.3 (a). The resistance measurement was taken both before the device was exposed to the laser and after this exposure. It can be observed that the neutrality point occurs at an applied voltage of ≈ 0.2 V before laser exposure and it remains unchanged after exposure to the laser. If gold was inducing photo-doping in the graphene, the neutrality point, indicated by the position of the resistance peak, would altered, which is not observed.

Even though the measurement displayed in Figure 4.3 (a) is already a strong evidence that photo-doping is not happening, this device is not encapsulated, being the reason for the difference in the peak value. Thus, another device was built, but encapsulated this time (not for TERS measurements, but for conventional Raman only). The electrical measurements of this new device were done after exposing the sample to the laser for 120 s with fixed gate voltages (0 to -5 V). After laser exposure, a resistance measurement is performed and, as expected, the curves did not change significantly, confirming that no photo-doping happens using this gate metal choice.

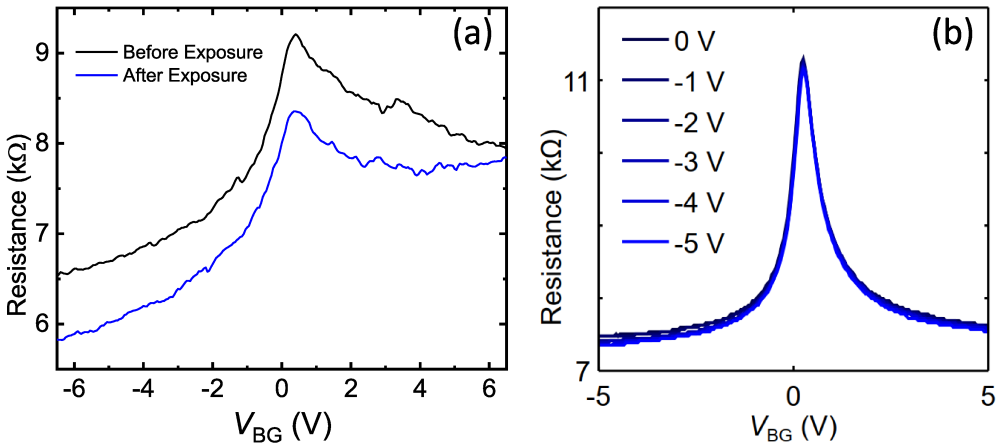

Figure 4.3: (a) Resistance measurement of the device as a function of the applied Gate voltage before and after exposure to the HeNe laser for 120 seconds. The neutrality point is around 0.2V and remains unchanged, indicating that there is no photo-doping in graphene. The difference in resistance values between the two curves is due to the device not being encapsulated, which can lead to gas adsorption on the surface. (b) Resistance measurements made in a similar, but encapsulated, graphene device, showing even further that there is no photo-doping when using Au as gate metal. The measurements were done after exposing the sample to the laser for 120 s for several gate voltages (0 to -5 V). All the electrical measurements from (a) and (b) were performed by a Lock-In Amplifier SR830 DSP.

4.2 Influence of electric field on graphene's TERS spectra

As discussed in section 2.1.1.1, the Raman spectrum of graphene is dependent on the Fermi level. Then, Raman (TERS) measurements were performed on the device to analyze the relative enhancements of the G and 2D bands while varying the gate voltage.

Firstly, a "sweep" measurement (Raman signal acquired varying the gate voltage from -7 V to +7 V with 0.4 V steps) was conducted without the presence of the tip to quantify the variation in the Raman signal of the device compared to those reported in the literature. These results are presented in Figure 4.4, where data from the G and 2D bands of graphene were extracted, such as the peak positions [Figure 4.4 (a) and (d)], intensities [Figure 4.4 (b) and (e)], and FWHM [Figure 4.4 (c) and (f)]. These data are consistent with previously obtained in the literature [36, 40]. Particularly, by observing Figure 4.4 (a), it is possible to identify the "w"-shaped feature in the G-band frequency ramp, which occurs due to the Kohn anomaly [37], not visible in the measurements reported in the literature at room temperature. The reason the Kohn anomaly is clearly seen in the measurements displayed in Figure 4.4 is because of the careful choice for the materials in the device, being the reason why it was reported in one of the papers produced from this thesis [117].

Then, the same sweep was conducted, but this time with the TERS tip. An area of interest is the behavior occurring in the near field when varying the Fermi level of graphene. The same graphs from Figure 4.4 were compiled, and they are presented in Figure 4.5. The fewer number of points on the p-doping side is due to damages to the tip. The conversion from gate voltage (V_{BG}) to number of charge carriers (n) was done using the equation [117]:

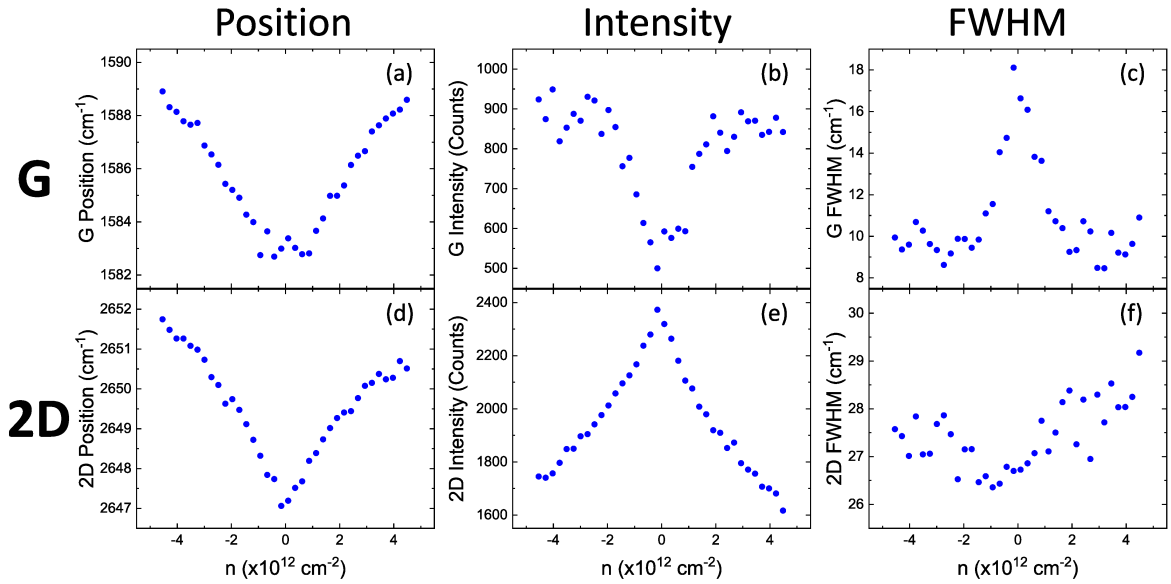

Figure 4.4: Analysis of micro-Raman spectra from a monolayer graphene device varying the number of charge carriers, displaying from the G band: (a) peak position, (b) intensity, and (c) full width at half maximum. Similarly, for the 2D band: (d), (e), and (f), respectively.

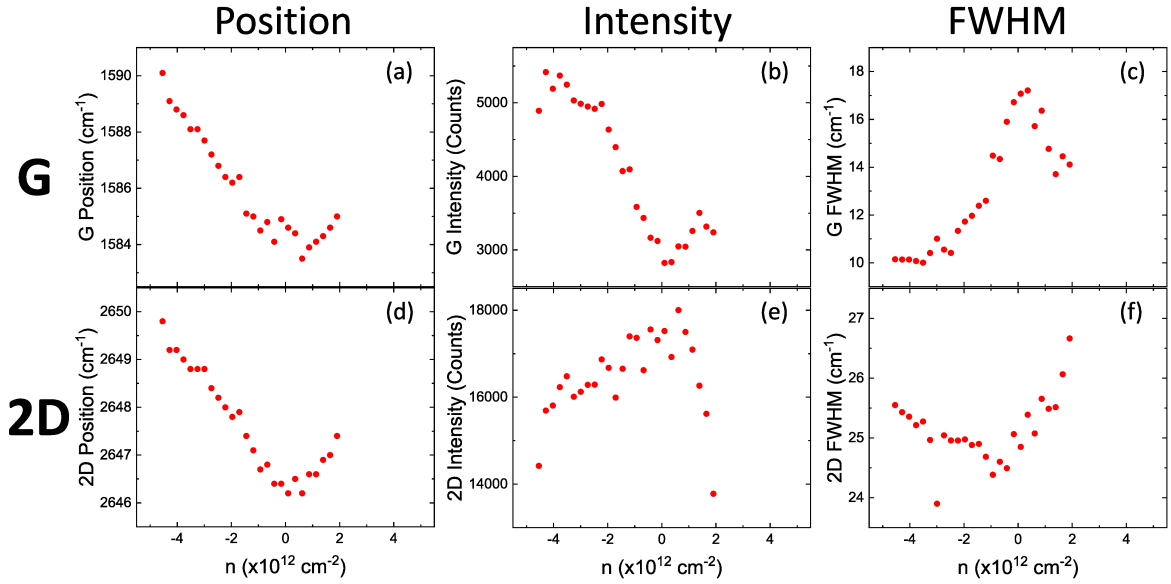

Figure 4.5: Analysis of TERS spectra from a monolayer graphene device varying the number of charge carriers, displaying from the G band: (a) peak position, (b) intensity, and (c) full width at half maximum. Similarly, for the 2D band: (d), (e), and (f), respectively. The fewer number of points on the p-doping side is due to damages to the tip.

$$n = \frac{\epsilon_0 \epsilon_{hBN}}{ed}(V_G - V_{CNP}), \tag{4.2}$$

where ϵ_0 and $\epsilon_{hBN} = 3.5$ are the vacuum permittivity and hBN dielectric constant [123], e is the electron charge, $d = 30\,\text{nm}$ is the hBN thickness and $V_{CNP} = 0.2\,\text{V}$ is the potential at graphene's charge neutrality point.

With these data in hand, in particular the intensities variations of the bands [Figures 4.4

and 4.5 (b) and (e)], it is possible to calculate the Enhancement Factor (EF) by taking the ratio of the intensity with the tip engaged (I^{TERS}) to the intensity without the tip (I^{FF}) for both the G and 2D bands, as shown in:

$$EF_\gamma = I_\gamma^{TERS}/I_\gamma^{FF}, \tag{4.3}$$

in which γ is the Raman mode (G or 2D) and the superscript FF stands for far field (conventional Raman). The G and 2D EF are displayed in Figure 4.6 (a) and (b). With the EF, it is possible to establish the relative enhancement, ρ_0:

$$\rho_0 = EF_{2D}/EF_G. \tag{4.4}$$

Figure 4.6 (c) plots ρ_0 as a function of n. Clearly, ρ_0 has its lowest point near the neutrality point of graphene and increases as the doping level increases. This can be understood as a consequence of the Kohn anomaly effect in the Raman coherence length (L_c), a subject that will be discussed in depth in the next section.

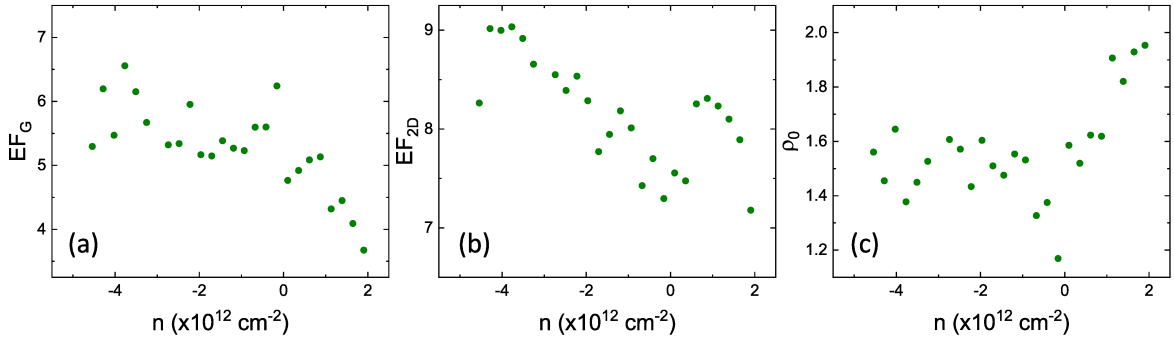

Figure 4.6: EF as a function of the number of carriers for the (a) G band and (b) 2D band. By taking the ratio of these enhancement factors, we have the (c) relative enhancement ρ_0.

One might wonder at this point if the effects observed here are in fact a phenomenon intrinsically from graphene or an external effect due to the variations of the electric field near the tip. To address that, simulations were performed, as reported in reference [124], and what was found is that the changes in electric field due to the gate voltage sweep are negligible.

These data could only be acquired once for this device due to the experimental instability. However, for other devices with different tips the same sweep experiment was performed and the data present a similar trend. The data can be found in Appendix A in Figures A.1 and A.2.

4.3 Coherence length dependence on doping

In this section it will be discussed the relation between the Raman coherence length (L_c) and the Fermi level of graphene. The results obtained are published in reference [23].

L_c is defined by how far a wave keeps its phase [125]. In materials, it depends on the electronic and vibrational structure, representing an important aspect of transport in solid state physics, specially in mesoscopic systems [126]. For example, in the case of graphene,

a zero gap semiconductor, electron-phonon interaction promotes electronic excitation near the Dirac point, resulting in a loss of the optical phonon phase. This is called the Kohn Anomaly effect [35, 39]. By changing the Fermi level away from the neutrality (Dirac) point, the electronic excitation driven by phonon is suppressed [36, 127], causing an increase of the phonon lifetime, which should consistently generate a variation in L_c.

Broadly utilized to study electrons, phonons and electron-phonon interactions is conventional Raman spectroscopy, the inelastic scattering of light [128]. Nevertheless, if the relevant L_c is significantly smaller than the wavelength of light, it cannot be measured by Raman spectroscopy because most of the phonons or electrons participating in the Raman process do not interact with each other. Thus, even micro-Raman spectroscopy is a spatially incoherent phenomenon. However, in nano-Raman spectroscopy, the spatial resolution can be comparable or smaller than L_c, and the fields can interfere.

The most prominent technique for implementing nano-Raman scattering is TERS [129, 130], and a theoretical framework to access L_c in two-dimensional systems was introduced in references [20, 22], based on the dependence of the TERS intensity on the tip-sample distance and on phonon symmetry. The drawback is that, while the theory can be used to obtain L_c, one needs another way to confirm whether the theory is reliable. In this sense, the tunable Kohn anomaly offers a parameter to play and check the validity of the theory for coherent near-field Raman scattering [20, 22]. In this section, we have evaluated the gate voltage dependence of L_c in a graphene device by performing TERS measurements while varying the Fermi level, i.e. while tuning the Kohn anomaly strength, showing consistency with the TERS-coherence theory. The novel results show a renormalization of the optical phonon energies different from what has been measured before [36, 127], due to the ability of nano-Raman spectroscopy to extract information very close to the Γ point, strongly empowering the technique.

Figure 4.7 (a) shows a schematic of the setup used in this work, which consists of the device presented in section 3.1 and the TERS tip interacting with the laser and the sample [53, 131]. Once the tip was engaged (~ 5 nm distant from the sample), a TERS spectrum was measured, and then the tip was pull 0.5 nm up to measure the spectrum again. The process was repeated until the tip was 55 nm away from the sample. Figure 4.7 (b) plots the TERS signal showing the G ($\sim 1584\,\mathrm{cm}^{-1}$) and 2D ($\sim 2650\,\mathrm{cm}^{-1}$) bands, and how they decrease when retracting the tip away from the sample, for tip-sample distances varying from z =5 nm to 50 nm.

After performing the TERS experiments for several gate voltages in section 4.2, the approach curve experiment was done. Figures 4.8 (a) and (b) plot the peak intensities of G and 2D bands as a function of z for graphene slightly doped [(a), density of charge carriers $n = 0.4 \times 10^{12}$ cm^{-2}, with $n = 0$ at the neutrality point] and highly doped [(b), $n = 4.5 \times 10^{12}$ cm^{-2}]. The intensities are independently normalized by the respective FF values (with the tip far from the sample), to clearly show that the 2D band (A_{1g}, totally symmetric) enhances more than the G band (E_{2g}, non-symmetric mode) when approaching the tip, due to differences in the near-field spatial interference conditions [20].

L_c can be determined by fitting the z-dependent TERS intensities with the theory of spatially coherent near-field Raman scattering [22]. Using the Mathematica package, L_c is

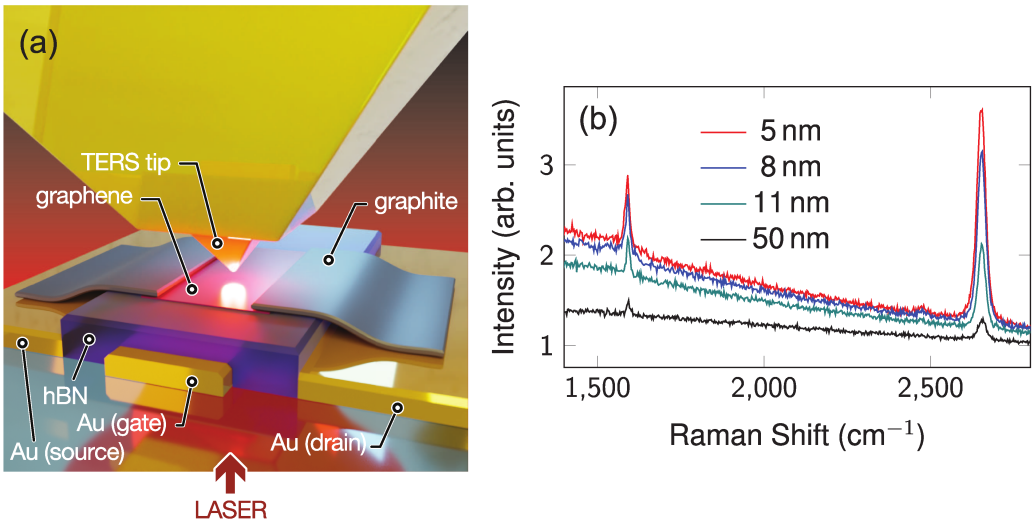

Figure 4.7: (a) Device configuration: a HeNe laser focusing from the bottom passes through the glass coverslip, a thin Au layer, an hBN flake and a monolayer graphene, and interacts with the TERS tip. (b) Graphene Raman spectra for tip-sample distances of $z = 5$ nm (red), 8 nm (blue), 11 nm (teal) and 50 nm (black).

found using the TERS intensities formula 2.21. By fitting a curve to the experimental ratio $\rho(z)$, as shown in Figures 4.8(c) and 4.8 (d) for the graphene slightly and highly doped, respectively, the L_c, r_{tip} and f_e are numerically found. The measurements are performed using the same tip, so that r_{tip} and f_e are expected to be the same, and fitting the curves provides $r_{tip} = 7.5$ nm and $f_e = 4$, which are reasonable values based on previous experimental results [21, 22, 56, 86].

Since the intensity depends also on the mode symmetry, fitting the ratio between the A_{1g} and the E_{2g} modes provides an internally consistent metric. For this reason, Figures 4.8 (c) and 4.8 (d) plot the relative enhancement (ρ) of 2D to G band intensity (black bullets), normalized by the far-field Raman intensity as a function of z, defined by

$$\rho(z) = (I_{2D}^{TERS}(z)/I_{2D}^{FF})/(I_{G}^{TERS}(z)/I_{G}^{FF}). \tag{4.5}$$

Note that this equation is a generalization of equation 4.4, but this time it is z-dependent. Here, while the superscript FF stands for far-field, indicating the result obtained with the tip far ($z = 55$ nm), the superscript $TERS$ stands for near-field at a tip-sample distance of z. As shown in both Figures 4.8 (c) and (d), ρ monotonically decreases to the unity with increasing z up to sufficiently large values, and the data are fitted (red solid lines) to find the coherence lengths. For the highly doped case [Figure 4.8 (d)], $L_c = (37 \pm 2)$ nm is found, in good agreement with the previous literature data (~ 40 nm) [22]. For the slightly doped case [Figure 4.8 (c)], we get a shorter coherence length $L_c = (27 \pm 2)$ nm. The different L_c values is due to the change in the Fermi energy, i.e. due to changes in the Kohn anomaly strength, which seems to consistently affect L_c.

To investigate the L_c dependency on Fermi energy, we use the experiment discussed in section 4.2, in which a sweep is performed with and without the tip, recording the Raman

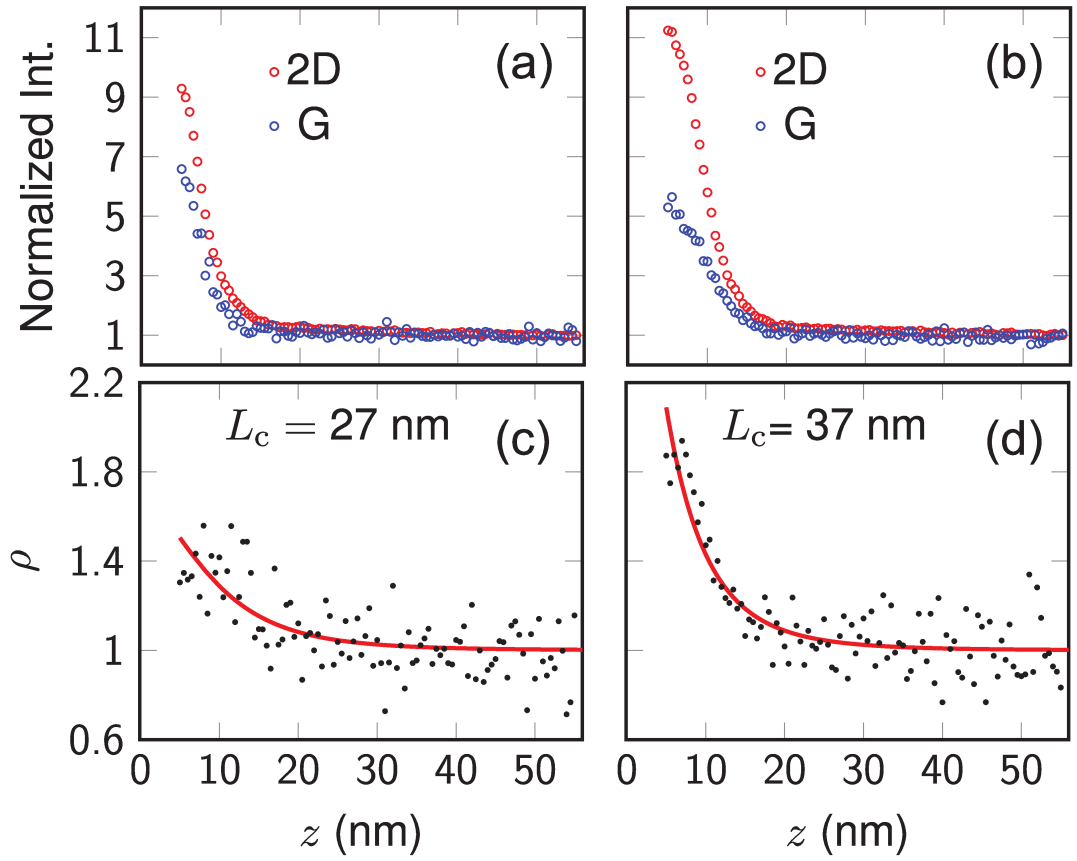

Figure 4.8: (a) 2D and G Raman band intensities separately normalized in the FF, as a function of tip-sample distance (z) for a slightly doped graphene, $n = 0.4 \times 10^{12}$ cm^{-2}. (b) Same as (a) for a highly doped graphene, $n = 4.5 \times 10^{12}$ cm^{-2}. (c),(d) Approach curve data (black bullets) for the normalized relative enhancement ρ (see equation (4.5)) for graphene (c) slightly doped and (d) highly doped, and curve fit (red lines) according to [22]. $L_c = (27 \pm 2)$ nm and $L_c = (37 \pm 2)$ nm are found for the slightly and highly doped cases, respectively.

(TERS) spectra for several gate voltages. We define the value of ρ at the position of tip engaged ($z = 5$ nm), which is denoted by ρ_0, as a metric related to the maxima TERS enhancement. A theoretical relation between ρ_0 and L_c can be found using Green's function calculations [22] [see blue bullets in Figure 4.9 (a)] and, considering that the interference effects generating distinct levels of TERS enhancement scale with the area defined by the coherence length, it can be represented by a quadratic dependence [see blue line in Figure 4.9 (a)]

$$\rho_0(L_c) = 1 + CL_c^2. \tag{4.6}$$

Using equation 4.6, the measured values of ρ_0 can be converted to L_c^2, and Figure 4.9 (b) plots L_c versus the density of charge carriers (n), consistently showing a minimum towards the neutrality point, as expected due to the modulation of the Kohn anomaly strength. The zoom in the x-axis (not displaying higher n-doped points) is just for symmetry of the graph.

Theoretically, the L_c dependence on n is expected to follow the power law

$$L_c(n) = A + Bn^{1/4}, \tag{4.7}$$

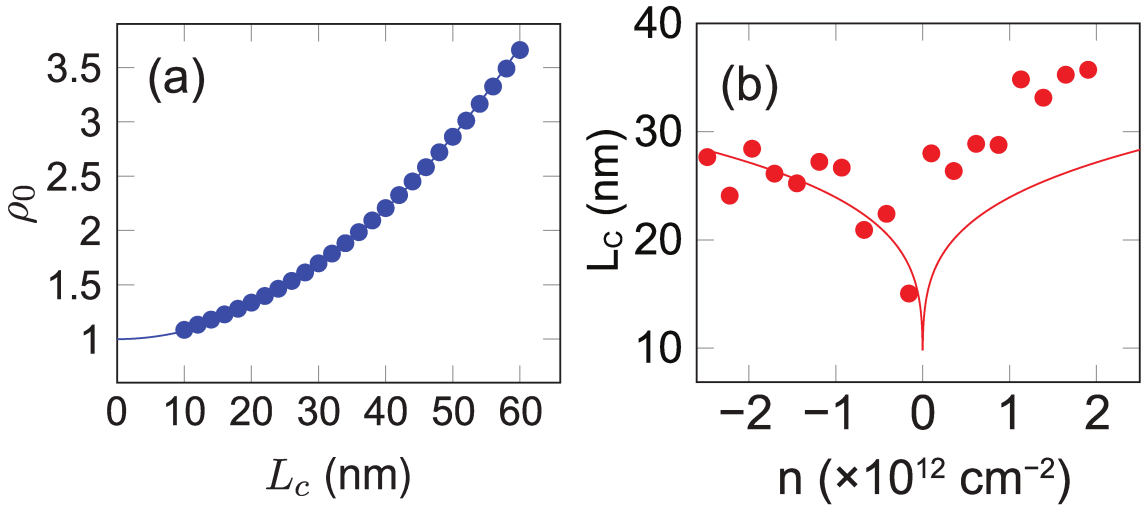

Figure 4.9: (a) Theoretical dependence of the relative enhancement ρ_0 on L_c calculated based on the theory for spatially coherent TERS (blue bullets) and a fit to the theoretical points using equation (4.6); $C = (747 \pm 2) \times 10^{-6}\,\mathrm{nm}^{-2}$ if found. The ρ_0 behavior depends on sample properties (L_c and phonon symmetry) and on TERS tip properties (tip radius $r_{tip} = 7.5\,\mathrm{nm}$ and field enhancement factor $f_e = 4$). (b) L_c as a function of n. Dots are the experimental data converted using equation (4.6), and the red line is the data fit using equation (4.7); $A = (7 \pm 4)\,\mathrm{nm}$, representing the minimum value obtained for $L_c(n)$, and $B = (17 \pm 4)\,(10^7\mathrm{nm}^3)^{1/2}$ as a proportionality constant. The fitting procedure considered only n negative, and the p/n asymmetry is expected to be related to instrumental artifacts (contacts influence and loss of TERS enhancement).

where the L_c scaling with $n^{1/4}$ comes from the Landauer formalism [132] for ballistic transport in graphene: conductivity scaling with the number of conducting channels ($\sigma \propto \sqrt{n}$) [133] and with scattering coherence area ($\sigma \propto L_c^2$). Notice that, while in TERS the light interacts with high-energy photo-induced electrons, the Landauer formalism is used to describe the L_c variations because the Kohn anomaly happens due to electron-phonon interactions at low energies. The fitting curve is shown by the red line in Figure 4.9 (b).

4.3.1 Phononic or electronic origin of the coherence length dependence on doping

The previous section discusses the coherence length in a nano-Raman (TERS) experiment. The origin of this coherence length can be related either to electrons or phonons since the Raman process involves both quasiparticles. In this sub-section it will be presented a discussion regarding these possible assignments.

First, let's consider the phononic case. The theory discussing the use of coherent TERS to measure L_c was introduced in reference [20] and further extended in reference [22]. This theory, which is behind equation (2.21), is based on Green's functions and it can be used to measure the correlation length of the source of the scattered electromagnetic fields. The polarization of the scattered field is dictated by the Raman tensor, thus describing how the G (E_{2g}) and 2D (A_{1g}) phonons exhibit different TERS enhancements. The fact that the different

enhancements, as evidenced in Figure 4.8, are related to different phonon symmetries, suggest the identification of L_c as the phonon coherence length [20–22, 86].

Figure 4.10 displays a schematic of the interference process, taken from reference [20], in which the green arrows in Figure 4.10 (a) represent the radially polarized light irradiated by the tip (yellow circle) onto a graphene sheet. Within this theory, inside the phonon coherence length the vibrations have a fixed phase and the fields coming from different locations of the sample, back to the tip, can interfere constructively or destructively. More specifically, in Figure 4.10 (b) the scattered light, represented by the red arrows, is scattered by a totally symmetric (2D) phonon, keeping the same orientation as the incoming light and interfering constructively when back to the TERS tip; however, if the phonon is not totally symmetric, the scattered light polarizations are changed locally, losing the fully symmetric radial configuration. Figure 4.10 (c) and (d) show how the E_{2g} mode (G phonon) rotates the light polarization (red arrows). In this non-symmetric scenario, destructive field interference happens in the TERS tip. This, as demonstrated in [20], results in different enhancements of the bands in near-field Raman, and the experimentally measured difference provides the radius from where the fields exhibit coherence, interpreted as the phonon coherence length.

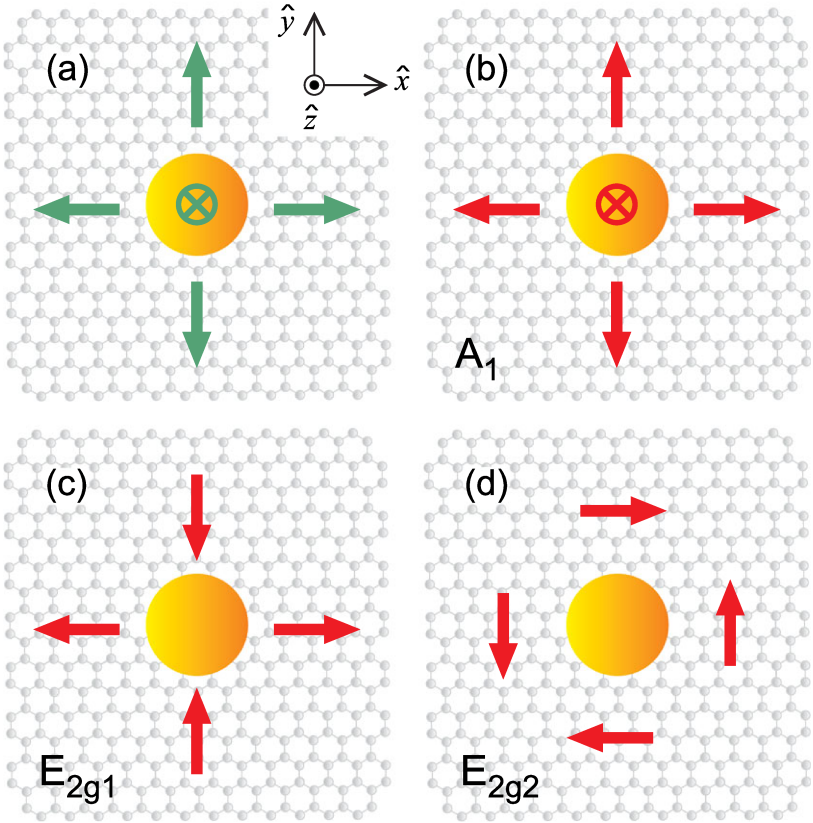

Figure 4.10: Schematics of the TERS interference for different Raman modes. (a) The green arrows represent the radially polarized light irradiated by the tip (yellow circle) into a graphene sheet. (b) The red arrows represent the scattered light from a totally symmetric (A, or 2D) mode, while (c) and (d) represent the scattered light from a non-totally symmetric (E_{2g}, or G) mode. Figure taken from [20].

Furthermore, the values obtained in these works for the coherence length ($L_c \approx 30-40$ nm) are consistent with measurements on graphite of different crystallite sizes (L_a) [134]. In reference [134], they show the width of the G band (Γ_G^A) as a function L_a. When decreasing L_a, the values of Γ_G^A do not change until when the crystallite sizes get smaller than 30-40 nm, then the G band width starts increasing significantly, a result that can be understood considering that the G band phonon coherence length is, indeed, around 30-40 nm.

Based on the assignment of L_c variation due to phonons, a method to determine the variations on the G-band phonon group velocity $v_g = \partial\omega/\partial k$ using the special setup from this work can be proposed

$$v_g = \frac{L_c}{\tau_{ph}}, \tag{4.8}$$

in which τ_{ph} is the phonon lifetime, and it can be obtained from the linewidth of the G phonon data using the uncertainty relation $\tau_{ph}\Delta E \sim \hbar$. The important aspect here is that, when the Fermi energy of graphene is located at the Dirac point, since an electron-hole pair can be excited by absorbing a phonon, the phonon frequencies of the G and 2D bands become soft due to the Kohn anomaly effect [39]. The Kohn anomaly effect for these bands occurs, respectively, for the longitudinal (LO) and in-plane transversal optical (iTO) phonon modes at the center (Γ point, G) or corner (K point, 2D) of the Brillouin zone. As a result, these phonon dispersions become singular like a kink at the Γ or K points [36, 37, 40].

Consider the energy uncertainty $\Delta E^{G_{FWHM}} = \Delta E^{G_{KA}} + \Delta E^{G_0}$, where $\Delta E^{G_{KA}}$ is the G-band energy uncertainty due to the Kohn anomaly effect and ΔE^{G_0} is the G-band energy uncertainty due to all other effects. Using equations 4.6, 4.7, 4.8 and the G-band FWHM variation [ΔG FWHM, see Figure 4.11(a)], we can calculate Δv_g as a function of n for both experimental data and theoretical modeling [see Figure 4.11 (b)]. It is noticeable that, near the neutrality point, the group velocity is at it's maximum (around 40 km/s). These values are unusually high, 20 times larger than v_g for optical phonons in graphite and twice the value for the longitudinal acoustic phonon [135], indicating that the Kohn anomaly near the Γ point strongly distorts the phonon dispersion diagram. The "M" shape in theory (line) near the neutrality point is consistent with the "W" shape predicted and observed for the phonon frequency [36, 127]. What is troublesome with this development is that the present theoretical work on the phonon dispersion relation of graphite and graphene do not predict this ultra-strong phonon softening very close to the Γ point in the Brillowin zone [36, 37, 127, 136].

Now, let's consider the electronic case. Considering L_c as the coherence length of the photo-excited electrons in the TERS process, Figure 4.12 (a) shows how the photo-excited electron uncertainty ΔE changes from 20 meV when doped to around 50 meV near the neutrality point. The experimental data [black bullets on Figure 4.12 (a)] were calculated using

$$\Delta E = \frac{v_F \hbar}{L_c}, \tag{4.9}$$

where $v_F = 1 \times 10^6$ m/s is the Fermi velocity and L_c was obtained experimentally in section 4.3. The G band FWHM [Figure 4.12 (b)] and frequency [Figure 4.12 (c)] can then be fit

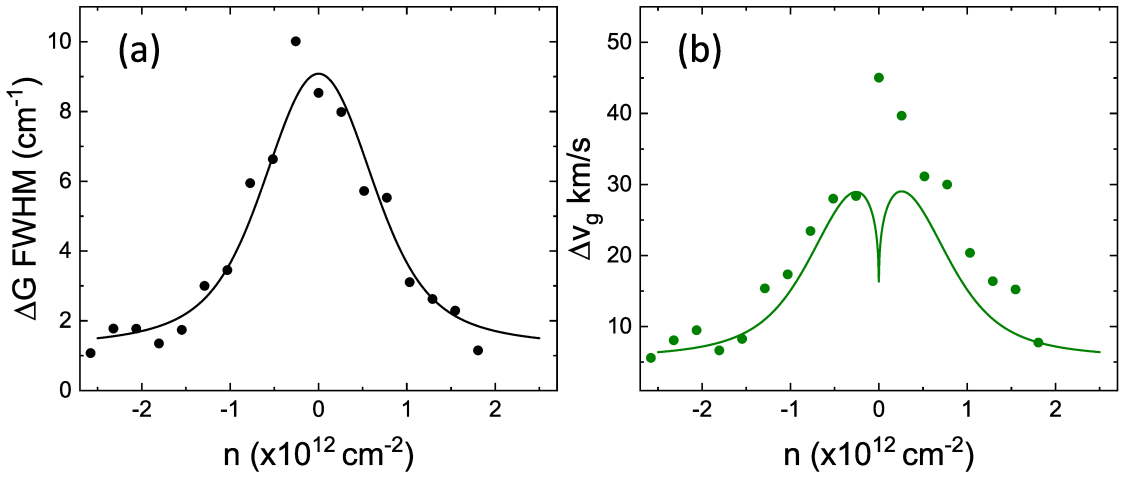

Figure 4.11: (a) Variation of the full width at half maximum (FWHM) of the G band due to the Kohn anomaly [ΔG FWHM = (G FWHM) - 8 cm^{-1}] as a function of n, fitted using the theory in [37]. (b) Δv_g of the G phonon as a function of n calculated using equation 4.8 with the values for τ_{ph} obtained from (a) and L_c from the results on section 4.3.

with the variable δE (red lines) obtained in Figure 4.12 (a), showing results consistent with the measured data (black dots). The blue line in Figures 4.12 (b) and (c) are the dependencies obtained with a fixed ΔE = 40 meV for the excitation laser line of 633 nm [136] for comparison.

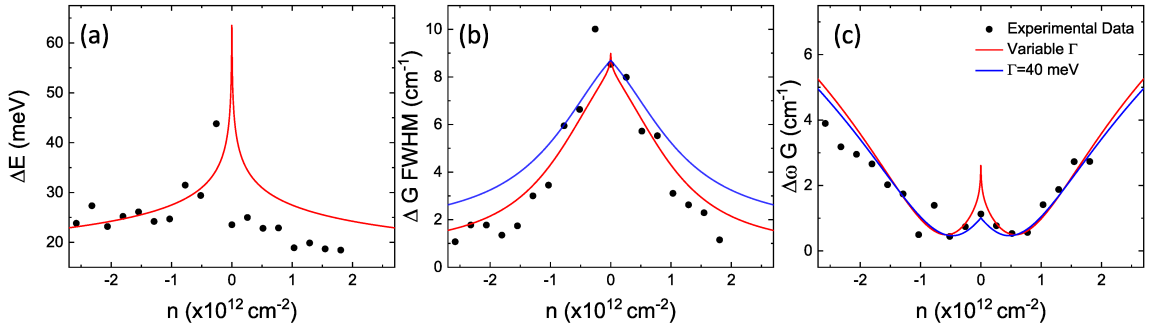

Figure 4.12: (a) Photo-induced electron energy level uncertainty ΔE as a function of n. Using equation 4.9, the experimental data (black bullets) and modeling (red line) were converted from the values obtained for L_c in section 4.3. (b,c) Variation of the full width at half maximum (Δ G FWHM = measured G FWHM - 8 cm^{-1}) (b) and frequency $\Delta\omega$ (c) of the G band due to the Kohn anomaly as a function of n, fitted using the theory in [37, 127]. The experimental data are represented as the black bullets and two modelings can be found: one with variable ΔE from (a) (red lines) and one with fixed ΔE = 40 meV [136](blue lines).

Although the data in 4.12 can be well represented with the electronic assignment for L_c, what is troublesome is that there is in the literature sufficient experimental and theoretical evidence that the electron coherence length for optically activated electrons in the Raman process is in the 3-4 nm range when analyzed based on the defect induced D-band [134, 137–140]. For instance, in reference [137], the turning point of the intensity ratio I_D/I_G at 3-4 nm is dictated by the electronic coherence length, being a measure of it. Furthermore, direct evidence of this electronic coherence length has been measured directly with TERS recently [30]. It is true that this electronic coherence length relies on the Raman scattering from the defect induced

(D) band, and one can argue that defects can decrease the electron lifetime, thus decreasing the coherence length. However, Ferrari and Basko addressed the electronic broadening in reference [18] and the 3-4 meV value is consistent with what is expected for resonance Raman where one of the scattering processes (either incident or scattered light emission) happens through a "virtual" state, which is far from the real state by the phonon energy. In this case, the electronic coherence length is given by $\ell \approx v_F/\Omega_{ph} \approx 3.5$ nm, where $v_F \approx 10^8$ cm/s is the Fermi velocity and $\Omega_{ph} = 0.2$ eV is the phonon energy, in agreement with the experimentally measured values. This is valid for the G, D and 2D scattering.

Another possibility we should still consider is the fact that the 2D band scattering can also happen through a triple-resonance process, where all the involved electronic states are real. In this case the energy uncertainty in the excited states should be of the order of the broadening ΔE (see reference [18]), which is a few tens of meV, leading to a one order of magnitude higher values for the electronic coherence length for these specific 2D band processes. In this scenario, we should consider the G band coherence length as 3-4 nm and the 2D band coherence length as 30-40 nm. However, if we use those numbers for the coherent TERS scattering, the G band should increase more than the 2D band in the TERS approach curve experiments, leading to I_{2D}/I_G ratio (ρ) that decreases instead of increasing (see black curve in Figure 4.13), inconsistent with the observed results that follow the red curve in Figure 4.13.

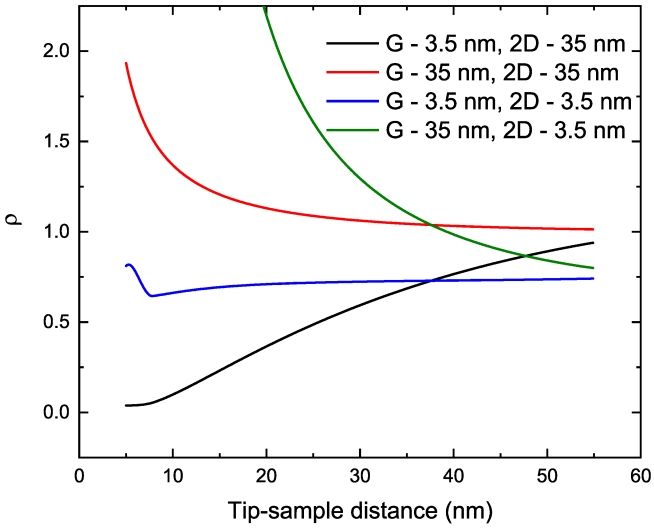

Figure 4.13: Theoretical plot of ρ as a function of tip-sample distance using the same L_c = 35 nm for the G and 2D bands (red) and using different L_c values for the 2D and G bands (respectively): 3.5 and 35 nm (black), 3.5 and 3.5 nm (blue) and 35 and 3.5 nm (green). For all curves the parameters r_{tip} and f_e are fixed at 7.5 nm and 4, respectively.

Moreover, if the coherence length of the process is the same for both bands, but both at 3.5 nm, the theory do not represents what happens in the experiment (blue curve in Figure 4.13). Finally, for completion, if the G L_c is larger than 2D by one order of magnitude (green curve in Figure 4.13), ρ increases more rapidly than the actual experiments, which, again, does not reflect the data.

In summary, despite the several arguments presented above, we understand it is not possible

to undoubtedly assign L_c as due to electrons or phonons. There is a bias towards the phonon interpretation because of the nature of the coherent TERS experiment. We consider that, even though the Raman scattering process takes place inside the material in a relatively small region dictated by the electronic coherence length, which should be in the 3-4 nm range, the experiment we perform probes the interference of electromagnetic fields at the TERS tip, and how it changes when you change the tip-sample distance. The interference we measure considers the different paths of the incoming and scattered electromagnetic waves traveling between the tip and the sample, and within the sample, a larger area given by the phonon coherence length (30-40 nm) has to be taken into account, considering that within this area the vibrations dictating the scattered field distribution exhibit fixed phases. We understand this picture leads to an ultra-strong phonon softening, i.e. to values of phonon group velocity that have not been neither measured nor predicted. However, we can argue that: (i) previous experimental works do not get as close to the Γ point in the Brillouin zone as the optical Raman experiment does ($10^{-4}\times$ the first Brillouin zone dimension); (ii) theory may be missing some fundamental aspect, as it was missing the Kohn anomaly two decades ago; (iii) the particle-like picture defining L_c/τ_c may be misleading.

In the phonon interpretation, it is worth noting that the lifetime of optical phonons, τ_{ph}, is a measure accessible in the conventional Raman spectroscopy, as it can be extracted from the peak widths by means of the Heisenberg uncertainty principle, as performed in this paper. The development of ultra-fast optics made it possible to carry out time-resolved spectroscopy experiments, which have already confirmed the τ_{ph} values obtained through the Raman linewidth [141, 142]. However, the coherence length, and consequently the group velocity near the Γ point, as defined by $v_g = L_c/\tau_{ph}$, remained inaccessible. The fact that interference effects are detectable in the near-field regime makes TERS a technique capable of measuring L_c and, in the case of phonons dictating the coherence TERS, Δv_g near the center of the Brillouin zone, revealing unusually high optical phonon group velocity for graphene in the ballistic regime.

In the electron interpretation, our results imply that the electronic energy uncertainty ΔE is not constant, but it rather varies with doping, probably due to electron-electron interaction, as suggested previously based on 2D-band analysis [143]. The values obtained from $\Delta E = v_F\hbar/L_c$ are still debatable, being consistent with some works in the literature [136] and inconsistent with others [18, 30, 134, 137–140].

By establishing the coherence length, a previously unavailable quantity, our results might be relevant to understand strongly correlated phenomena in graphene [144, 145], and to improve the present models based on the Kohn anomaly. The protocol is not limited to graphehe, it can be utilized in other materials, with important consequences in optical and transport phenomena.

Chapter 5

TERS and TEPL of TMDs

This chapter will cover works that are yet to be published regarding TERS and TEPL of TMDs. It will be divided into three parts. The first will be the TERS spectra on the TMDs, displaying the challenges in the measurements and in the data analysis, specially in comparison to graphene. Second, we will apply the same methodology presented in section 2.2.1 to analyze the effects of coherence in two-dimensional systems. Finally, we will analyze the localized emissions of these TMDs, in which it will comprehend the TEPL part of this thesis, as well as nano-bubbles and substrate roughness effect in the TERS and TEPL of TMDs.

5.1 TERS of MoS_2, WS_2, $MoSe_2$ and WSe_2

Here we begin with the TERS of the TMDs. The first challenge one has when attempting to measure TERS of TMDs is that, unlike graphene, they are semi conductors, presenting photon emissions (PL) when the electrons are excited above the gap energy. The laser used is the HeNe (1.96 eV), which is high enough to excite all the TMDs studied, and the Raman response is very close to the PL. For instance, in MoS_2 and WS_2 the Raman is a "shoulder" of the PL spectra [see Figures 2.5 (a) and (b)]. This is an issue because when using high NA objective lens (for instance, 1.4 as used in this work), the PL spectra can be saturated, meaning that when the focus is optimal for Raman, the PL quenches. Therefore, the maximum PL emission is not in the Raman focus. Since TERS is highly dependent in focus, this phenomenon hinders the tip alignment process.

Raman spectra were taken with (orange) and without (black) the presence of the tip for MoS_2, WS_2, $MoSe_2$ and WSe_2 monolayers and the spectra are displayed in Figure 5.1 (a)-(d), respectively. Unlike graphene, the totally symmetric A mode is not always clearly distinguishable from the non-totally symmetric E mode. In addition, there are several other Raman peaks with similar energies impacting the peak fitting process. Therefore, although the spectral enhancement factor (SEF) is evident for all TMDs in Figures 5.1, to analyze near field interference phenomena one needs to fit them properly.

Figures 5.2 (a)-(d) and (e)-(h) corresponds to the far-field and near-field data (black and orange bullets, respectivelly) with the Raman band fits below. Here we will focus in the totally

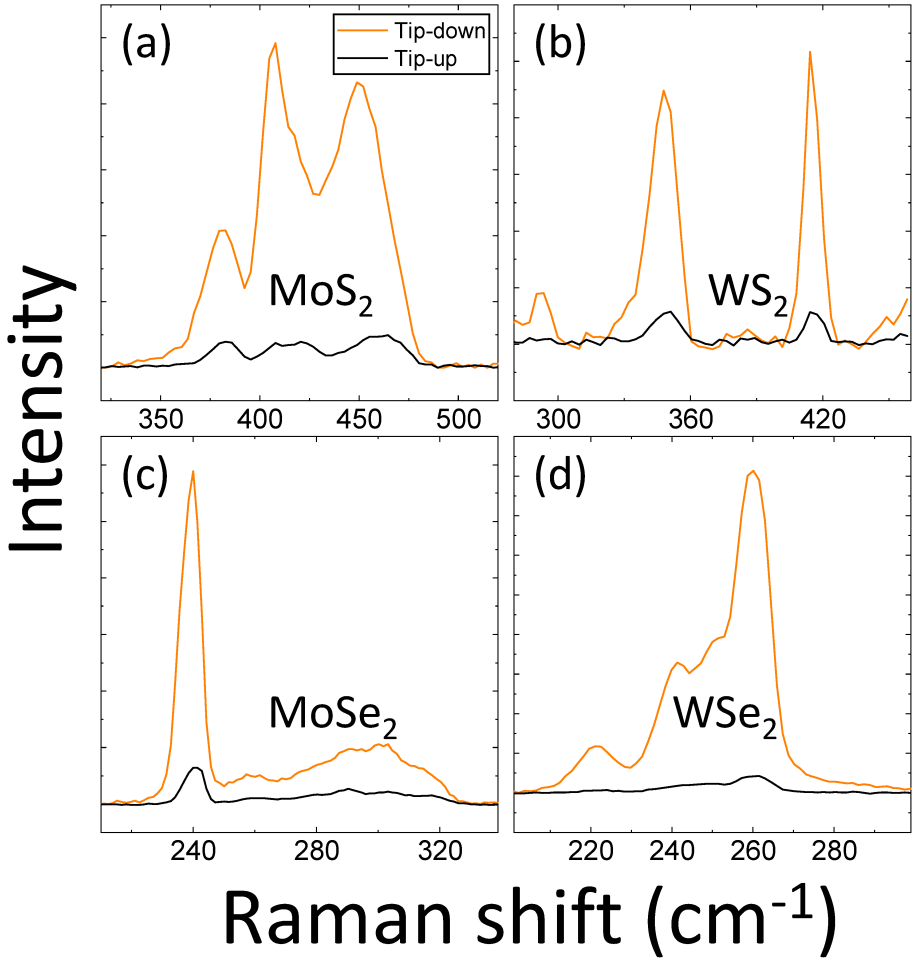

Figure 5.1: Near field (orange) and far field (black) Raman spectra of monolayer (a) MoS_2, (b) WS_2, (c) $MoSe_2$ and (d) WSe_2, respectivelly. Each spectra for each material were taken with different parameters aiming the best spectra quality. The spectra with and without the tip for each material were acquired using the same parameters. For MoS_2 and $MoSe_2$ the spectra were taken with 200 μW laser power, 5 accumulations of 5 s. WSe_2 and WS_2 were both exposed to 20 μW of laser power, with 5 accumulations of 5s for the first and 25 accumulations of 1 s for the latter due to WS_2's electronic energy gap being very close to 632.8 nm (our excitation laser) [146].

symmetric A-type and non-totally symmetric E-type modes, and they are displayed as the red and blue thick lines, respectivelly. The sum of all fits are displayed as a black solid line passing through the experimental data and the color code for the other fits are as follows: since we are not analyzing the influence of further peaks, we simply assigned them as p_1, p_2, p_3 and p_4 as green, magenta, cyan and orange in the other that they appear in the fit from lower to higher frequency. The 2LA peak is one exception to this color code and it is displayed as dark yellow.

First, we discuss MoS_2 [Figure 5.2 (a) and (e)]. Here, the fitting was done following the assignments of reference [147] and the A_{1g} SEF was 16.5x. We stress that, even though there are usually only three peaks assigned (E^1_{2g}, A_{1g} and 2LA), it is clear in our data and in reference [147] that there is another peak (p_1) besides the A_{1g} and the so-called 2LA is actually the convolution of three lorenztzians (p_2, p_3 and p_4).

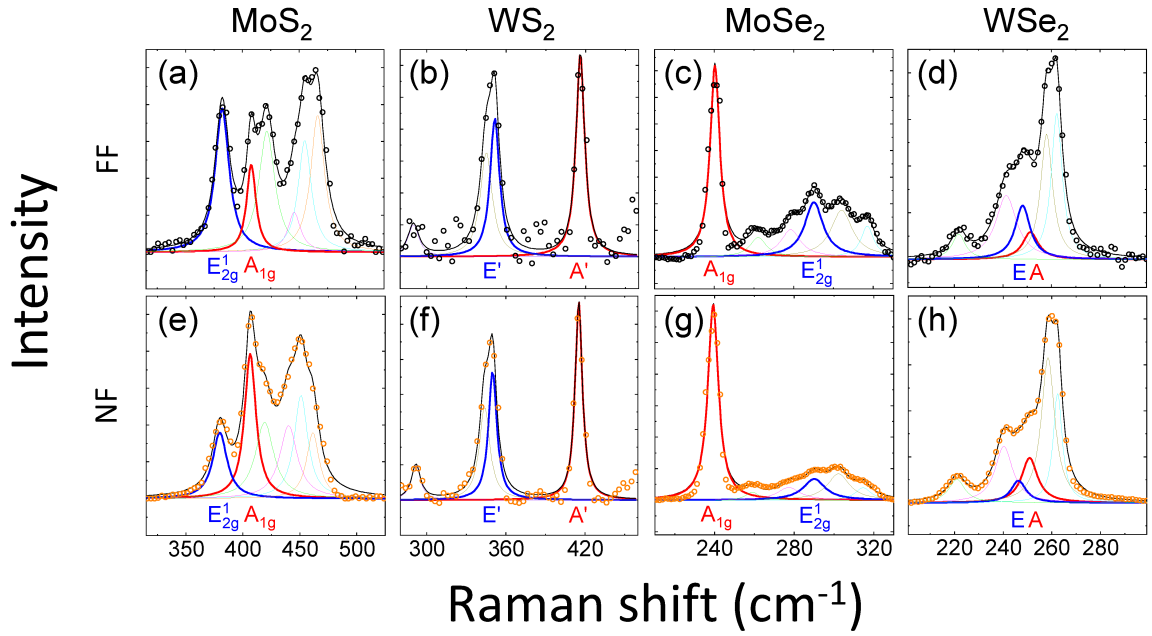

Figure 5.2: Raw far-field [black bullets, (a)-(d)] and near-field [orange bullets, (e)-(h)] data with the band fits. The main peaks of interest are the A (A_{1g}, A, A') and E (E^1_{2g}, E, E') are highlighted in blue and red, respectively, while the other fits displayed correspond to peaks that are not explored in the present work, and they follow the color code as explained in the text.

WS_2 FF and NF data with the fits are displayed in Figures 5.2 (b) and (f), respectively, and the A' SEF was 8.8x. Since the energy gap is very close to the laser, the FF data has a larger background noise, while the NF data is well defined due to the tip's enhancement. The peak assignments were done according to reference [148].

$MoSe_2$ FF and NF data with the fits are displayed in Figures 5.2 (c) and (g), respectively, and the A_{1g} SEF was 8.6x. Here, the A_{1g} peak is well separated from the other peaks and its fitting is trivial. However, that is not the case for the E^1_{2g} peak, where it is in the middle of three other lorentzians. The assignment was done according to reference [149].

WSe_2 FF and NF data with the fits are displayed in Figures 5.2 (d) and (h), respectively, and the A SEF was 33x. Here, since the A and E peaks are almost degenerate the fitting process is not trivial. Nevertheless, the assignment was done according to reference [150]. Besides the A and E almost degeneracy, for the laser line used in this work, there are many other peaks that appear in the same window of analysis and 4 other lorentzians were needed to accurately fit the data.

5.2 Coherence on TMDs

Near field interference theory states that a totally symmetric mode should experience only constructive interference when inside the Raman coherence length [22], while non-totally symmetric modes experience both constructive and destructive interference. Hence, this translates to a higher enhancement factor for the symmetric modes over the non-symmetric

ones. This has been widely seen for graphene in previous works [21–23].

Now that we have assigned the peaks in Figure 5.2 we can perform the analysis to determine the Raman coherence length for each TMD. This is done by ploting the so-called approach curves [20], similarly to what was done in section 4.3. First, we plot the intensity of the totally symmetric A peak and the non-totally symmetric E peak as a function of the tip-sample distance, as displayed in Figures 5.3 (a)-(d). Here, the intensities are normalized by the FF and thus this gives a direct value for the peak's enhancement factor. Notice that the highest enhancement for the samples differ from what is seen in Figure 5.1 (in Figure 5.3, the enhancement is always smaller). This is because, when performing the measurements in Figure 5.1, the near field is with the tip at 5 nm from the sample, while in the far field the tip is $\approx$1 μm away. In the approach curve experiments (Figure 5.3), while the near field closest to the sample is the same 5 nm, the far field is taken at 55 nm away. Thus, a mirror effect (light reflecting not on the tip itself, but at the plateau) non-related to the near field signal is present, which does not happen when the tip is at $\approx$1 μm away. Again, due to each material's specificity, different parameters were used to perform the measurements and it will be specified in the following paragraphs for each material.

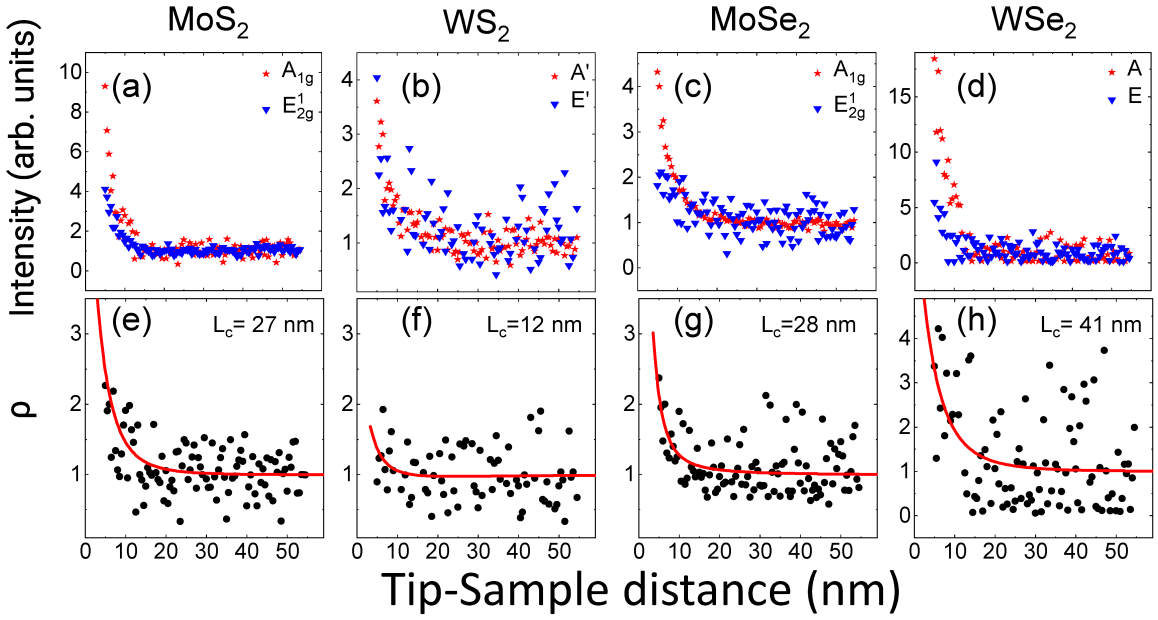

Figure 5.3: Approach curves for the A (A_{1g}, A, A') and E (E^1_{2g}, E, E') peaks for (a) MoS_2, (b) WS_2, (c) $MoSe_2$ and (d) WSe_2, repectivelly. All the intensities are normalized by the far field. (e)-(h) relative enhancement (ρ) for all the materials studied. The L_c values for each material are displayed inside the graphs. The tip's enhancement factor for all tips are $f_e = 7$ and r_{tip}s are (e) 13 nm, (f) 21 nm, (g) 11 nm, (h) 27 nm, respectively, which are all reasonable values.

Using the definition for relative enhancement (ρ) given by equation 4.4 and calculating the TERS intensity with equation 2.21, we can plot ρ as a function of tip sample distance for all TMDs [Figures 5.3 (e)-(h)].

Again, the fitting has three parameters: f_e, r_{tip} and L_c and we can find all three of them. Due to the PTTP high plasmonic response and repeatability, the tip's enhancement factors

are very high and equal for all experiments: $f_e = 7$. The tip's radii are different for each experiment and we find $r_{\text{tip}} = 13, 21, 11$ and 27 nm for the experiments envolving, MoS_2, WS_2, $MoSe_2$ and WSe_2, respectively. With these parameters set, we can finally extract L_c from the fit.

Figure 5.3 (a) displays the intensities for the A_{1g} and E^1_{2g} of MoS_2 as a function of tip-sample distance. Each spectra were acquired with 1 s accumulation time and 200 μW laser power. Again, plotting ρ as a function of tip-sample distance it is possible to perform the same procedure done for graphene in section 4.3 and we find $L_c = 27$ nm.

Repeating this over for all the other TMDs, with exposure time of 0.5 s, laser power of 200 μW for $MoSe_2$ and 20 μW for WS_2 and WSe_2, we can determine L_c. Figures 5.3 (b)-(d) plots the (non-)totally symmetric (E) A modes intensities and Figures 5.3 (f)-(h) plots ρ for WS_2, $MoSe_2$ and WSe_2, respectively. Therefore, we found L_c to be 12, 28 and 41 nm for the remaining materials.

It is noticeable that the coherence length of MoS_2 and $MoSe_2$ are very close together (27 and 28 nm). WS_2 on the other hand is considerably smaller (12 nm) and WSe_2 is considerably larger (41 nm). One disclaimer has to be done for both WS_2 and WSe_2. In the former, we are exciting the sample very close to the energy gap. Therefore, the fitting process is not easy with low acquisition time (which is necessary for the approach curve experiment) for when the tip is far from the sample (>15 nm) due to the PL. The latter, the Raman A and E modes are almost degenerate [150], in fact, the spectrometer's spectral resolution ($\approx 5\,\text{cm}^{-1}$) is worse than the separation between these modes, making the fitting likely inaccurate.

Here, it is important to highlight that all these experiments were performed under different experimental conditions, with different tips and laser power. Therefore, to confirm these experiments and the obtained values one must re-do this experiment under the same condition, especially with the same tip. This is a development that is being worked on, producing a sample with all the TMDs in the same region so one can perform the measurement more than once, with the same tip in all TMDs.

5.3 Localized emissions

As discussed in section 2.1.2, one important characteristics of TMDs is the fact that they are two-dimensional semi conductors. Thus, if one illuminates it with a laser with energy higher than the electronic gap, electrons can be promoted to the conduction band, relax to the bottom of the band and when it recombines with the hole left in the valance band, it emits a photon with the gap energy. This is the so-called conventional PL spectrocopy. However, when conducting this experiment, one is limited by the diffraction limit of light as well (equation 1.1), meaning that one can only distinguish these emissions from two different points in space by a distance about half of the wavelength of the light used. Thus, TEPL becomes an interesting technique to overcome the diffraction limit and analyze these emissions localized in space.

Moreover, the PL and Raman spectra of TMDs have been reported to be influenced by the substrate they are on [151, 152] for conventional measurements and for nano-scale

emissions [153]. Due to our experimental setup and high yield tips, we are able to expand these studies.

This section will provide TERS and TEPL measurements for MoS_2, WS_2, $MoSe_2$ and WSe_2 monolayers, as well as measurements of twisted bilayer MoS_2 and $MoSe_2$.

5.3.1 MoS_2

First, let's consider grain boundaries (GB) in a MoS_2 sample grown by chemical vapor deposition (CVD). This is the only sample in this thesis that is not assembled by mechanical exfoliation. CVD grown samples are more susceptible to grain boundaries, therefore, in order to study its optical properties, this sample had to be assembled differently. Nano-optical characterization of such samples have already been studied in the literature [75,87,91], however, they mostly present a quench in the Raman and PL signal in the GB region. This contradicts what have been observed via micro-Raman/PL spectroscopy, in which for freshly grown samples, the optical signals are enhanced in the GB region [154–156].

Figure 5.4 (a) presents a polarized second-harmonic generation (SHG) of a MoS_2 monolayer, characterized by a multi-sided polygonal shape. Due to the sensitivity of SHG in monolayer TMDs to material crystallographic orientation, utilizing polarized SHG measurements enables the identification of grain orientations and thereby exposes the existence of GB. Consequently, the varied SHG intensities observed in Figure 5.4 delimits individual grains and show their boundaries within the others MoS_2 monolayers.

In the red square in Figure 5.4 (a) a conventional PL spectra map is performed and the map is displayed in Figure 5.4 (b). Here, it is clear that, as shown by previous μ-PL works, the GB region present a PL enhancement, yet with "poor" spacial resolution.

Moreover, to determine the precise location and extent of optical modifications within these GB, we conducted TEPL measurements across specific regions highlighted by colored rectangles in Figure 5.4 (b). Figure 5.4 (c) shows the PL intensity maps from four TEPL hyperspectral measurements conducted along the regions of MoS_2 monolayer GB. The color encircling each map corresponds to the rectangular areas of the same color in Figure 5.4 (b) and we observe localized enhancements in PL intensity across all examined GB.

Aiming to measure the spatial extent of the optical alterations within these defects examined through NF measurements and contrast them with the spatial resolution of the FF measurements, Figure 5.4 (d) displays PL intensity profiles acquired along the black dashed arrow in Figure 5.4 (b), and the orange and purple dashed arrows in Figure 5.4 (c). The upper intensity profile graph in Figure 5.4 (d) illustrates a notable enhancement in spatial resolution provided by the tip. While the GB in the FF measurement exhibit spatial widths of approximately 650 nm, the lower intensity profile graphs reveal that the area impacted by these defects can be as narrow as 49 nm, which is close to our tip's maximum spatial resolution. Different GB exhibit distinct structural alterations, thus it's natural for them to also demonstrate different affected regions. For example, in the brown highlighted TEPL map of Figure 5.4 (c), a GB is shown with two distinct intensified lines, corresponding to a wider and brighter area in the FF PL map of Figure 5.4 (b). Figures 5.4 (e) and (f) compare the PL spectra of GB and

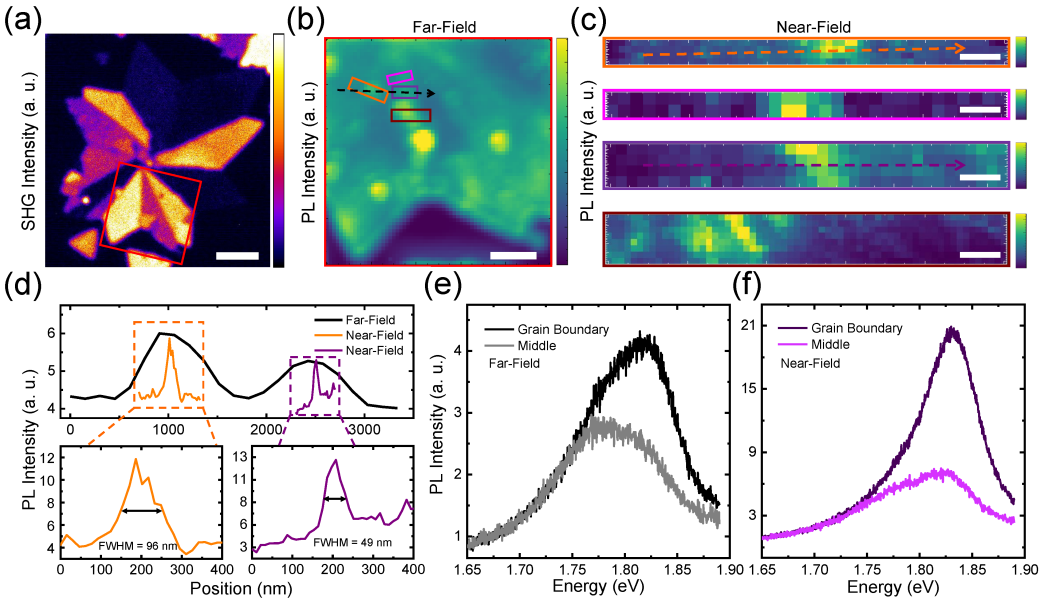

Figure 5.4: (a) Polarized Second Harmonic Generation (SHG) imaging was conducted on a monolayer of MoS_2 with a multi-sided polygonal structure. Variations in SHG intensities across regions indicate the presence of grains with different crystallographic orientations. The scale bar in (a) corresponds to 5 μm. (b) Photoluminescence (PL) intensity map obtained from a far field (FF) hyperspectral measurement within the highlighted area in (a) reveals an enhancement in PL intensity at the grain boundary regions. The scale bar in (b) represents 2 μm. (c) TEPL intensity maps from four near field (NF) hyperspectral measurements within the colored rectangular areas highlighted in (b) also exhibit a PL intensity increase at the grain boundaries. The colors of the rectangular areas in (b) correspond to the same colors surrounding the TEPL maps in (c). FF hyperspectral measurements were conducted with 150 nm steps, while NF measurements were performed with 16 nm steps. The scale bars in (c) range from 50, 100, 40 and 100 nm, respectively (from top to bottom). (d) PL intensity profiles along grain boundaries were obtained for both FF and NF measurements. The top graph illustrates the FF PL intensity profile in black [taken along the black dashed arrow in (b)] and the NF PL intensity profiles in orange and purple [taken along the respective dashed arrows in (c)]. The spatial width of the PL enhancement at the grain boundaries is shown in the bottom intensity profile graphs. (e) and (f) FF and NF PL spectra, respectively were obtained for both grain boundary and grain middle regions. These spectra correspond to the grain boundary region highlighted in the purple square in (b) and (c). NF measurements reveal the actual magnitude of the PL enhancement at the grain boundaries, indicating a dominance of exciton emission over trion emission suppression. Figure from [157].

grain middle regions under FF and NF conditions, respectively. The FF spectra exhibit a blue shift in PL energy and an increase in intensity at the GB. However, these characteristics are more pronounced in the NF spectra, providing a more accurate representation of the spectral alterations. As illustrated in Figure 5.4 (f), the grain middle region displays a PL spectrum featuring trion and exciton peaks with similar intensities. On the other hand, at the GB, there is a notable enhancement in the exciton peak, accompanied by a quenching of the trion peak, resulting in the observed blue shift in PL energy.

The results in Figure 5.4 are one instance of measurements performed in CVD grown

MoS_2. More results on TERS and TEPL can be found in reference [157].

5.3.2 WS_2

Next, we study WS_2 monolayer. Since the laser we use for the measurements is the HeNe laser (1.96 eV) and WS_2 energy gap is very close to the laser energy [47], we do not see the full PL emission due to the long pass filter (see Figure 3.3). Therefore, one cannot perform TEPL in this sample with our current setup.

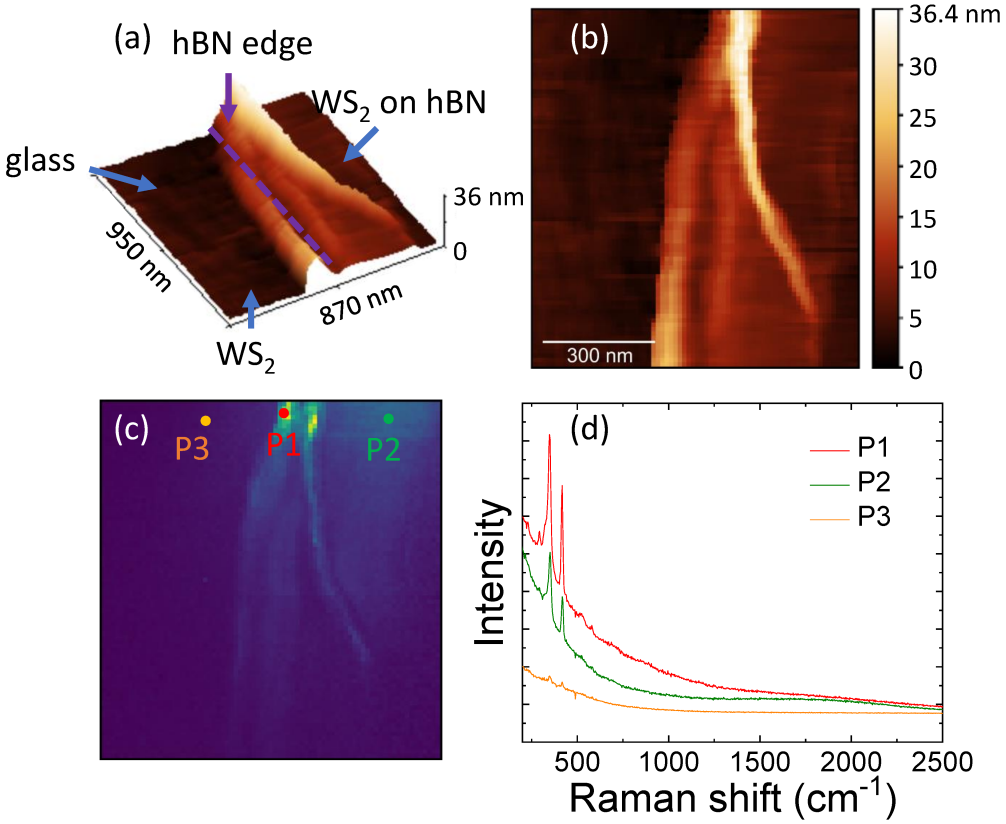

Figure 5.5: (a) 3D AFM map of a WS_2 on top of hBN and glass. Near the hBN border (purple dashed line) WS_2 formed a wrinkle. (b) 2D AFM of the same region, which corresponds to the same region analyzed in panels (c). (c) A_{1g} TERS map constructed with 128 points per line/column, 1.5x1.5 μm (interrupted in the 81st line - 950 nm due to tip's dis-alignment), 0.5 s per pixel, 20 μW laser power. (d) TERS spectra of three different points in the sample, P1 (red) on top of the wrinkle, P2 (green) on top of hBN and P3 (orange) on top of glass. Here, it is clear that the Raman signal is more intense on top of the wrinkle, and it is stronger on top of hBN than when on top of glass only.

Nevertheless, TERS is possible. It has another layer of difficulty, again, due to our laser excitation (the Raman is a "shoulder" of the PL and is not very intense, hindering the tip-alignment process). Figure 5.5 (a) shows a 3D AFM of the region of interest. In it, a WS_2 monolayer is disposed on top of glass and hBN (which in turn is on top of glass). The sample rolled over itself, forming a wrinkle at the border (purple dashed line). Figure 5.5 (b) shows the same AFM in panel (a), but in two dimensions. This is useful to compare with the TERS

map in Figure 5.5 (c). Here, it is mapped the A_{1g} TERS peak and it is clear that on top of the wrinkle the emission is very intense in comparison to the rest of the sample. Figure 5.5 (d) shows the spectra for three different points in the map in panel (b). P1 (red) is on top of the wrinkle and it presents the highest Raman intensity, while P2 (green) on top of hBN the signal is less intense than in P1 but it is more intense than P3 (orange) in glass. This result have been observed for wrinkles in a graphene sample [158] and the authors credit that to local strain and doping variations near the wrinkle, which is possible to be the case for WS_2 as well.

5.3.3 $MoSe_2$

Moving on to $MoSe_2$, Figure 5.6 display a similar sample as to Figure 5.5, but with $MoSe_2$ being the analyzed sample. Here, the sample is also positioned on top of glass and hBN with a wrinkle in the middle, as evidenced by the AFM [Figure 5.6 (e)]. Figure 5.6 (a), (b) and (c) display the TERS intensity, FWHM and position maps, respectively. The inset in Figure 5.6 (c) display the Raman spectra in three points, P1 (black) $MoSe_2$ on glass, P2 (red) on top of the wrinkle and P3 (magenta) $MoSe_2$ on top of hBN. The Raman intensity is enhanced on top of the wrinkle, same as for WS_2 in Figure 5.5 (c). However, unlike WS_2, the Raman intensity is higher on top of glass than on top of hBN. The FWHM appears to shine more on the hBN border in Figure 5.6 (b) and a blueshift in the Raman A_{1g} mode is observed in Figure 5.6 (c) on top of hBN and a redshift when on top of the wrinkle. This measurement was performed in such a way that both Raman and PL appear in the same window, that is, with a 300 lines/mm grating. Thus, the spectral resolution in the Raman bands is not great.

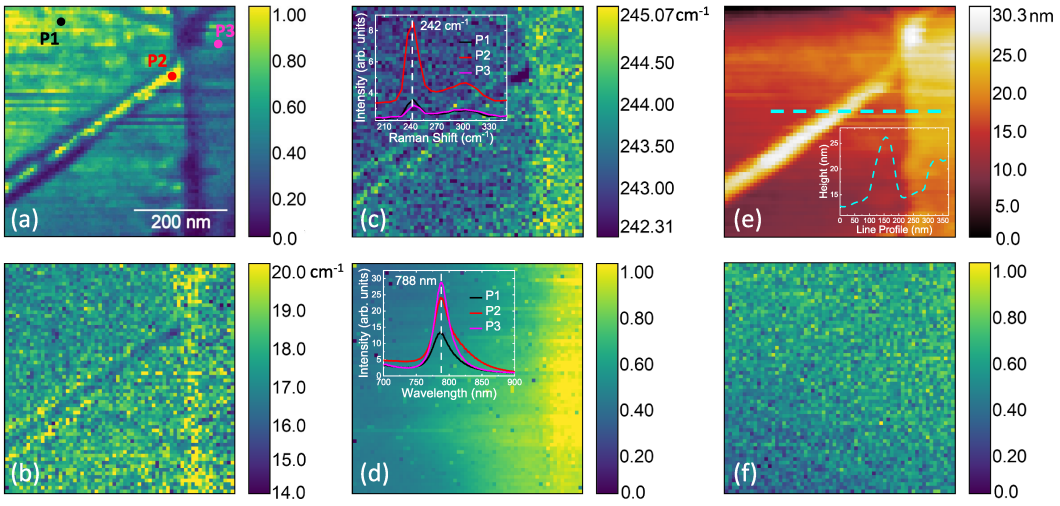

Figure 5.6: TERS measurements include (a) intensity, (b) FWHM, and (c) peak frequency pertaining to the A_{1g} vibrational mode; (d) integrated area of TEPL. The insets in (c, d) show TERS and TEPL spectral features at positions P1, P2, and P3 as indicated in (a). Additionally, (e) presents AFM data from the same location, and (f) illustrates micro-Raman intensity related to the A_{1g} vibrational mode, where just background noise is present. The measurement was conducted with 64 pixels per line/column, 0.5 s per pixel, 200 μW laser power.

When it comes to the TEPL map, Figure 5.6 (d) displays the PL integrated area and it

shows that there is a PL enhancement on top of hBN. Furthermore, in the inset of Figure 5.6 (d) it is clear that when on top of the wrinkle (P2), there is an appearance of a trion-like shoulder that it is likely due to doping on top of the hBN. For comparison, Figure 5.6 (f) display the far-field Raman map, where the features seen with TERS are not visible at all.

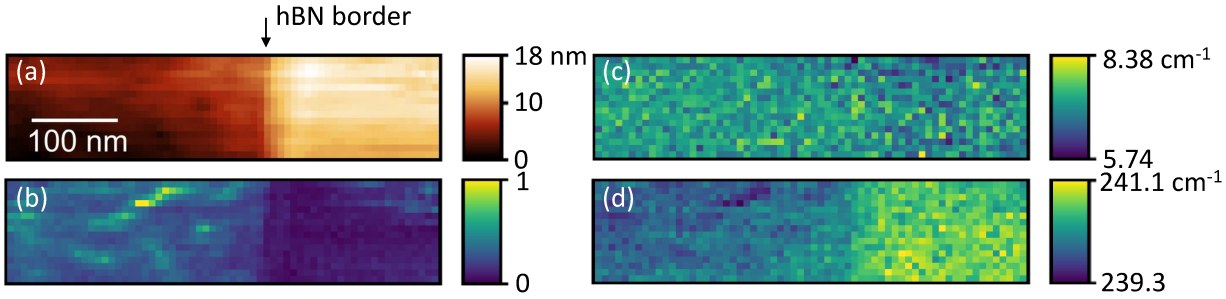

Figure 5.7: (a)AFM map of a $MoSe_2$ on top of hBN and glass. A_{1g} Raman intensity (b), (c) FWHM and (d) position map, showing that on top of hBN the signal is less intense and suffers a blueshift. No significant features are observed in the FWHM nor on the other Raman bands. The measurement was conducted with 64 pixels per line and 16 per column, 0.5 s per pixel, 200 μW laser power.

To further study this glass-hBN interface, another measurement in the same sample is performed in a position without the wrinkle, but with a 1200 lines/mm grading, providing a greater spectral resolution to the Raman peaks. Figure 5.7 (a) shows the AFM for this measurement, in which is highlighted the hBN border. The A_{1g} TERS map is displayed in Figure 5.7 (b), in which it is possible to confirm that it quenches on top of hBN. Furthermore, local spots of high intensity are visible on glass, which are most likely due to the substrate features (not visible in the AFM because they are much smaller than the hBN height). Figure 5.7 (c) and (d) display the A_{1g} Raman FWHM and position, respectively. Here, while one can maybe see a increase on the FWHM on top of glass, it is clear that the red and blue shifts reported in Figure 5.6 (c) are confirmed on top of the topography feature (on glass) and on top of hBN.

5.3.4 WSe_2

Finally, the last TMD monolayer studied is WSe_2. Figures 5.8 (a) and (b) display the AFM (3D and 2D, repectively). Here, the WSe_2 flake was cropped when transferring (it was supposed to be the same way as the measurements performed for WS_2 and $MoSe_2$) and at first glance the flake was entirely on top of hBN, however, the TERS map in Figure 5.8 (c) show that in fact after the hBN border, a small portion of WSe_2 can be found on top of glass only. Moreover, it is possible to see that on the bubble at the bottom part of the map, the TERS signal is quenched, which is the opposite to what happened in the other TMDs wrinkles studied so far. For comparison, Figure 5.8 (d) show the conventional Raman map and is not possible to see any features. This is probably due to a combination of two factors: not enough spacial resolution in the map for μRaman (500x500 nm map) and very low laser power for Raman (2 μW), making the Raman peaks shine only with the aid of the tip's enhancement.

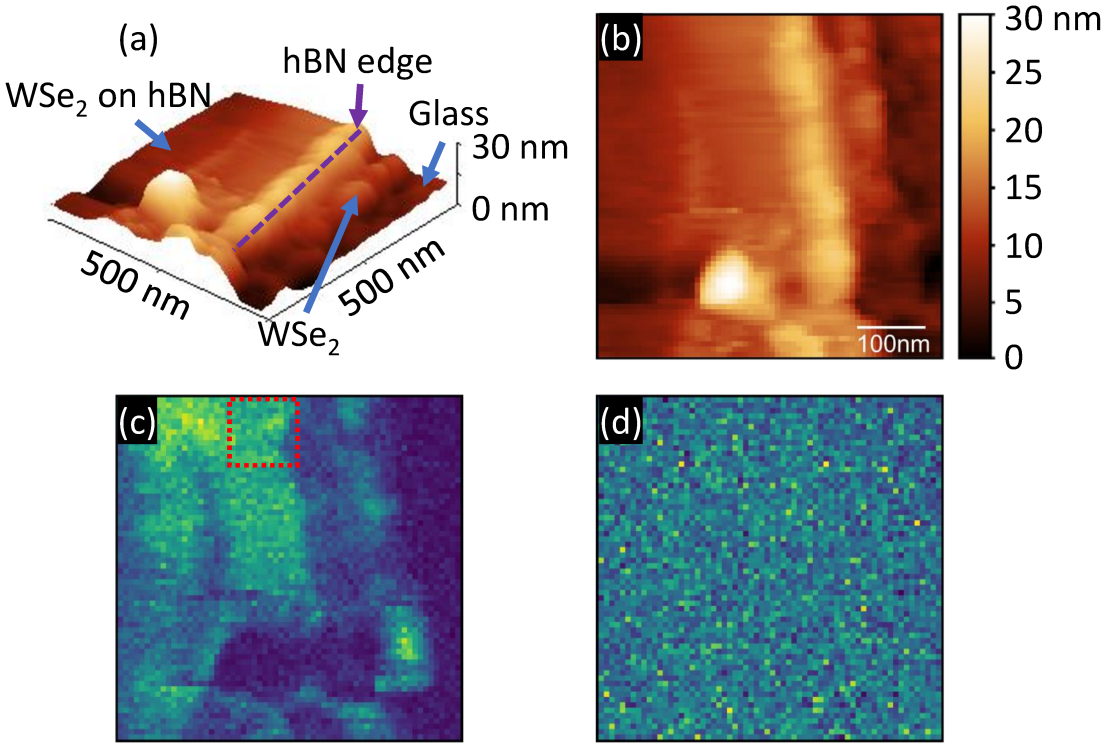

Figure 5.8: (a) 3D AFM map of a WSe_2 on top of hBN and glass. The WSe_2 is present on glass for a very short region after the edge of the hBN (purple dashed line). (b) 2D AFM of the same region, which corresponds to the same region analyzed in panels (c) and (d). (c) TERS map where the Raman signal is weaker on top of the hBN border and shines again when on top of glass. The Raman signal on top of the bouble is weaker than in the rest of the sample. The red square is the region in which TEPL maps were performed (refer to Figure 5.9) (d) Conventional Raman map of the same region as panel (c). Panels (c) and (d) were constructed with 64 points per line/column, 500x500 nm, 0.5 accumulation time per pixel and 2 μW laser power.

At the top middle part of the map (red dashed square) on Figure 5.8 (c) an interesting emission caught the attention in the TEPL spectra and other measurements were carried out in the same region, but with a smaller pixel size (100x100 nm with 32 pixels per line/column) and the results are shown in Figure 5.9.

The maps were taken with two different laser power because we suspect that this is emission comes from a defect island, 2 μW [Figure 5.9 (a)-(d)] and 20 μW [Figure 5.9 (e)-(h)]. Figure 5.9 (a) and (e) show the exciton intensity showing no major change across the 100x100 nm map. However, there are more emissions in this map, one centered at 783 nm [1.58 eV, Figures 5.9 (b) and (f)] and another centered at 813 nm [1.52 eV, Figures 5.9 (c) and (g)]. No features in the AFM are seen [Figures 5.9 (d) and (h)], but the border is close to the defect region, therefore it might be inducing a strain in the region.

Figures 5.9 (i) and (j) show the spectra at the points P1 (black), P2 (orange), P3 (blue) and P4 (magenta) showing that there is a quench in the PL signal on top of the defect region, but it does not clearly define the defect as well as the other two emissions. The defects should obey a sub-linear dependence with laser power, whereas the exciton should obey a

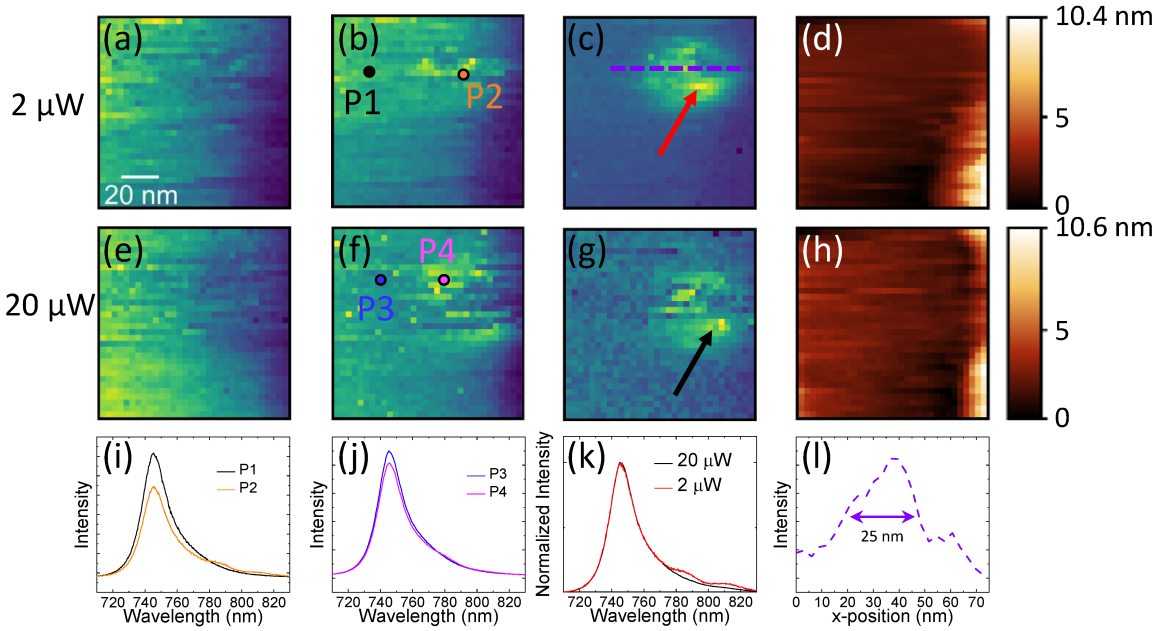

Figure 5.9: TEPL maps of the region highlighted in Figure 5.8 (c) performed for two different laser powers [(a)-(c) 2 μW and (e)-(g) 20 μW]. (a) and (e) display the exciton intensity, with no clear change in the vicinity of the defect island. (b) and (f) display the intensity of the emission centered at around 783 nm. Same done in (c) and (g) but for the emission at around 813 nm. The AFM [panels (d) and (h)] don't show any clear bubble or similar in the defect island region, empowering the vacancy defect island assignment. Different spectra in the maps are highlighted in panels (i) and (j), namely P1, P2, P3 and P4, showing that in the defect island region the emissions are clear (P2, orange and P4, magenta) when in comparison to regular WSe_2 (P1, black and P3, blue). (k) displays the spectra of the points pointed by the red and black arrows in panels (c) and (g). Here, we are comparing the same point in space with two different laser powers, normalized by the exciton energy. The intensity of the lower energy emissions are more clear in the 2 μW (black) in comparison to the 20 μW (red) one. The reason for that is that defects have a sub-linear dependence with laser power, whereas the exciton is linear. (l) display the purple line profile in panel (c), where the width of the defect region is $\approx$ 25 nm, which is close to our spatial resolution limit. The maps were acquired both with 32 points per line/column, 100x100 nm and 0.5 s accumulation time per pixel.

linear dependence [16, 159], therefore, analyzing the same point in space denoted by the red and black arrows in Figures 5.9 (c) and (g), one can normalize by the exciton intensity and the results are displayed in Figure 5.9 (k). Here, since the two peaks at 783 and 813 nm are more pronounced in the 2 μW over the 20 μW spectrum, the dependence can be assigned as sub-linear, hinting as towards a defect emission. Moreover, if one takes a line profile of the 813 nm emission one can see that the size of the defect island is in the order of tens of nanometers, which is in the order of the spacial resolution given by the tip [Figure 5.9 (l)].

5.3.5 Twisted homobilayer TMDs

Another very interesting feature that TERS and TEPL might be able to see are the optical and vibrational properties of Moire structures in twisted samples. This was previously done in

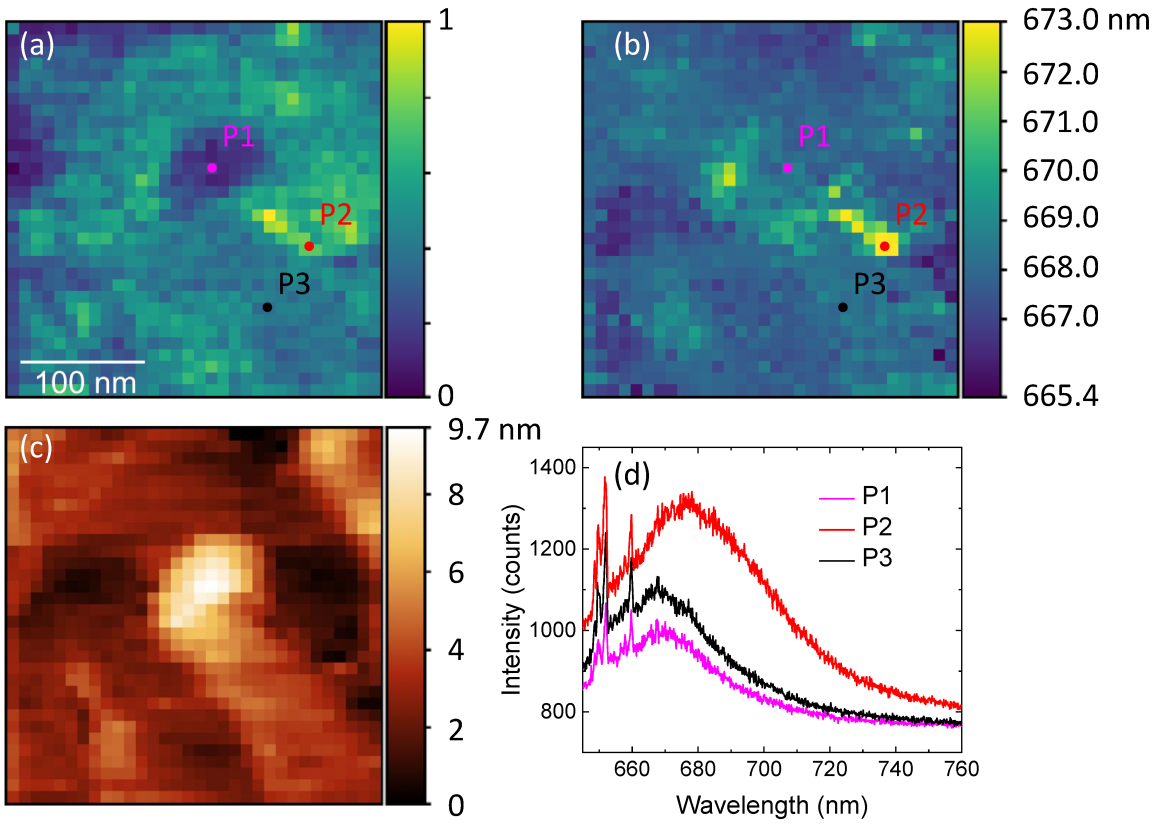

Figure 5.10: (a) E^1_{2g} TERS intensity map of a twisted bilayer MoS_2 at 58 degrees. The points P1 (magenta), P2 (red) and P3 (black) are points of interest in which in P1 the signal is weaker due to the AFM feature [panel (c)]. (b) Exciton center wavelength (energy) in which there is a redshift in P2. (d) PL spectra for the points P1, P2 and P3, where it is clear the PL energy shift in P2, as well as the less intense Raman signal in P1 due to the topography. The map was acquired with 32 points per line/column, 0.5 s per pixel, 20 μW laser power.

low-angle twisted bilayer graphene [99] but it is still yet to be done for TMDs. The low-angle part is very important for TERS and TEPL because the spatial resolution has to be greater than the Moire lattice given by $L_M = \frac{a}{2sin(\frac{\theta}{2})}$, where the lattice parameter a is in the order of angstroms for graphene and TMDs, the tilt angle θ has to be small so the tip's resolution can image the localized features.

Aiming the moiré features, two samples were attempted. First, a twisted MoS_2 at ≈ 58 degrees (due to the hexagonal structure, it is equivalent to 2 degrees, a low angle) that was exfoliated and transferred using the pickup method [74] on top of an hBN flake (Figure 5.10) and second a twisted $MoSe_2$ below 5 degrees built with CVD grown flakes also transferred on top of hBN (Figure 5.11).

Since MoS_2 has the Raman very close to the PL for the HeNe laser, a simultaneous TERS and TEPL map was acquired. First, Figure 5.10 (a) show the TERS intensity map. At first glance, it could resemble a Moire structure and further analysis would be done towards it. However, in Figure 5.10 (c) the AFM clearly show that in the region of lowest Raman signal is also a region with high topography, much like Figure 5.8 (c). Moreover, one can plot the PL position over the same region [Figure 5.10 (b)] and at a intermediate region towards the

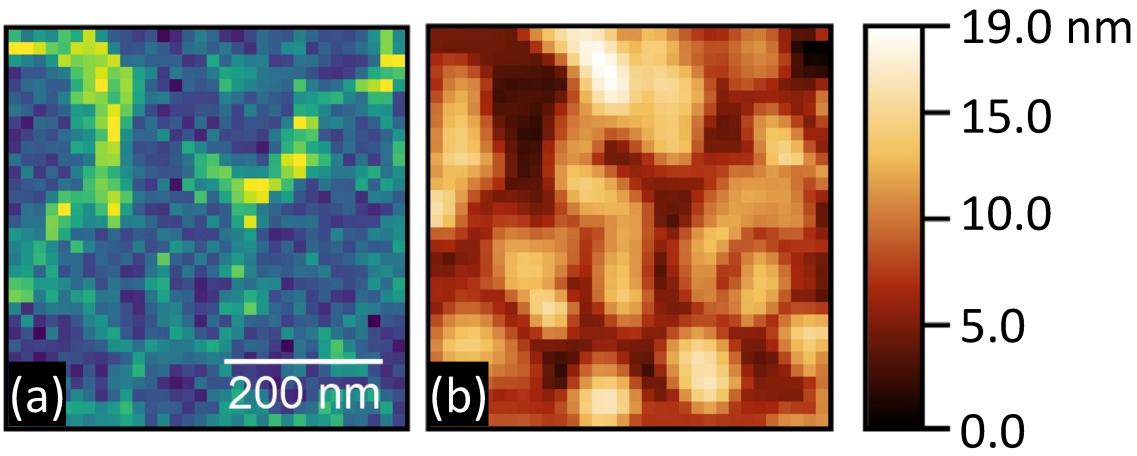

Figure 5.11: (a) TERS and (b) AFM of low angle (<5 degrees) twisted bilayer $MoSe_2$. The locations with higher A_{1g} TERS intensity in (a) match with the areas with lower topography in (b). The map was acquired with 32 points per line/column, 0.5 s per pixel and 200 μW laser power.

right bottom side of the bubble, where it suffers a very pronounced redshift. Figure 5.10 (d) shows the plots of three different points in the sample: inside the bubble region (P1, magenta), on the highest PL shift (P2, red) and in a regular region of the flake (P3, black). Here, it is evidenced the quench in the TERS signal when on top of the bubble and the shifted PL on P2. Bubbles have been reported to present shifts in the PL spectra [160], however, what is shown here is that even nano-bubbles affect the PL emission.

Finally, let's analyze the twisted $MoSe_2$ sample. Here, we performed a TERS measurement in a small region, again, Figure 5.11 (a) shows regions with clear higher TERS intensity. However, when looking at the topography [Figure 5.11 (b)], it is possible to perfectly match the areas with higher TERS signal with the lowest points in topography, much like Figures 5.8 (c) and 5.10 (a). These bubbles (or substrate features) are present throughout the whole samples of twisted MoS_2 and $MoSe_2$. Therefore, in order to study moiré features using TEPL and TERS, one needs a bubble free sample that the topography features will not interfere with the optical and vibrational properties of the moiré structure.

Chapter 6

Conclusion

In summary, TERS and TEPL of two-dimensional materials were performed to study the electronic, optical and vibrational properties of two dimensional materials, from graphene to monolayer and twisted bilayer TMDs.

A high quality graphene device was patterned for optical measurements tailored for the SNOM system (with no top hBN for TERS measurements) and due to the careful choice of gate metal, the Kohn anomaly effect at room temperature was observed by varying the number of charge carriers on the graphene surface and recording its Raman spectra.

Moreover, TERS measurements were done in this device and it was possible to probe the near field interference phenomena when varying the Fermi level. Raman spectroscopy is known to be a spatially incoherent phenomena, but this is only true in μ-Raman, in which the spatial resolution is limited by the wavelength of the light used. In nano-Raman, since the measurement takes place inside the so-called Raman coherence length, the Raman scattered photons can interfere. By varying the Fermi level, the Raman bands enhance differently for different number of charge carriers, showing the effects of near field interference in the totally and non-totally symmetric 2D and G bands of graphene TERS sprectra. Furthermore, it is shown that near the neutrality point, the Raman coherence length is smaller (≈ 7 nm) than when graphene is highly doped (≈ 40 nm) due to the Kohn anomaly modulation.

The concept of near field interference and coherence in TERS was expanded from graphene to TMDs, performing the approach curve experiments for MoS_2, WS_2, $MoSe_2$ and WSe_2 and probing the (non-)totally symmetric (E) A bands and the relation between them, assigning Raman coherence length for the TMDs. It is noticeable that for all TMDs studied the same trend observed for graphene are repeated here: the totally symmetric A band enhances more than the non-totally symmetric E band, despite all the differences that they present. For instance, in the TMDs, both A and E are first order Raman modes, whereas in graphene, only the E (G) band is first order. Moreover, graphene presents Kohn anomaly near the neutrality point, while TMDs do not. Among the four TMDs studied, MoS_2 and $MoSe_2$ present very close values of L_c, at 27 and 28 nm, respectively. WSe_2 presents the highest value for L_c at 41 nm, disclaiming the difficulty in fitting the A and E modes (they are almost degenerate), while WS_2's Raman coherence length is considerably smaller than the others at 12 nm. These experiments are the first steps towards the understanding of coherence in TMDs and further

experiments and theoretical development are still to be done to confirm or disprove this trend.

It is important to highlight that the analysis performed here is based on the assumption that L_c is the same for both A and E symmetry Raman modes. Finding the Raman coherence length by fitting the relative enhancement ρ provides an intrinsic metric that mitigates instabilities of the experiment, being the main way that most of the previous works used to find L_c. However, in reference [86], the authors assigned two different values for L_c for two A-type Raman modes in GaS, so there are clues that the coherence between different Raman modes is not the same. In this sense, further studies are needed in order to confirm whether L_c can be calculated using the ratio or if an individual treatment of the peaks is necessary.

The spatial resolution gain by the optically active tips also allowed the measurement of localized phenomena in TMDs, probing grain boundaries in CVD grown MoS_2, where an enhancement of the excitonic response is seen in the GB region, in the opposite direction of previous TEPL GB measurements. Furthermore, TERS variations in wrinkles of WS_2 and $MoSe_2$ were measured, showing an enhancement of the TERS signal strongly depends on the topography. Moreover, the influence of the substrate on the TERS and TEPL spectra of $MoSe_2$ showed that, when on top of hBN, the A_{1g} Raman mode decreases in intensity and in energy (it redshifts) in comparison when it is on top of glass. Finally, localized defects islands in WSe_2 were measured using two different laser powers, with no clear topography feature, displaying a defect in the order of 25 nm.

As future perspectives, TERS and TEPL can be applied to the studies in vertical and horizontal heterostructures, probing their unique properties provided by the different sample preparations. In particular, twisted bilayer samples present unique properties, among them, the moiré features that are yet to be seen and studied in twisted TMDs. To achieve that, one must prepare a nanometrically flat sample without bubbles and without top encapsulation. The nano bubbles observed in the twisted bilayer samples in this work presented strong correlation between topographic features and the TERS and TEPL signals, making it not possible to measure the moiré features.

6.1 List of publications

Published papers

1. A. R. Portes, R. B. Nadas, A. Jorio, and J. CORDOBA, “Electro-optical properties of a graphene device on a tip-enhanced raman spectroscopy system,” Optics Letters, vol. 56, no. 2, pp. 123–143, 2024.

2. R. B. Nadas, A. C. Gadelha, T. C. Barbosa, et al., “Spatially coherent tip-enhanced raman spectroscopy measurements of electron–phonon interaction in a graphene device,” Nano Letters, vol. 23, no. 19, pp. 8827–8832, 2023.

3. A. C. Gadelha, R. Nadas, T. C. Barbosa, et al., “Observation of well-defined kohn-anomaly in high-quality graphene devices at room temperature,” 2D Materials, vol. 9, no. 4, p. 045 028, 2022.

4. A. C. Gadelha, D. A. Ohlberg, C. Rabelo, et al., “Localization of lattice dynamics in low-angle twisted bilayer graphene,” Nature, vol. 590, no. 7846, pp. 405–409, 2021.

5. A. C. Gadelha, D. A. Ohlberg, F. C. Santana, et al., “Twisted bilayer graphene: A versatile fabrication method and the detection of variable nanometric strain caused by twist-angle disorder,” ACS Applied Nano Materials, vol. 4, no. 2, pp. 1858–1866, 2021.

6. L. M. Malard, L. Lafeta, R. S. Cunha, et al., “Studying 2d materials with advanced raman spectroscopy: CARS, SRS and TERS,” Physical Chemistry Chemical Physics, vol. 23, no. 41, pp. 23 428–23 444, 2021.

Submitted papers

1. F. B. Sousa, R. Nadas, R. Martins, A. P. M. Barboza, J. S. Soares, B. R. A. Neves, I. Silvestre, A. Jorio, L. M. Malard, "Nano-optical investigation of grain boundaries, strain and edges in CVD grown MoS2 monolayers"

2. A. Jorio, R. Nadas, A. G. Pereira, C. Rabelo, A. C. Gadelha, T. L. Vasconcelos, W. Zhang, Y. Miyata, R. Saito, M. D. Costa, L. G. Cancado, "Nano-Raman Spectroscopy of 2D Materials".

Papers under construction

1. R. Nadas et.al., "Spatial coherence in the tip-enhanced Raman spectroscopy of transition metal dichalcogenides: MoS2, MoSe2, WS2 and WSe2".

2. R. Nadas et. al., "Localized Emissions in Transition Metal Dichalcogenides".

Colaboration papers under construction

1. L. Liberal. et. al., "A Tip Enhancement Photoluminescence Spectroscopy (TEPL) approach on single photon emitters".

2. G. Soares et.al., "Localized angle and strain fields in twisted bilayer graphene by Nano-Raman spectral imaging"

Conference Presentations

1. Spatial coherence in 2D systems probed by nano-Raman spectroscopy, International Winterschool on Electronic Properties of Novel Materials (IWEPNM), Kirchberg, 2024.

2. Super-strong optical phonon energy renormalization measured by spatially coherent tip-enhanced Raman spectroscopy in a graphene device, XXI Brazilian MRS Meeting, Maceio, 2023.

3. Kohn anomaly modulation of graphene phonon coherence length and group velocity by gate-dependent nano-Raman spectroscopy, Brazilian Physical Society Autumn Meeting, Ouro Preto, 2023.

4. Tip-enhanced Raman spectroscopy and photoluminescence of transition metal dichalcogenides, III Encontro Anual da rede de estudos e aplicações de materiais 2D, Belo Horizonte, 2023.

5. Gate-Doping Dependent Tip Enhanced Raman Spectroscopy of Graphene Devices, TERS 8, Paris, 2022.

6. Gate-Doping Dependent Tip Enhanced Raman Spectroscopy of Graphene Devices, XX Brazilian MRS Meeting, Foz do Iguacu 2022.

Bibliography

[1] Gianluca Fiori, Francesco Bonaccorso, Giuseppe Iannaccone, Tomás Palacios, Daniel Neumaier, Alan Seabaugh, Sanjay K Banerjee, and Luigi Colombo. Electronics based on two-dimensional materials. *Nature nanotechnology*, 9(10):768–779, 2014.

[2] Kostya S Novoselov, Andre K Geim, Sergei V Morozov, De-eng Jiang, Yanshui Zhang, Sergey V Dubonos, Irina V Grigorieva, and Alexandr A Firsov. Electric field effect in atomically thin carbon films. *science*, 306(5696):666–669, 2004.

[3] Qing Hua Wang, Kourosh Kalantar-Zadeh, Andras Kis, Jonathan N Coleman, and Michael S Strano. Electronics and optoelectronics of two-dimensional transition metal dichalcogenides. *Nature nanotechnology*, 7(11):699–712, 2012.

[4] Manish Chhowalla, Hyeon Suk Shin, Goki Eda, Lain-Jong Li, Kian Ping Loh, and Hua Zhang. The chemistry of two-dimensional layered transition metal dichalcogenide nanosheets. *Nature chemistry*, 5(4):263–275, 2013.

[5] Saju Joseph, Jainy Mohan, Seetha Lakshmy, Simil Thomas, Brahmananda Chakraborty, Sabu Thomas, and Nandakumar Kalarikkal. A review of the synthesis, properties, and applications of 2d transition metal dichalcogenides and their heterostructures. *Materials Chemistry and Physics*, 297:127332, 2023.

[6] Chandrasekhara V Raman. A change of wave-length in light scattering. *Nature*, 121(3051):619–619, 1928.

[7] Ado Jorio, Mildred S Dresselhaus, Riichiro Saito, and Gene Dresselhaus. *Raman spectroscopy in graphene related systems*. John Wiley & Sons, 2011.

[8] Riichiro Saito, Y Tatsumi, Shengxi Huang, X Ling, and MS Dresselhaus. Raman spectroscopy of transition metal dichalcogenides. *Journal of Physics: Condensed Matter*, 28(35):353002, 2016.

[9] Andrea Splendiani, Liang Sun, Yuanbo Zhang, Tianshu Li, Jonghwan Kim, Chi-Yung Chim, Giulia Galli, and Feng Wang. Emerging photoluminescence in monolayer mos2. *Nano letters*, 10(4):1271–1275, 2010.

[10] E Abbe. Contributions to the theory of the microscope and microscopic observations(wave theory of light for optimal design of microscopes). *Arch. Mikrosk. Anat.,(Leipzig)*, 9:413–468, 1873.

[11] Rayleigh. Xxxi. investigations in optics, with special reference to the spectroscope. *The London, Edinburgh, and Dublin Philosophical Magazine and Journal of Science*, 8(49):261–274, 1879.

[12] EdwardH Synge. Xxxviii. a suggested method for extending microscopic resolution into the ultra-microscopic region. *The London, Edinburgh, and Dublin Philosophical Magazine and Journal of Science*, 6(35):356–362, 1928.

[13] Raoul M Stöckle, Yung Doug Suh, Volker Deckert, and Renato Zenobi. Nanoscale chemical analysis by tip-enhanced raman spectroscopy. *Chemical Physics Letters*, 318(1-3):131–136, 2000.

[14] Norihiko Hayazawa, Yasushi Inouye, Zouheir Sekkat, and Satoshi Kawata. Metallized tip amplification of near-field raman scattering. *Optics Communications*, 183(1-4):333–336, 2000.

[15] Hyeongwoo Lee, Dong Yun Lee, Min Gu Kang, Yeonjeong Koo, Taehyun Kim, and Kyoung-Duck Park. Tip-enhanced photoluminescence nano-spectroscopy and nano-imaging. *Nanophotonics*, 9(10):3089–3110, 2020.

[16] Zhong Lin, Bruno R Carvalho, Ethan Kahn, Ruitao Lv, Rahul Rao, Humberto Terrones, Marcos A Pimenta, and Mauricio Terrones. Defect engineering of two-dimensional transition metal dichalcogenides. *2D Materials*, 3(2):022002, 2016.

[17] Qijie Liang, Qian Zhang, Xiaoxu Zhao, Meizhuang Liu, and Andrew TS Wee. Defect engineering of two-dimensional transition-metal dichalcogenides: applications, challenges, and opportunities. *ACS nano*, 15(2):2165–2181, 2021.

[18] Andrea C Ferrari and Denis M Basko. Raman spectroscopy as a versatile tool for studying the properties of graphene. *Nature nanotechnology*, 8(4):235–246, 2013.

[19] Manish Chhowalla, Debdeep Jena, and Hua Zhang. Two-dimensional semiconductors for transistors. *Nature Reviews Materials*, 1(11):1–15, 2016.

[20] Luiz Gustavo Cançado, Ryan Beams, Ado Jorio, and Lukas Novotny. Theory of spatial coherence in near-field raman scattering. *Physical Review X*, 4(3):031054, 2014.

[21] Ryan Beams, Luiz Gustavo Cançado, Sang-Hyun Oh, Ado Jorio, and Lukas Novotny. Spatial coherence in near-field raman scattering. *Physical review letters*, 113(18):186101, 2014.

[22] Bruno C Publio, Bruno S Oliveira, Cassiano Rabelo, Hudson Miranda, Thiago L Vasconcelos, Ado Jorio, and Luiz Gustavo Cancado. Inclusion of the sample-tip interaction term in the theory of tip-enhanced raman spectroscopy. *Physical Review B*, 105(23):235414, 2022.

[23] Rafael Battistella Nadas, Andreij C Gadelha, Tiago C Barbosa, Cassiano Rabelo, Thiago de Lourenco e Vasconcelos, Vitor Monken, Ary VR Portes, Kenji Watanabe, Takashi Taniguchi, Jhonattan C Ramirez, et al. Spatially coherent tip-enhanced raman spectroscopy measurements of electron-phonon interaction in a graphene device. *Nano Letters*, 23(19):8827–8832, 2023.

[24] Deji Akinwande, Christopher J Brennan, J Scott Bunch, Philip Egberts, Jonathan R Felts, Huajian Gao, Rui Huang, Joon-Seok Kim, Teng Li, Yao Li, et al. A review on mechanics and mechanical properties of 2d materials—graphene and beyond. *Extreme Mechanics Letters*, 13:42–77, 2017.

[25] Gerardo G Naumis, Salvador Barraza-Lopez, Maurice Oliva-Leyva, and Humberto Terrones. Electronic and optical properties of strained graphene and other strained 2d materials: a review. *Reports on Progress in Physics*, 80(9):096501, 2017.

[26] Caterina Soldano, Ather Mahmood, and Erik Dujardin. Production, properties and potential of graphene. *Carbon*, 48(8):2127–2150, 2010.

[27] DSL Abergel, V Apalkov, J Berashevich, Klaus Ziegler, and Tapash Chakraborty. Properties of graphene: a theoretical perspective. *Advances in Physics*, 59(4):261–482, 2010.

[28] Sajedeh Manzeli, Dmitry Ovchinnikov, Diego Pasquier, Oleg V Yazyev, and Andras Kis. 2d transition metal dichalcogenides. *Nature Reviews Materials*, 2(8):1–15, 2017.

[29] Mildred S Dresselhaus, Gene Dresselhaus, and Ado Jorio. *Group theory: application to the physics of condensed matter*. Springer Science & Business Media, 2007.

[30] Hudson Miranda, Vitor Monken, João Luiz E Campos, Thiago L Vasconcelos, Cassiano Rabelo, Bráulio S Archanjo, Clara M Almeida, Sebastian Grieger, Claudia Backes, Ado Jorio, et al. Establishing the excitation field in tip-enhanced raman spectroscopy to study nanostructures within two-dimensional systems. *2D Materials*, 10(1):015002, 2022.

[31] Gunnar Moos, Cornelius Gahl, Roman Fasel, Martin Wolf, and Tobias Hertel. Anisotropy of quasiparticle lifetimes and the role of disorder in graphite from ultrafast time-resolved photoemission spectroscopy. *Physical review letters*, 87(26):267402, 2001.

[32] Tobias Kampfrath, Luca Perfetti, Florian Schapper, Christian Frischkorn, and Martin Wolf. Strongly coupled optical phonons in the ultrafast dynamics of the electronic energy and current relaxation in graphite. *Physical review letters*, 95(18):187403, 2005.

[33] Achim Hartschuh. New techniques for carbon-nanotube study and characterization. *Carbon Nanotubes: Advanced Topics in the Synthesis, Structure, Properties and Applications*, pages 371–393, 2008.

[34] Irene Calizo, Alexander A Balandin, Wenzhong Bao, Feng Miao, and CN Lau. Temperature dependence of the raman spectra of graphene and graphene multilayers. *Nano letters*, 7(9):2645–2649, 2007.

[35] S Piscanec, M Lazzeri, Francesco Mauri, AC Ferrari, and J Robertson. Kohn anomalies and electron-phonon interactions in graphite. *Physical review letters*, 93(18):185503, 2004.

[36] Anindya Das, Simone Pisana, Biswanath Chakraborty, Stefano Piscanec, Srijan K Saha, Umesh V Waghmare, Konstantin S Novoselov, Hulikal R Krishnamurthy, Andre K Geim, Andrea C Ferrari, et al. Monitoring dopants by raman scattering in an electrochemically top-gated graphene transistor. *Nature nanotechnology*, 3(4):210–215, 2008.

[37] Michele Lazzeri and Francesco Mauri. Nonadiabatic kohn anomaly in a doped graphene monolayer. *Physical review letters*, 97(26):266407, 2006.

[38] Ken-ichi Sasaki, Riichiro Saito, Gene Dresselhaus, Mildred S Dresselhaus, Hootan Farhat, and Jing Kong. Curvature-induced optical phonon frequency shift in metallic carbon nanotubes. *Physical Review B*, 77(24):245441, 2008.

[39] W Kohn. Image of the fermi surface in the vibration spectrum of a metal. *Physical Review Letters*, 2(9):393, 1959.

[40] Yilei Li. *Probing the response of two-dimensional crystals by optical spectroscopy*. springer, 2015.

[41] Jun Yan, Erik A Henriksen, Philip Kim, and Aron Pinczuk. Observation of anomalous phonon softening in bilayer graphene. *Physical review letters*, 101(13):136804, 2008.

[42] Kin Fai Mak, Changgu Lee, James Hone, Jie Shan, and Tony F Heinz. Atomically thin mos 2: a new direct-gap semiconductor. *Physical review letters*, 105(13):136805, 2010.

[43] Alexey Chernikov, Timothy C Berkelbach, Heather M Hill, Albert Rigosi, Yilei Li, Burak Aslan, David R Reichman, Mark S Hybertsen, and Tony F Heinz. Exciton binding energy and nonhydrogenic rydberg series in monolayer ws 2. *Physical review letters*, 113(7):076802, 2014.

[44] Hong Li, Qing Zhang, Chin Chong Ray Yap, Beng Kang Tay, Teo Hang Tong Edwin, Aurelien Olivier, and Dominique Baillargeat. From bulk to monolayer mos2: evolution of raman scattering. *Advanced Functional Materials*, 22(7):1385–1390, 2012.

[45] Dattatray J Late, Yi-Kai Huang, Bin Liu, Jagaran Acharya, Sharmila N Shirodkar, Jiajun Luo, Aiming Yan, Daniel Charles, Umesh V Waghmare, Vinayak P Dravid, et al. Sensing behavior of atomically thin-layered mos2 transistors. *ACS nano*, 7(6):4879–4891, 2013.

[46] Jiamin Quan, Lukas Linhart, Miao-Ling Lin, Daehun Lee, Jihang Zhu, Chun-Yuan Wang, Wei-Ting Hsu, Junho Choi, Jacob Embley, Carter Young, et al. Phonon renormalization in reconstructed mos2 moiré superlattices. *Nature materials*, 20(8):1100–1105, 2021.

[47] Jiwon Chang, Leonard F Register, and Sanjay K Banerjee. Ballistic performance comparison of monolayer transition metal dichalcogenide mx2 (m= mo, w; x= s, se, te) metal-oxide-semiconductor field effect transistors. *Journal of Applied Physics*, 115(8), 2014.

[48] Wei Shi, Miao-Ling Lin, Qing-Hai Tan, Xiao-Fen Qiao, Jun Zhang, and Ping-Heng Tan. Raman and photoluminescence spectra of two-dimensional nanocrystallites of monolayer ws2 and wse2. *2D Materials*, 3(2):025016, 2016.

[49] Yu Zhang, Yuyu Yao, Marshet Getaye Sendeku, Lei Yin, Xueying Zhan, Feng Wang, Zhenxing Wang, and Jun He. Recent progress in cvd growth of 2d transition metal dichalcogenides and related heterostructures. *Advanced materials*, 31(41):1901694, 2019.

[50] Paul Bazylewski, Sabastine Ezugwu, and Giovanni Fanchini. A review of three-dimensional scanning near-field optical microscopy (3d-snom) and its applications in nanoscale light management. *Applied Sciences*, 7(10):973, 2017.

[51] Lukas Novotny. Effective wavelength scaling for optical antennas. *Physical review letters*, 98(26):266802, 2007.

[52] Lukas Novotny. Optical antennas tuned to pitch. *Nature*, 455(7215):887–887, 2008.

[53] Thiago L Vasconcelos, Bráulio S Archanjo, Bruno S Oliveira, Rogério Valaski, Rafael C Cordeiro, Helton G Medeiros, Cassiano Rabelo, Aroldo Ribeiro, Peter Ercius, Carlos A Achete, et al. Plasmon-tunable tip pyramids: Monopole nanoantennas for near-field scanning optical microscopy. *Advanced Optical Materials*, 6(20):1800528, 2018.

[54] Peter Walke, Yasuhiko Fujita, Wannes Peeters, Shuichi Toyouchi, Wout Frederickx, Steven De Feyter, and Hiroshi Uji-i. Silver nanowires for highly reproducible cantilever based afm-ters microscopy: towards a universal ters probe. *Nanoscale*, 10(16):7556–7565, 2018.

[55] Antonino Foti, Francesco Barreca, Enza Fazio, Cristiano D'Andrea, Paolo Matteini, Onofrio Maria Maragò, and Pietro Giuseppe Gucciardi. Low cost tips for tip-enhanced raman spectroscopy fabricated by two-step electrochemical etching of 125 μm diameter gold wires. *Beilstein journal of nanotechnology*, 9(1):2718–2729, 2018.

[56] Bruno S Oliveira, Bráulio S Archanjo, Rogério Valaski, Carlos A Achete, Luiz Gustavo Cançado, Ado Jorio, and Thiago L Vasconcelos. Nanofabrication of plasmon-tunable

nanoantennas for tip-enhanced raman spectroscopy. *The Journal of Chemical Physics*, 153(11):114201, 2020.

[57] M Cardona. *Topics in applied physics*. Springer, 1984.

[58] William Hayes and Rodney Loudon. Scattering of light by crystals. *(No Title)*, 1978.

[59] WH Carter and E Wolf. Coherence properties of lambertian and non-lambertian sources. *JOSA*, 65(9):1067–1071, 1975.

[60] Rémi Carminati and Jean-Jacques Greffet. Near-field effects in spatial coherence of thermal sources. *Physical Review Letters*, 82(8):1660, 1999.

[61] Andrei V Shchegrov, Karl Joulain, Rémi Carminati, and Jean-Jacques Greffet. Near-field spectral effects due to electromagnetic surface excitations. *Physical Review Letters*, 85(7):1548, 2000.

[62] Hema Roychowdhury and Emil Wolf. Effects of spatial coherence on near-field spectra. *Optics letters*, 28(3):170–172, 2003.

[63] A Apostol and A Dogariu. Spatial correlations in the near field of random media. *Physical review letters*, 91(9):093901, 2003.

[64] Hema Roychowdhury and Emil Wolf. Coherence effects in the near-field. *Journal of Modern Optics*, 51(11):1603–1612, 2004.

[65] Lukas Novotny and Bert Hecht. *Principles of nano-optics*. Cambridge university press, 2012.

[66] Achim Hartschuh, Erik J Sanchez, X Sunney Xie, and Lukas Novotny. High-resolution near-field raman microscopy of single-walled carbon nanotubes. *Physical Review Letters*, 90(9):095503, 2003.

[67] Norihiko Hayazawa, Takaaki Yano, Hiroyuki Watanabe, Yasushi Inouye, and Satoshi Kawata. Detection of an individual single-wall carbon nanotube by tip-enhanced near-field raman spectroscopy. *Chemical Physics Letters*, 376(1-2):174–180, 2003.

[68] Indhira O Maciel, Neil Anderson, Marcos A Pimenta, Achim Hartschuh, Huihong Qian, Mauricio Terrones, Humberto Terrones, Jessica Campos-Delgado, Apparao M Rao, Lukas Novotny, et al. Electron and phonon renormalization near charged defects in carbon nanotubes. *Nature materials*, 7(11):878–883, 2008.

[69] Luiz Gustavo Cançado, Achim Hartschuh, and Lukas Novotny. Tip-enhanced raman spectroscopy of carbon nanotubes. *Journal of Raman Spectroscopy*, 40(10):1420–1426, 2009.

[70] Ryo Kato, Shun Igarashi, Takayuki Umakoshi, and Prabhat Verma. Tip-enhanced raman spectroscopy of multi-walled carbon nanotubes through d-band imaging: Implications for nanoscale analysis of interwall interactions. *ACS Applied Nano Materials*, 2020.

[71] Cla Duri Tschannen, Martin Frimmer, Thiago L Vasconcelos, Lei Shi, Thomas Pichler, and Lukas Novotny. Tip-enhanced stokes–anti-stokes scattering from carbyne. *Nano Letters*, 22(8):3260–3265, 2022.

[72] Andreij C Gadelha, Thiago L Vasconcelos, Luiz G Cançado, and Ado Jorio. Nano-optical imaging of in-plane homojunctions in graphene and mos2 van der waals heterostructures on talc and sio2. *The Journal of Physical Chemistry Letters*, 12(31):7625–7631, 2021.

[73] Ryan Beams, Luiz Gustavo Cançado, and Lukas Novotny. Raman characterization of defects and dopants in graphene. *Journal of Physics: Condensed Matter*, 27(8):083002, 2015.

[74] Andreij C Gadelha, Douglas AA Ohlberg, Fabiano C Santana, Gomes SN Eliel, Jessica S Lemos, Vinicius Ornelas, Daniel Miranda, Rafael Battistella Nadas, Kenji Watanabe, Takashi Taniguchi, et al. Twisted bilayer graphene: a versatile fabrication method and the detection of variable nanometric strain caused by twist-angle disorder. *ACS Applied Nano Materials*, 4(2):18581866, 2021.

[75] Yongjun Lee, Seki Park, Hyun Kim, Gang Hee Han, Young Hee Lee, and Jeongyong Kim. Characterization of the structural defects in cvd-grown monolayered mos 2 using near-field photoluminescence imaging. *Nanoscale*, 7(28):11909–11914, 2015.

[76] Weitao Su, Naresh Kumar, Sandro Mignuzzi, Jason Crain, and Debdulal Roy. Nanoscale mapping of excitonic processes in single-layer mos 2 using tip-enhanced photoluminescence microscopy. *Nanoscale*, 8(20):10564–10569, 2016.

[77] Mahfujur Rahaman, Raul D Rodriguez, Gerd Plechinger, Stefan Moras, Christian Schuller, Tobias Korn, and Dietrich RT Zahn. Highly localized strain in a mos2/au heterostructure revealed by tip-enhanced raman spectroscopy. *Nano letters*, 17(10):6027–6033, 2017.

[78] Alexander G Milekhin, Mahfujur Rahaman, Ekaterina E Rodyakina, Alexander V Latyshev, Volodymyr M Dzhagan, and Dietrich RT Zahn. Giant gap-plasmon tip-enhanced raman scattering of mos 2 monolayers on au nanocluster arrays. *Nanoscale*, 10(6):2755–2763, 2018.

[79] Yoshito Okuno, Ophélie Lancry, Agnès Tempez, Cristina Cairone, Matteo Bosi, Filippo Fabbri, and Marc Chaigneau. Probing the nanoscale light emission properties of a cvd-grown mos 2 monolayer by tip-enhanced photoluminescence. *Nanoscale*, 10(29):14055–14059, 2018.

[80] Ryo Kato, Takayuki Umakoshi, Rhea Thankam Sam, and Prabhat Verma. Probing nanoscale defects and wrinkles in mos2 by tip-enhanced raman spectroscopic imaging. *Applied Physics Letters*, 114(7), 2019.

[81] Alvaro Rodriguez, Tim Verhagen, Martin Kalbac, Jana Vejpravova, and Otakar Frank. Imaging nanoscale inhomogeneities and edge delamination in as-grown mos2 using tip-enhanced photoluminescence. *physica status solidi (RRL)–Rapid Research Letters*, 13(11):1900381, 2019.

[82] Teng-Xiang Huang, Xin Cong, Si-Si Wu, Kai-Qiang Lin, Xu Yao, Yu-Han He, Jiang-Bin Wu, Yi-Fan Bao, Sheng-Chao Huang, Xiang Wang, et al. Probing the edge-related properties of atomically thin mos2 at nanoscale. *Nature communications*, 10(1):5544, 2019.

[83] Jizhou Wang, Zehua Han, Zhe He, Kai Wang, Xiaohui Liu, and Alexei V Sokolov. Tip-enhanced photoluminescence of monolayer mos2 increased and spectrally shifted by injection of electrons. *Nanophotonics*, (0), 2023.

[84] Ryan Beams, Luiz Gustavo Cançado, Sang-Hyun Oh, Ado Jorio, and Lukas Novotny. Spatial coherence in near-field raman scattering. *Physical Review Letters*, 113(18):186101, 2014.

[85] Jenaina Ribeiro-Soares, RM Almeida, Eduardo B Barros, Paulo T Araujo, Mildred S Dresselhaus, Luiz G Cançado, and Ado Jorio. Group theory analysis of phonons in two-dimensional transition metal dichalcogenides. *Physical Review B*, 90(11):115438, 2014.

[86] RS Alencar, Cassiano Rabelo, Hudson LS Miranda, Thiago L Vasconcelos, Bruno S Oliveira, Aroldo Ribeiro, Bruno C Puublio, Jenaina Ribeiro-Soares, AG Souza Filho, Luiz Gustavo Cançado, et al. Probing spatial phonon correlation length in post-transition metal monochalcogenide gas using tip-enhanced raman spectroscopy. *Nano letters*, 19(10):7357–7364, 2019.

[87] Kirby KH Smithe, Andrey V Krayev, Connor S Bailey, Hye Ryoung Lee, Eilam Yalon, Ozgur Burak Aslan, Miguel Munoz Rojo, Sergiy Krylyuk, Payam Taheri, Albert V Davydov, et al. Nanoscale heterogeneities in monolayer mose2 revealed by correlated scanning probe microscopy and tip-enhanced raman spectroscopy. *ACS Applied Nano Materials*, 1(2):572–579, 2018.

[88] Kyoung-Duck Park, Omar Khatib, Vasily Kravtsov, Genevieve Clark, Xiaodong Xu, and Markus B Raschke. Hybrid tip-enhanced nanospectroscopy and nanoimaging of monolayer wse2 with local strain control. *Nano letters*, 16(4):2621–2627, 2016.

[89] David Moore, Kiyoung Jo, Christine Nguyen, Jun Lou, Christopher Muratore, Deep Jariwala, and Nicholas R Glavin. Uncovering topographically hidden features in 2d

mose2 with correlated potential and optical nanoprobes. *npj 2D Materials and Applications*, 4(1):44, 2020.

[90] Andrey Krayev, Sergiy Krylyuk, Robert Ilic, Angela R Hight Walker, Ashish Bhattarai, Alan G Joly, Matej Velicky, Albert V Davydov, and Patrick Z El-Khoury. Comparable enhancement of ters signals from wse2 on chromium and gold. *The Journal of Physical Chemistry C*, 124(16):8971–8977, 2020.

[91] Weitao Su, Naresh Kumar, Haibo Shu, Ophelie Lancry, and Marc Chaigneau. In situ visualization of optoelectronic behavior of grain boundaries in monolayer wse2 at the nanoscale. *The Journal of Physical Chemistry C*, 125(48):26883–26891, 2021.

[92] Shuai Zhang, Baichang Li, Xinzhong Chen, Francesco L Ruta, Yinming Shao, Aaron J Sternbach, AS McLeod, Zhiyuan Sun, Lin Xiong, SL Moore, et al. Nano-spectroscopy of excitons in atomically thin transition metal dichalcogenides. *Nature communications*, 13(1):542, 2022.

[93] Kathryn Hasz, Zuocheng Hu, Kyoung-Duck Park, and Markus B Raschke. Tip-enhanced dark exciton nanoimaging and local strain control in monolayer wse2. *Nano Letters*, 23(1):198–204, 2022.

[94] Chanwoo Lee, Sung Tae Kim, Byeong Geun Jeong, Seok Joon Yun, Young Jae Song, Young Hee Lee, Doo Jae Park, and Mun Seok Jeong. Tip-enhanced raman scattering imaging of two-dimensional tungsten disulfide with optimized tip fabrication process. *Scientific reports*, 7(1):40810, 2017.

[95] Chanwoo Lee, Byeong Geun Jeong, Seok Joon Yun, Young Hee Lee, Seung Mi Lee, and Mun Seok Jeong. Unveiling defect-related raman mode of monolayer ws2 via tip-enhanced resonance raman scattering. *ACS nano*, 12(10):9982–9990, 2018.

[96] Ryo Kato, Toki Moriyama, Takayuki Umakoshi, Taka-aki Yano, and Prabhat Verma. Ultrastable tip-enhanced hyperspectral optical nanoimaging for defect analysis of large-sized ws2 layers. *Science Advances*, 8(28):eabo4021, 2022.

[97] Chanwoo Lee, Byeong Geun Jeong, Sung Hyuk Kim, Dong Hyeon Kim, Seok Joon Yun, Wooseon Choi, Sung-Jin An, Dongki Lee, Young-Min Kim, Ki Kang Kim, et al. Investigating heterogeneous defects in single-crystalline ws2 via tip-enhanced raman spectroscopy. *npj 2D Materials and Applications*, 6(1):67, 2022.

[98] Yuan Liu, Nathan O Weiss, Xidong Duan, Hung-Chieh Cheng, Yu Huang, and Xiangfeng Duan. Van der waals heterostructures and devices. *Nature Reviews Materials*, 1(9):1–17, 2016.

[99] Andreij C Gadelha, Douglas AA Ohlberg, Cassiano Rabelo, Eliel GS Neto, Thiago L Vasconcelos, Joao L Campos, Jessica S Lemos, Vinicius Ornelas, Daniel Miranda,

Rafael Nadas, et al. Localization of lattice dynamics in low-angle twisted bilayer graphene. *Nature*, 590(7846):405–409, 2021.

[100] Sourav Garg, J Pierce Fix, Andrey V Krayev, Connor Flanery, Michael Colgrove, Audrey R Sulkanen, Minyuan Wang, Gang-Yu Liu, Nicholas J Borys, and Patrick Kung. Nanoscale raman characterization of a 2d semiconductor lateral heterostructure interface. *ACS nano*, 16(1):340–350, 2021.

[101] Alvaro Rodriguez, Andrey Krayev, Matej Velicky, Otakar Frank, and Patrick Z El-Khoury. Nano-optical visualization of interlayer interactions in wse2/ws2 heterostructures. *The Journal of Physical Chemistry Letters*, 13(25):5854–5859, 2022.

[102] Jiaqi Shao, Fei Chen, Weitao Su, Naresh Kumar, Yijie Zeng, Ling Wu, and Hong-Wei Lu. Probing nanoscale exciton funneling at wrinkles of twisted bilayer mos2 using tip-enhanced photoluminescence microscopy. *The Journal of Physical Chemistry Letters*, 13(14):3304–3309, 2022.

[103] Yeonjeong Koo, Hyeongwoo Lee, Tatiana Ivanova, Ali Kefayati, Vasili Perebeinos, Ekaterina Khestanova, Vasily Kravtsov, and Kyoung-Duck Park. Dynamical control of interlayer excitons and trions in wse _2/mo _{0.5} w _{0.5} se _2 heterobilayer via tunable near-field cavity. *arXiv preprint arXiv:2203.02136*, 2022.

[104] Sharad Ambardar, Zachary H Withers, Jiru Liu, Xiaoyi Lai, Abdullah Albagami, Alina Zhukova, Pedro Fabris Capelli, Prasana K Sahoo, and Dmitri V Voronine. Quantum plasmonic two-dimensional ws 2–mos 2 heterojunction. *Nanoscale*, 15(16):7318–7328, 2023.

[105] Hassan Lamsaadi, Dorian Beret, Ioannis Paradisanos, Pierre Renucci, Delphine Lagarde, Xavier Marie, Bernhard Urbaszek, Ziyang Gan, Antony George, Kenji Watanabe, et al. Kapitza-resistance-like exciton dynamics in atomically flat mose _{2}-wse _{2} lateral heterojunction. *arXiv preprint arXiv:2306.13352*, 2023.

[106] Dong Hyeon Kim, Chanwoo Lee, Sung Hyuk Kim, Byeong Geun Jeong, Seok Joon Yun, Hyeong Chan Suh, Dongki Lee, Ki Kang Kim, and Mun Seok Jeong. Probing the multi-disordered nanoscale alloy at the interface of lateral heterostructure of mos2–ws2. *Nanophotonics*, (0), 2024.

[107] Min Yi and Zhigang Shen. A review on mechanical exfoliation for the scalable production of graphene. *Journal of Materials Chemistry A*, 3(22):11700–11715, 2015.

[108] Enlai Gao, Shao-Zhen Lin, Zhao Qin, Markus J Buehler, Xi-Qiao Feng, and Zhiping Xu. Mechanical exfoliation of two-dimensional materials. *Journal of the Mechanics and Physics of Solids*, 115:248–262, 2018.

[109] Kei Kinoshita, Rai Moriya, Momoko Onodera, Yusai Wakafuji, Satoru Masubuchi, Kenji Watanabe, Takashi Taniguchi, and Tomoki Machida. Dry release transfer of

graphene and few-layer h-bn by utilizing thermoplasticity of polypropylene carbonate. *npj 2D Materials and Applications*, 3(1):22, 2019.

[110] Ji Won Suk, Alexander Kitt, Carl W Magnuson, Yufeng Hao, Samir Ahmed, Jinho An, Anna K Swan, Bennett B Goldberg, and Rodney S Ruoff. Transfer of cvd-grown monolayer graphene onto arbitrary substrates. *ACS nano*, 5(9):6916–6924, 2011.

[111] Filippo Pizzocchero, Lene Gammelgaard, Bjarke S Jessen, Jose M Caridad, Lei Wang, James Hone, Peter Boggild, and Timothy J Booth. The hot pick-up technique for batch assembly of van der waals heterostructures. *Nature communications*, 7(1):11894, 2016.

[112] Seong-Jun Yang, Shinyoung Choi, Francis Okello Odongo Ngome, Ki-Jeong Kim, Si-Young Choi, and Cheol-Joo Kim. All-dry transfer of graphene film by van der waals interactions. *Nano letters*, 19(6):3590–3596, 2019.

[113] Cassiano Rabelo. *TIP-ENHANCED RAMAN SPECTROSCOPY in GRAPHENE*. PhD thesis, Universidade Federal de Minas Gerais, 2019.

[114] Neil Anderson. *Near-field Raman spectroscopy of single-walled carbon nanotubes*. PhD thesis, Rohcester University, 2007.

[115] Paulo Antonio Trindade Araujo. Study of electrostatic shielding and environmental interactions in carbon nanotubes by resonance raman spectroscopy. 2010.

[116] Ado Jorio, Cassiano Rabelo, Rafael Nadas, Hudson Miranda, Thiago Vasconcelos, Bráulio S Archanjo, Andreij C Gadelha, and Luiz Gustavo Cançado. Nano-raman spectral imaging of localized vibrations in two-dimensional systems. In *Enhanced Spectroscopies and Nanoimaging 2022*, volume 12203, page 1220302. SPIE, 2022.

[117] Andreij C Gadelha, Rafael Nadas, Tiago C Barbosa, Kenji Watanabe, Takashi Taniguchi, Leonardo C Campos, Markus B Raschke, and Ado Jorio. Observation of well-defined kohn-anomaly in high-quality graphene devices at room temperature. *2D Materials*, 9(4):045028, 2022.

[118] Andreij C Gadelha, Alisson R Cadore, Kenji Watanabe, Takashi Taniguchi, Ana M de Paula, Leandro M Malard, Rodrigo G Lacerda, and Leonardo C Campos. Gate-tunable non-volatile photomemory effect in mos2 transistors. *2D Materials*, 6(2):025036, 2019.

[119] DG Purdie, NM Pugno, T Taniguchi, K Watanabe, AC Ferrari, and A Lombardo. Cleaning interfaces in layered materials heterostructures. *Nature communications*, 9(1):5387, 2018.

[120] Min Sup Choi, Gwan-Hyoung Lee, Young-Jun Yu, Dae-Yeong Lee, Seung Hwan Lee, Philip Kim, James Hone, and Won Jong Yoo. Controlled charge trapping by molybdenum disulphide and graphene in ultrathin heterostructured memory devices. *Nature communications*, 4(1):1624, 2013.

[121] Han-gyu Kim and Hyoung Joon Choi. Thickness dependence of work function, ionization energy, and electron affinity of mo and w dichalcogenides from dft and gw calculations. *Physical Review B*, 103(8):085404, 2021.

[122] Wolfgang MH Sachtler, GJH Dorgelo, and AA Holscher. The work function of gold. *Surface Science*, 5(2):221–229, 1966.

[123] Faisal Ahmed, Sunwoo Heo, Zheng Yang, Fida Ali, Chang Ho Ra, Ho-In Lee, Takashi Taniguchi, James Hone, Byoung Hun Lee, and Won Jong Yoo. Dielectric dispersion and high field response of multilayer hexagonal boron nitride. *Advanced Functional Materials*, 28(40):1804235, 2018.

[124] Ary Reis Portes, Rafael Battistella Nadas, Ado Jorio, and JHONATTAN CORDOBA. Electro-optical properties of a graphene device on a tip-enhanced raman. *Optics Letters*, 56(2):123–143, 2024.

[125] Benoit Latour, Sebastian Volz, and Yann Chalopin. Microscopic description of thermal-phonon coherence: From coherent transport to diffuse interface scattering in superlattices. *Physical Review B*, 90(1):014307, 2014.

[126] Supriyo Datta. *Electronic transport in mesoscopic systems*. Cambridge university press, 1997.

[127] E. H. Hasdeo, A. R. T. Nugraha, M. S. Dresselhaus, and R. Saito. Fermi energy dependence of first- and second-order raman spectra in graphene: Kohn anomaly and quantum interference effect. *Phys. Rev. B*, 94:075104, 2016.

[128] Ado Jorio, Mildred S. Dresselhaus, Riichiro Saito, and Gene Dresselhaus. *Raman Spectroscopy in Graphene Related Systems*. Wiley-VCH Verlag GmbH & Co KGaA, WeinHeim, Germany, 2010.

[129] Feng Shao and Renato Zenobi. Tip-enhanced raman spectroscopy: principles, practice, and applications to nanospectroscopic imaging of 2d materials. *Analytical and bioanalytical chemistry*, 411(1):37–61, 2019.

[130] Leandro M Malard, Lucas Lafeta, Renan S Cunha, Rafael Nadas, Andreij Gadelha, Luiz Gustavo Cançado, and Ado Jorio. Studying 2d materials with advanced raman spectroscopy: Cars, srs and ters. *Physical Chemistry Chemical Physics*, 23(41):23428–23444, 2021.

[131] Cassiano Rabelo, Hudson Miranda, Thiago L. Vasconcelos, Luiz Gustavo Cancado, and Ado Jorio. Tip-enhanced Raman Spectroscopy of Graphene. In *2019 4th International Symposium on Instrumentation Systems, Circuits and Transducers (INSCIT)*, pages 1–6. IEEE, 2019.

[132] M Büttiker, Y Imry, R Landauer, and S Pinhas. Generalized many-channel conductance formula with application to small rings. *Physical Review B*, 31(10):6207, 1985.

[133] Antonio Di Bartolomeo. Graphene schottky diodes: An experimental review of the rectifying graphene/semiconductor heterojunction. *Physics Reports*, 606:1–58, 2016.

[134] J Ribeiro-Soares, ME Oliveros, C Garin, MV David, LGP Martins, CA Almeida, EH Martins-Ferreira, K Takai, T Enoki, R Magalhães-Paniago, et al. Structural analysis of polycrystalline graphene systems by raman spectroscopy. *Carbon*, 95:646–652, 2015.

[135] J Maultzsch, S Reich, C Thomsen, H Requardt, and P Ordejón. Phonon dispersion in graphite. *Physical review letters*, 92(7):075501, 2004.

[136] Pedro Venezuela, Michele Lazzeri, and Francesco Mauri. Theory of double-resonant raman spectra in graphene: Intensity and line shape of defect-induced and two-phonon bands. *Physical Review B*, 84(3):035433, 2011.

[137] Márcia Maria Lucchese, F Stavale, EH Martins Ferreira, Cecılia Vilani, Marcus Vinicius de Oliveira Moutinho, Rodrigo B Capaz, Carlos Alberto Achete, and A Jorio. Quantifying ion-induced defects and raman relaxation length in graphene. *Carbon*, 48(5):1592–1597, 2010.

[138] Ryan Beams, Luiz Gustavo Cançado, and Lukas Novotny. Low temperature raman study of the electron coherence length near graphene edges. *Nano letters*, 11(3):1177–1181, 2011.

[139] L Gustavo Cançado, A Jorio, EH Martins Ferreira, F Stavale, Carlos Alberto Achete, Rodrigo Barbosa Capaz, Marcus Vinicius de Oliveira Moutinho, Antonio Lombardo, TS Kulmala, and Andrea Carlo Ferrari. Quantifying defects in graphene via raman spectroscopy at different excitation energies. *Nano letters*, 11(8):3190–3196, 2011.

[140] Luiz Gustavo Cançado, Mateus Gomes Da Silva, Erlon H Martins Ferreira, Ferdinand Hof, Katerina Kampioti, Kai Huang, Alain Pénicaud, Carlos Alberto Achete, Rodrigo B Capaz, and Ado Jorio. Disentangling contributions of point and line defects in the raman spectra of graphene-related materials. *2D Materials*, 4(2):025039, 2017.

[141] Daohua Song, Feng Wang, Gordana Dukovic, M Zheng, ED Semke, Louis E Brus, and Tony F Heinz. Direct measurement of the lifetime of optical phonons in single-walled carbon nanotubes. *Physical review letters*, 100(22):225503, 2008.

[142] Kwangu Kang, Daner Abdula, David G Cahill, and Moonsub Shim. Lifetimes of optical phonons in graphene and graphite by time-resolved incoherent anti-stokes raman scattering. *Physical Review B*, 81(16):165405, 2010.

[143] Jens Sonntag, Kenji Watanabe, Takashi Taniguchi, Bernd Beschoten, and Christoph Stampfer. Charge carrier density dependent raman spectra of graphene encapsulated in hexagonal boron nitride. *Physical Review B*, 107(7):075420, 2023.

[144] Yuan Cao, Valla Fatemi, Shiang Fang, Kenji Watanabe, Takashi Taniguchi, Efthimios Kaxiras, and Pablo Jarillo-Herrero. Unconventional superconductivity in magic-angle graphene superlattices. *Nature*, 556(7699):43–50, 2018.

[145] Eva Y Andrei and Allan H MacDonald. Graphene bilayers with a twist. *Nature materials*, 19(12):1265–1275, 2020.

[146] Long Yuan and Libai Huang. Exciton dynamics and annihilation in ws 2 2d semiconductors. *Nanoscale*, 7(16):7402–7408, 2015.

[147] Bruno R Carvalho, Yuanxi Wang, Sandro Mignuzzi, Debdulal Roy, Mauricio Terrones, Cristiano Fantini, Vincent H Crespi, Leandro M Malard, and Marcos A Pimenta. Intervalley scattering by acoustic phonons in two-dimensional mos2 revealed by double-resonance raman spectroscopy. *Nature communications*, 8(1):14670, 2017.

[148] Xin Zhang, Xiao-Fen Qiao, Wei Shi, Jiang-Bin Wu, De-Sheng Jiang, and Ping-Heng Tan. Phonon and raman scattering of two-dimensional transition metal dichalcogenides from monolayer, multilayer to bulk material. *Chemical Society Reviews*, 44(9):2757–2785, 2015.

[149] Pedro Soubelet, Alex E Bruchhausen, Alejandro Fainstein, Karol Nogajewski, and Clément Faugeras. Resonance effects in the raman scattering of monolayer and few-layer mose 2. *Physical Review B*, 93(15):155407, 2016.

[150] Elena Del Corro, Humberto Terrones, Ana Elias, Cristiano Fantini, Simin Feng, Minh An Nguyen, Thomas E Mallouk, Mauricio Terrones, and Marcos A Pimenta. Excited excitonic states in 1l, 2l, 3l, and bulk wse2 observed by resonant raman spectroscopy. *Acs Nano*, 8(9):9629–9635, 2014.

[151] FDV Araujo, FWN Silva, T Zhang, C Zhou, Zhong Lin, Nestor Perea-Lopez, Samuel F Rodrigues, Mauricio Terrones, Antônio Gomes Souza Filho, RS Alencar, et al. Substrate-induced changes on the optical properties of single-layer ws2. *Materials*, 16(7):2591, 2023.

[152] Kuilong Li and Wenjia Wang. Effects of substrates on the optical properties of monolayer ws2. *Journal of Crystal Growth*, 540:125645, 2020.

[153] Yeonjeong Koo, Yongchul Kim, Soo Ho Choi, Hyeongwoo Lee, Jinseong Choi, Dong Yun Lee, Mingu Kang, Hyun Seok Lee, Ki Kang Kim, Geunsik Lee, et al. Tip-induced nano-engineering of strain, bandgap, and exciton funneling in 2d semiconductors. *Advanced Materials*, 33(17):2008234, 2021.

[154] Arend M Van Der Zande, Pinshane Y Huang, Daniel A Chenet, Timothy C Berkelbach, YuMeng You, Gwan-Hyoung Lee, Tony F Heinz, David R Reichman, David A Muller, and James C Hone. Grains and grain boundaries in highly crystalline monolayer molybdenum disulphide. *Nature materials*, 12(6):554–561, 2013.

[155] Thuc Hue Ly, Ming-Hui Chiu, Ming-Yang Li, Jiong Zhao, David J Perello, Magdalena Ola Cichocka, Hye Min Oh, Sang Hoon Chae, Hye Yun Jeong, Fei Yao, et al. Observing grain boundaries in cvd-grown monolayer transition metal dichalcogenides. *ACS nano*, 8(11):11401–11408, 2014.

[156] Lasse Karvonen, Antti Säynätjoki, Mikko J Huttunen, Anton Autere, Babak Amirsolaimani, Shisheng Li, Robert A Norwood, Nasser Peyghambarian, Harri Lipsanen, Goki Eda, et al. Rapid visualization of grain boundaries in monolayer mos2 by multiphoton microscopy. *Nature communications*, 8(1):15714, 2017.

[157] Frederico B Sousa, Rafael Battistella Nadas, Rafael Martins, Ana PM Barboza, Jaqueline S Soares, Bernardo RA Neves, Ive Silvestre, Ado Jorio, and Leandro M Malard. Nano-optical investigation of grain boundaries, strain and edges in cvd grown mos _{2} monolayers. *arXiv preprint arXiv:2401.11984*, 2024.

[158] Maria Vanessa Balois-Oguchi, Norihiko Hayazawa, Satoshi Yasuda, Katsuyoshi Ikeda, Tien Quang Nguyen, Mary Clare Escano, and Takuo Tanaka. Probing strain and doping along a graphene wrinkle using tip-enhanced raman spectroscopy. *The Journal of Physical Chemistry C*, 127(12):5982–5990, 2023.

[159] Xin Wang, Jing Wu, Yuwei Zhang, Yu Sun, Kaikai Ma, Yong Xie, Wenhao Zheng, Zhen Tian, Zhuo Kang, and Yue Zhang. Vacancy defects in 2d transition metal dichalcogenide electrocatalysts: from aggregated to atomic configuration. *Advanced Materials*, 35(50):2206576, 2023.

[160] Takato Hotta, Akihiko Ueda, Shohei Higuchi, Mitsuhiro Okada, Tetsuo Shimizu, Toshitaka Kubo, Keiji Ueno, Takashi Taniguchi, Kenji Watanabe, and Ryo Kitaura. Enhanced exciton–exciton collisions in an ultraflat monolayer mose2 prepared through deterministic flattening. *Acs Nano*, 15(1):1370–1377, 2020.

Appendix A - Other measurements in graphene devices

This appendix displays the sweep measurements of two other graphene devices, number 2 and number 3. The data with the tip is displayed in red and without the tip in blue. All the Raman parameters of the bands displayed (see the Figure caption for details). Here, in particular, it is noticeable that the same trend for ρ is followed in Figure 4.6 (c) in the main text and in Figures A.1 and A.2 (i) in this appendix.

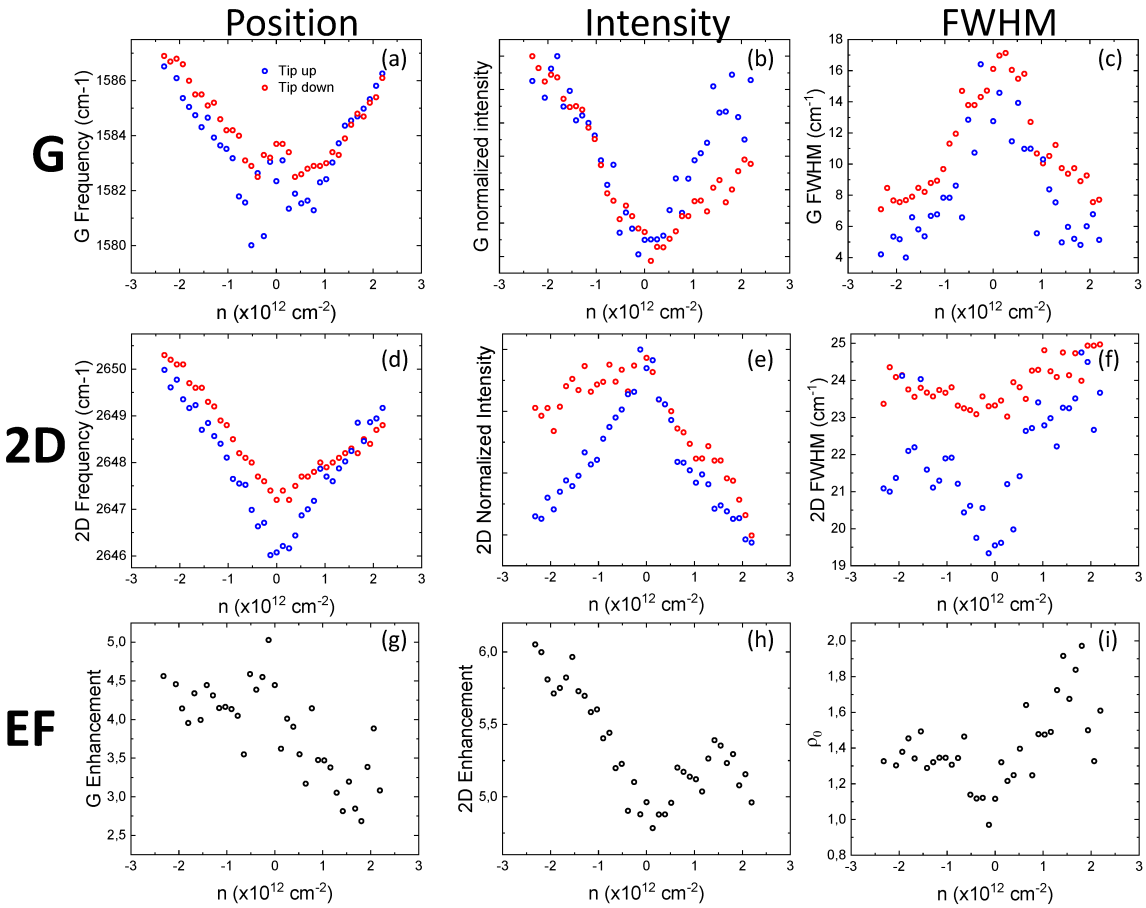

Figure A.1: Analysis of Raman spectra from a monolayer graphene device number 2, varying the number of charge carriers, displaying from the G band: (a) peak position, (b) intensity, and (c) full width at half maximum. Similarly, for the 2D band: (d), (e), and (f), respectively. The red (blue) circles are data acquired with (without) the tip. Panels (g) and (h) display the G and 2D enhancement factors as a function of n, while panel (i) displays the relative enhancement ρ. The data was acquired with the same experimental parameters as explained in the main text.

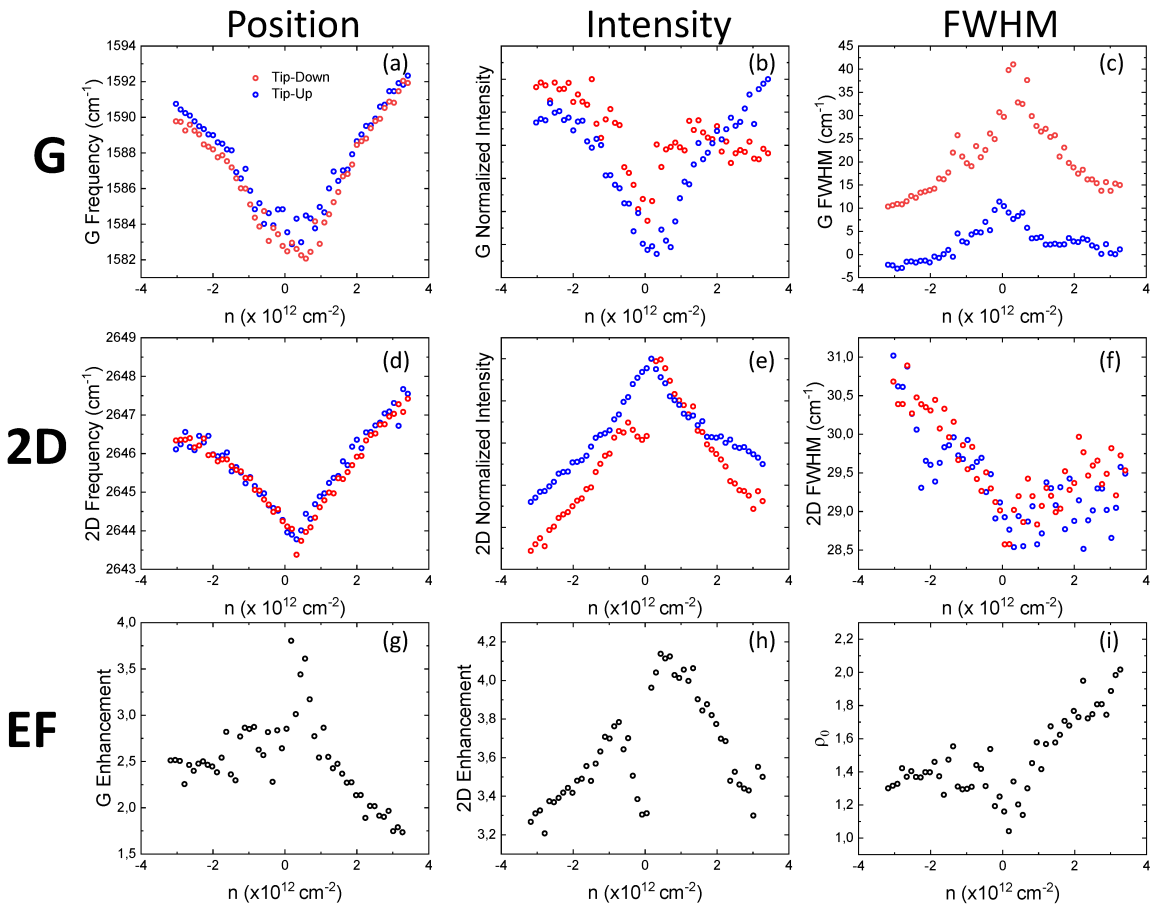

Figure A.2: Analysis of Raman spectra from a monolayer graphene device number 3, varying the number of charge carriers, displaying from the G band: (a) peak position, (b) intensity, and (c) full width at half maximum. Similarly, for the 2D band: (d), (e), and (f), respectively. The red (blue) circles are data acquired with (without) the tip. Panels (g) and (h) display the G and 2D enhancement factors as a function of n, while panel (i) displays the relative enhancement ρ. The data was acquired with the same experimental parameters as explained in the main text.